Entwicklung axonaler Dioden zur Untersuchung des gerichteten Informationsflusses in neuronalen Strukturen

Von der Fakultät für Mathematik, Informatik und Naturwissenschaften der RWTH Aachen University zur Erlangung des akademischen Grades eines Doktors der Naturwissenschaften genehmigte Dissertation

vorgelegt von

Diplom-Physiker

Jonas Albers

aus Lübeck

Berichter:

Universitätsprofessor Dr. rer. nat. Andreas Offenhäusser
Universitätsproffessorin Dr. rer. nat. Sonja Grün

Tag der mündlichen Prüfung: 22. November 2016

Diese Dissertation ist auf den Internetseiten der Universitätsbibliothek online verfügbar.

Abstract

The highly complex architecture of the central nervous system (CNS) is of paramount importance for the sophisticated information processing performed by the brain. Numerous functional regions are identified and arranged in different parts of the CNS and associated with individual assignments. Even though the function as well as the connectivity of the regions is known, it remains poorly understood how their function and entanglement arise. So far various factors have been identified, that are known to impact neuronal growth on various scale ranging from single cell level up to the scale of populations of neurons. Following the knowledge of these cues numerous approaches arose to reveal the role of individual factors and their combination to improve the knowledge of network development in an *in vitro*.

The first part of this work considers neuronal growth and network formation on substrates patterned with differently shaped structures. To this end, live-cell imaging was used to compare axonal growth on homogeneous with the one on patterned cultures. Here, mainly the impact of the edge of substrate-bound protein pattern was investigated. Immunofluorescence staining were performed in order to identify the effect of differently shaped gateways between adjacent pattern on axonal and dendritic growth. These experiments reveal a high selectivity for the orientation of axonal growth by choosing appropriate parameters for the design of the junction. Dendritic growth in contrast, could not be affected to the same extend by the pattern geometry.

In the second part the impact of neurite growth on functional connectivity is investigated using calcium-imaging techniques. After network maturation ensures a sufficient connectivity within and among populations, sequences of spontaneous neuronal activity were recorded. The orientation of occurring excitation of the network was validated with respect to the gateway design. For this purpose, an analysis script was developed in MATLAB, that automatically decodes the fluorescence sequences in event traces with a dynamic threshold method. As a consequence the delayed neuronal activity can be used to rate the impact of gateway design on functional connectivity. Furthermore, the causal influence between active areas within the network is calculated and evaluated providing an additional measure for functional correlations.

The last part of this thesis combines the previous findings generating a system with circulat-

ing neuronal action potentials. First of all, neuronal growth on the new pattern was evaluated and compared with previous findings. Subsequently, signal propagation on this system is characterized by the above mentioned analysis script.

Overall, this thesis illustrates the applicability of substrate-bound protein pattern as a versatile platform for the guidance of neuronal outgrowth as well as directed functional connectivity. By tuning the geometric parameters of the pattern a high selectivity for axonal growth and the resulting connectivity can be achieved. This allows the generation of a model system for the investigation of various aspects of signal propagation as well as neuro re- and degeneration.

Zusammenfassung

Die hochkomplexe Architektur des Zentralnervensystems (ZNS) ist von enormer Wichtigkeit für die komplizierte Informations-Prozessierung des Gehirns. Viele verschiedene funktionale Regionen wurden in unterschiedlichen Bereichen des ZNS gefunden, denen individuelle Aufgaben zugeordnet werden. Auch wenn ihre Funktionen und Verknüpfungen bekannt sind, so ist das Entstehen dieser Eigenschaften noch wenig erforscht. Bisher konnte eine Vielzahl von Faktoren identifiziert werden, deren Einfluss auf das Wachstum von einzelnen Zellen bis hin zu Zellpopulationen reicht. Aufgrund des Wissens über diese Faktoren entstanden vielfältige Ansätze um den Einfluss einzelner Faktoren, aber auch deren Kombination, auf die Netzwerkentwicklung *in vitro* Kulturen zu erforschen.

Der erste Teil dieser Arbeit betrachtet das Wachstum von Neuronen und deren Netzwerkentstehung auf unterschiedlich strukturierten Substraten. Hierfür wurde speziell das Wachstum des Axons auf homogenen und strukturierten Substraten in Echtzeit beobachtet, um dieses zu vergleichen. Dabei wurde vornehmlich der Einfluss der Ränder von substratgebundenem Protein untersucht. Um den Unterschied verschieden geformter Übergänge zwischen benachbarten Strukturen auf axonales und dendritisches Wachstum zu analysieren, wurden Immunfluoreszenz-Färbungen durchgeführt. Mit einer geeigneten Form der Übergänge konnte eine hohe Selektivität der Orientierung des axonalen Wachstums anhand der Färbungen belegen werden. Ein solcher Einfluss konnte für das dendritsche Wachstum hingegen nicht nachgewiesen werden.

Im zweiten Teil der Arbeit liegt das Augenmerk auf der durch das neuronale Wachstum hervorgerufenen funktionalen Verbindung. Nachdem eine ausreichende Verknüpfung innerhalb und zwischen benachbarten Strukturen sichergestellt ist, werden Sequenzen spontaner neuronaler Aktivität mittels Kalzium Imaging aufgenommen. Die Richtung der propagierenden Erregung wird im Verhältnis zur Orientierung des Übergangs zwischen zweier Strukturen bewertet. Hierfür wurde eigens ein MATLAB-Skript entwickelt, das die Fluoreszenzaufnahmen mittels automatischer Schwellwertermittlung in Ereignisspuren umwandelt. Die so detektierten Verzögerungen neuronaler Aktivität können zur Bewertung der Übergangs und dessen Einfluss auf die funktionale Verbindung herangezogen werden. Darüber hinaus wurde der kausale Zusammenhang zwischen aktiven Bereichen ermittelt, der ein weiteres Maß für die

Korrelation benachbarter Populationen darstellt.

Der letzte Teil der Arbeit kombiniert die oben beschriebenen Resultate, um ein System mit zirkulierender neuronaler Aktivität zu generieren. Zunächst wurde das Zellwachstum auf dieser neuen Struktur mit dem auf bekannten Strukturen verglichen. Im Anschluss wurde die Signalausbreitung mit Hilfe des erwähnten MATLAB-Skripts charakterisiert.

Zusammenfassend beschreibt die vorliegende Arbeit die Anwendbarkeit von substratgebundenen Proteinstrukturen als vielseitige Plattform, das neuronale Wachstum, aber auch funktionale Verknüpfung in vordefinierte Richtungen zu leiten. Durch die Wahl geeigneter geometrischer Parameter für die Strukturen kann eine hohe Selektivität des axonalen Wachstums und der resultierenden Verbindungen erreicht werden. Dies erlaubt das Erstellen eines Modellsystems für die Untersuchung vielseitiger Aspekte der Signalausbreitung, die in der Neuroregeneration und bei neurodegenerativer Erkrankungen Anwendung finden können.

Contents

1 Introduction **1**

2 Fundamentals & Theory **5**

2.1 Primary neurons 5

2.1.1 Membrane potential 6

2.1.2 Action potential 8

2.1.3 Neuronal development 12

2.2 Microcontact printing 15

2.3 Immunofluorescence analyses 17

2.4 Functional imaging 19

3 Material & Methods **21**

3.1 Sample preparation 21

3.1.1 Stamp production 21

3.1.2 Stamp design 23

3.1.3 Surface modification 25

3.2 Cell culture 26

3.3 Live cell imaging 27

3.4 Immunofluorescence 28

3.5 Calcium imaging 29

3.6 Data analysis 30

4 Results & Discussion **33**

4.1 Culturing small populations of neurons 33

4.1.1 Different stamp materials 34

4.1.2 Influence of serum containing medium on cell growth 37

4.2 Protein patterning and neuronal outgrowth 39

4.2.1 Axonal turn angle 39

4.2.2 Impact of pattern geometry on neuronal outgrowth 45

4.2.3 Gateway design impacts neural development 46

4.3 Patterned cultures and neuronal activity 52
4.3.1 Optical recordings 52
4.3.2 Analysis of Granger conditional causality 59
4.3.3 Analysis of delayed neuronal activity 62
4.4 Impact of structure design on network polarity 67
4.5 Neuronal circulating action potential 70
4.5.1 Cell growth on neuroCAPs 70
4.5.2 Modification of the analysis script 72
4.5.3 Signals on the arc of neuroCAP structure 73
4.5.4 Signals on the daisy-chain part of neuroCAP structures 77
4.5.5 Signal propagation on neuroCAP structures 78
4.6 Calcium imaging in microfluidic systems 81

5 Outlook **85**
5.1 Genetically encoded calcium indicators 85
5.2 Electrical recording and stimulation with microelectrode array 87
5.3 Optogenetic stimulation 88
5.4 Applications for the established system 89

References **94**

Acknowledgment **111**

Appendix A: Figures **113**

Appendix B: Abbreviations **119**

Appendix C: Solutions and Materials **123**

1 Introduction

Since the beginning of time the brain was of particular interest for mankind and the earliest conveyed descriptions of the brain reach back to the Egyptians in the 17th century BC. At that time little to none was known about the function of the brain, whereas surgeries on the scull were performed with a positive outcome for the patient. Since then little progress in characterization of the brain and the nervous system was gained, as the human body was considered sacred and was not allowed to be opened. By the time of the early Greek philosophers the academics were debating if the seat of the soul, including consciousness and the control of body functions, was the brain or the heart. While Aristoteles thought that the soul is localized in the heart and the brain is just a cooling system for the blood, Hippocrates was aware of numerous brain functions that were associated with the soul. Nonetheless, at this time the available techniques for functional analysis were missing. Not until Galen, a Greece physician who lived in the Roman empire, performed anatomical studies on animals was the nervous system was discovered. Based on his investigations he could show that the muscles are connected to the brain by a large branched network of nerve fibers. He postulated that nerves activate muscles mechanically by carrying a mysterious substance. Since Galen there was a long time of no progress in brain research until Rene Descartes picked up Galen's theory. Descartes thought that body motion is controlled by hydraulic signals from the nervous system. But as one of the first scientists he also associated cognitive functions with the brain, where they were assumed to be carried out non-physically. The first benchmark of neuroanatomy was created by Thomas Willis (1621-1675) in Oxford who was the first who identified the brain itself as the central control organ for motion, emotion, cognition and the center of attention [1] and Emanuel Swedenborg proposed the association of different functions to variable areas in the brain. Nevertheless, Luigi Galvani's experiments revealed the electrical signal transmission in nerve fibers [2, 3], as he applied shocks of static electricity to the ends of frog legs, which contracted as a result. Since then, every new understanding of the brain and its functions was associated with a new investigational method. Camillo Golgi and Santiago Ramón Cajal used a staining with silver chromate salt to discover hundrets of distinct types of neurons with unique structure in the early years of the 20th century [4, 5]. During the first half of the

20th century other important discoveries were made by Alan Hodgkin, Andrew Huxley and others, who investigated the electrical properties of a nerve cell and revealed the biophysical properties of the action potential [6]. At the same time Bernard Katz and others discovered the electrochemistry of the synapse [7, 8]. In the second half of the 20th century the knowledge and the investigation methods developed rapidly. New methods in chemistry, genetics, computer science and other fields of research opened new insights into brain function and structure. However far more important, the multidisciplinary field of neuroscience arose; combining biology, chemistry, physics, and mathematics resulting in fascinating research topics of the 21st century including multielectrode recordings, genetic engineering and neuroimaging. All these new techniques helped to assemble the current state of knowledge about the human brain.
Many postulates were proven right or wrong and new unknown facts were revealed. The brain is the central organ of the nervous system and with 1.3 - 1.4 kg makes roughly 2% of the body weight [9]. It is composed of neurons, glial cells and blood vessels containing approximately 86 billion neurons and the same amount of glial cells [9]. With about 100 trillion synapses [9] between the neurons, a network of vast complexity is generated, in which each neuron should be reachable within four steps from an arbitrary point, assuming a homogeneous distribution of the synapses. But with this simple idea of structure it would be impossible to explain the complex functionality of the network. It is not only the network itself but the pattern of connectivity and differing distinction in connection strength of the contacts that determines its function [10]. Beside the synapses neurons themselves are also not homogeneously distributed across the brain, as 19% of the cerebral neurons are located in the cortical tissue. The cerebral cortex is a 2 - 4 mm thick layer of neural tissue that covers most parts of the brain [9]. Brain functions such as perception, attention, awareness, memory, thought, and language are associated with certain specific receptive fields in the cortex, where most functional areas are replicated on both hemispheres of the brain. To facilitate the vast number of functions and high sensitivity, the cortical area is increased by folding, thus two thirds of the cortex is buried in the sulci. Receptive fields that are separated for more than 200 - 800 μm do not overlap and share no information [11–14]. Lateral communication is achieved by cortical minicolumns containing approximatly 80 neurons. Nonetheless the lateral connections across the cortex are less dense than those between different layers of the cortex. To facilitate the distinct functionality of the brain, it is of paramount importance to control neuronal outgrowth on the single cell level. Neurogenesis is either influenced by intrinsic cues such as centrosome position [15] or extrinsic cues, which can be categorized as mechanical or chemical cues. Chemical components guiding neuronal growth are e.g. extracellular signaling proteins conveying cell attraction or repulsion [16, 17]. These proteins occur freely soluble or substrate

bound. In addition to these proteins, a direct cell-cell interaction is also reported [18] to affect orientation in neuronal development.

To study the various factors influencing neuronal development different *in vitro* approaches arose, each with their own advantages and weaknesses. Ideally, these systems allow exclusive patterned cell growth with an impact ranging from the single cell level to populations of neurons with a high reproducibility. At the same time, these systems offer the potential to interact with individual cells and/or the entire network for intra- and extracellular recording or stimulation. State of the art culture systems exhibit different characteristics suitable for miscellaneous applications. Microfluidic devices provide a highly reliable tool with predefined geometry and the possibility to culture tissue from different parts of the brain in parallel with controlled connectivity among the tissues [19–22] with a variety of cell concentrations. Even circular cell cultures with defined orientation of signal propagation can be established [23], which show comparable results to *in vivo* cultures regarding propagation velocity. At the same time, the encapsulation is the downside of this system, as no accessibility to individual cells at arbitrary positions is granted. In-mold patterning techniques [24–26] tackle the downside of inaccessibility of individual cells for recordings or stimulation. Here, cells are cultured in a recess with defined geometry and sharp edges, where cell growth is tightly restricted to the recess, which offers a cell adhesive surface. Thus, these systems offer the opportunity to grow low and high cell densities on predefined patterns that can be contacted from above. Even a guided functionality among populations of neurons in the recesses could be achieved by Feinerman and colleagues [24, 26]. On the downside, this system does not support a culture system with different tissue separated in adjacent molds and also the impact of the structure on the growth of single cells within the network remains limited. To generate a system with a higher impact on single cells and their connectivity, techniques for reliable patterning of individual cells were established such as photolithografic patterning [27, 28] and laser micropatterning [29]. Another widely used technique is microcontact printing [30, 31], which is able to generate protein patterns with dimensions ranging from sub-micrometer [32] up to several hundred micrometers [33] without any loss in accuracy and reproducibility. At the same time, single cells and populations of neurons are accessible to any kind of manipulation, as a protein layer is directly transferred on top of a substrate. This protein layer provides cell attractive regions surrounded by a cell repellent surface restricting cell growth to the pattern geometry. As the restriction from the protein is weak in comparison to the above explained methods and the neurons themselves secrete neurotrophic factors mediating cell adhesion, the number of cells needs to be chosen appropriately such that cell growth is exclusively restricted to the pattern.

In the present thesis, daisy-chained populations of neurons with a defined geometry were

created. Microcontact printing techniques were used to transfer patterns of substrate-bound protein consisting of poly-L-lysine and laminin to obtain networks of embryonic cortical rat neurons with defined geometry. As a basic principle, it is assumed that neuronal outgrowth is directed by turning events induced by edges of the protein structures [34]. This has been used to impact neuronal outgrowth of single cells [28, 30, 35] and populations of neurons [26] by differently sculpted protein patterns. All protein patterns used in this thesis exhibit a predefined gateway at the point where adjacent structures touch and their dimensions are chosen appropriately to obtain ramified networks within a single pattern to ensure mature networks with a good vitality. The focus of the survey is on the impact of neuronal outgrowth induced by the geometry of protein patterns, the resulting connectivity between adjacent populations of neurons and the inevitable direction of signal propagation among populations. Furthermore, the optimized set of geometric parameters for guided cell growth and signal propagation will be used to generate a model system, that allows the investigation of network formation and communication in detail. Here, recurrent and self-triggering neuronal activity can be used to explore changes in neuronal plasticity as a consequence to external manipulation. For this purpose micropatterned glass substrates were used to culture embryonic cortical rat neurons. Samples were either used for immunohistochemical analyzes of axonal and dendritic growth after 10 - 14 days *in vitro* or optical recordings of spontaneous neuronal activity after 15 - 24 days *in vitro*. Subsequently, sequences of recorded activity were analyzed with a MATLAB script focusing on signal propagation across the gateway.

2 Fundamentals & Theory

In this chapter, an introduction to the theoretical background of this thesis will be given, to provide required fundamentals for better understanding the conclusions drawn based on the experimental results. General remarks on the primary neurons will be presented first, including the membrane potential, emergence and propagation of activity, and neuronal development. Here, the attention is focused on the interaction between neuronal cells and surface-bound proteins, followed by a discussion of the fundamentals of surface modification for guided cell growth. This chapter will be completed by the description of the experiments performed in this thesis to visualize neuronal cell growth by immunofluorescence and neuronal activity within and among networks by calcium imaging.

2.1 Primary neurons

A multiplicity of stimuli approach our body every minute where they are evaluated and treated enabling the organism to react appropriately. Nerve cells (see Figure 2.1) are the smallest functional unit in the challenge of information processing. These cells exhibit an intrinsic polarity for signal propagation as they manifest receiver units - the dendrites - and an emitter unit - the axon. Incoming stimuli are gathered by the dendrites and forwarded to the soma, con-

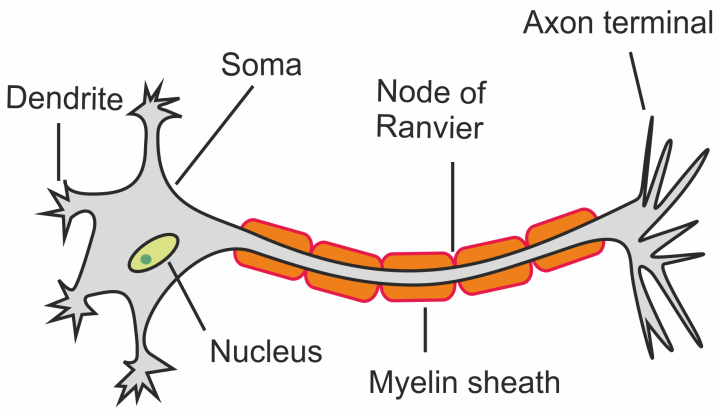

Figure 2.1: Sketch of a primary neuron with all essential components.

taining the nucleus and organelles like mitochondria, Golgi apparatus and others, maintaining the cell functionality. Adjacent to the soma the axon sprouts from the axon hillock and is terminated by the axon terminal. Here, connections to neighboring cells are formed and signals are transferred. A variety of ways to process information developed, which encompass mechanical [36–38], chemical [39], and electrical stimulation [3, 40]. All of these stimuli are integrated temporally and spatially inside the cell and determine its output. Even though the signal integration inside a single cell decides whether or not the signal is transmitted to a neighboring cell, it does not determine any network spanning activity. As network development shows a high complexity, signal propagation within the network is influenced by a variety of factors. When numerous neurons are combined to a network, it is not the single cell that accounts for signal transmission, but the combination of incoming signals to individual neurons in the network. In order to understand the complexity of signal transmission it is of paramount importance to figure out how information is processed in a network. Therefore the understanding should cover neuronal outgrowth, network formation, and the underlying processes resulting in the versatile functionality of single neurons and neuronal networks.

2.1.1 Membrane potential

Like all eukaryotic cells, neurons are surrounded by a cell membrane, that separates the intra- and extracellular space and consists of a lipid bilayer. Receptors and membrane spanning proteins are incorporated, which serve as ion channels and pumps. The membrane itself serves as an insulator and diffusion barrier for ions. Thus, the separation of ion species at both sides of the membrane is facilitated, see Figure 2.2 A. Here the most important ion species, Na^+, K^+ and Cl^-, are depicted and considered in later arguments. A concentration gradient for individual ions is established by ion pumps that actively ship ions across the membrane. Ion channels allow the ions to cross the membrane along the gradients that are depicted in Figure 2.2 B. For all eukaryotic cells, the charge separation leads to a non-zero potential, where the inside usually is biased on a negative potential. For neurons the potential difference from the intra- to extracellular space is approximately -70 mV [9]. The passive movement of the ions along the concentration gradient through the membrane is mediated by ion specific channels. For active ion transport an electrical force across the cell membrane is generated by consumption of adenosintriphosphate (ATP) and the pumps actively move the ions along this force. For a given ion concentration P_{Ion} the diffusive force and the electrical force for that specific ion compensate at a specific potential, such that the net flow across the membrane is zero. This transmembrane voltage is called the equilibrium potential. For any ion i the

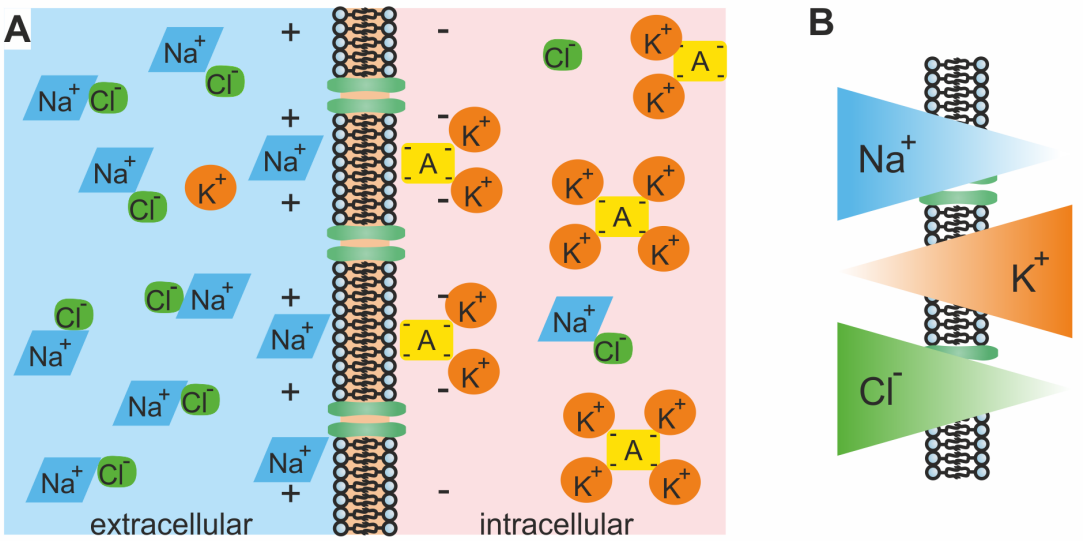

Figure 2.2: Schematic of a neuronal cell membrane. **A**) Ions are separated by the cell membrane, that is formed by a lipid bilayer. Membrane spanning proteins are embedded in the bilayer facilitating ions to cross the membrane. Different ion concentrations on both sides of the membrane generate a potential difference. **B**) Illustration of the concentration gradient across the membrane for the three ions with major impact on the membrane potential.

equilibrium potential can by calculated using the NERNST equation (2.1).

$$E_{eq,i} = \frac{RT}{zF} \ln \frac{[i]_{out}}{[i]_{in}} \tag{2.1}$$

Where R is the gas constant, T the absolute temperature, z the number of elementary charge and F the FARADAY constant. $[i]_{out}$ and $[i]_{in}$ are the extracellular and intracellular concentration of the ion i. This equation allows one to calculate the resting potential for a specific ion $E_{eq,i}$ but not for all ions at once. The cell membrane itself has a high intrinsic electrical resistivity caused by the lipid bilayer. That means the membrane can be assumed as a capacitor with a capacitance of roughly 2 $\mu F/cm^2$ [9], while the channels and pumps can be regarded as resistors. The capacitance of the membrane is a fixed value, but the resistance decreases with an increasing amount of channels embedded in the membrane. As a consequence the membrane can be described in an equivalent circuit, see Figure 2.3 A. For a single ion the variable conductance g represents the movement through the channels, while the electrochemical driving force V depicts the active ion transport by the pumps. The capacitive behavior of the membrane is accumulated for all ion species and indicated by the membrane capacitance C. A generalization of this equivalent circuit can be derived for fixed ion concentrations and fixed

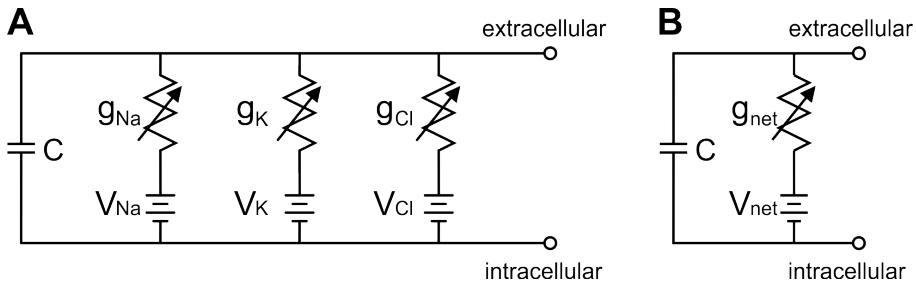

Figure 2.3: Equivalent circuit for the cell membrane. **A**) The fixed capacity of the bilayer is in parallel with the pathways for the ion species consisting of a electrochemical driving force V representing the ion pumps and a variable conductance g indicating the passive ion transport through the channels. **B**) Reduced circuit resulting from combining the ion-specific pathways by using the GOLDMAN-KATZ equation.

values of ion channel conductance, see Figure 2.3 B. Here the general net current is considered with g_{net} and the ion-specific pumps are summarized as V_{net}. Using the the GOLDMAN-KATZ equation (2.2) the resulting membrane potential E_m can be calculated considering the main ions involved in membrane depolarization as followed:

$$E_m = \frac{RT}{F} \ln \left(\frac{P_{K^+}[K^+]_{out} + P_{Na^+}[Na^+]_{out} + P_{Cl^-}[Cl^-]_{in}}{P_{K^+}[K^+]_{in} + P_{Na^+}[Na^+]_{in} + P_{Cl^-}[Cl^-]_{out}} \right) \tag{2.2}$$

Here R is the universal gas constant, T the absolute temperature and F the FARADAY constant. P_i represents the relative permeability for the ion i and $[i]_{in/out}$ is the intra-/extracellular concentration of the ion i respectively. In summary the GOLDMAN-KATZ equation (2.2) is the weighted average of the reversal potential of the individual ion species, where every ion species is weighted by their specific permeability. Consideration of calcium ions is omitted here, as the little exchange across the membrane results in low potential changes, but can be added with an additional pathway in the equivalent circuit and resulting term in GOLDMAN-KATZ equation 2.2 to complete the description. The ion concentration of the major species involved in membrane potential can be assumed as constant in the entire neuron. Changes of the ion concentration appear locally and can induce an action potential.

2.1.2 Action potential

A short-lasting event in which the membrane potential of a neuron rises and falls rapidly is called an action potential. These potential changes follow the all-or-none law and are mostly triggered by the strength of a stimulus. If the stimulus induced membrane potential change exceeds a threshold potential of roughly -55 mV [9], the action potential is triggered and the

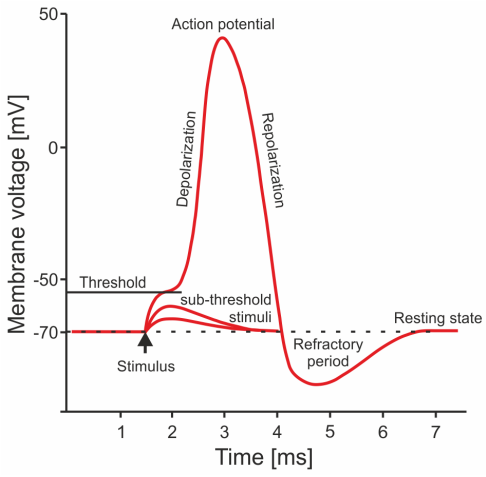

Figure 2.4: Schematic of an action potential. A cell resides in the resting state when a stimulus is applied. If the stimulus results in a depolarization above the threshold the potential rapidly rises to a maximal depolarization. Adjacent to the peak the membrane repolarizes and drops during the refractory period below the resting state.

membrane is depolarized, resulting in a potential change of 100 mV [9] compared to resting potential, see Figure 2.4. The potential change of about 100 mV during the depolarization is generated by fast voltage activated sodium channels first characterized by Hodgkin and Huxley [6]. At the end of the opening phase of the sodium channels, the slow potassium channels open and an efflux of potassium ions repolarizes the cell membrane. A refractory period follows the repolarization while the sodium and potassium channels stay inactive in a closed state. In this refractory period the resting potential is reestablished mainly by sodium-potassium ion pumps.

Besides sodium and potassium, other ions like calcium are involved in the depolarization of the entire cell. Within the dendrites the volume is small enough to depolarize the entire surrounding membrane and can be considered as a locally occurring event. To depolarize the entire soma, additional, mainly internal, ion concentration changes have to be triggered. To maintain the initially low concentration of calcium inside the cell a fraction is actively pumped across the membrane to the extracellular space while the majority of the ions are absorbed into the endoplasmatic reticulum (ER). The release of bound calcium from the ER into the cell results in a depolarization of the entire neuron and converts the local action potential into a cell spanning event. As the uptake mechanism for calcium ions is slower than for sodium and potassium the calcium concentration decreases more slowly than sodium. Beside this function, calcium is involved in a variety of cell signaling aspects, like neurotransmitter release [41].

Propagation of action potentials

From the soma of the neuron, the action potential travels along the axon hillock and along the cell membrane of the axon to adjacent cells. This means that close neighboring areas of the cell membrane get de- and repolarized consecutively. The refractory period prevents a backpropagation of the signal by the inactivity of the ion channels for sodium and potassium. To improve the signal propagation along the cell and the axon *in vivo*, the axon is covered with myelin sheaths. Schwanncells and/or oligodendrocytes enwrap axons with a multilamellar myelin membrane, whose segments are separated by nodes of Ranvier. Membrane capacitance is reduced by the sheath while the resistance is increased between the nodes. Thus, a saltatory movement of the action potential from node to node occurs [42, 43]. First suggestions for this saltatory movement were made by Ralph Lillie in 1925 [44], while it was experimentally evidenced by Tasaki [45, 46] and Huxley [47]. However, in the *in vitro* applied here, system neurons are not myelinated, therefore the action potential travels continuously along the axon towards axon terminals.

The propagation of a signal within the axon can be described by the cable theory [48, 49]. To apply this theory, the dimensions of axons and dendrites are approximated as cylinders with individual resistances r_m and capacitances c_m in parallel. Along a series of parallel capacitance and resistors, an additional resistance r_l is assumed, representing the movement of electric charge along the membrane. Considering the resistance R_m and capacitance C_m per unit area of membrane, the resistance R_l of the cytoplasm inside the axon, and the axon radius a this results in the following equations:

$$\begin{aligned} r_m &= \frac{R_m}{2\pi a} \\ c_m &= C_m 2\pi a \\ r_l &= \frac{R_l}{\pi a^2} \end{aligned}$$

For an easier derivation of the cable equation, $r_m = \infty$ and $c_m = 0$ is assumed. Using Ohm's law the current flow from $x = 0$ along the inside of the fiber can be calculated as: $\Delta V = -i_l r_l \Delta x$. Reducing Δx towards zero results in infinitesimal small parts of x resulting in:

$$\frac{1}{r_l}\frac{\partial V}{\partial x} = -i_l$$

As the membrane is not completely sealed, some ions, and thus current, flow through the membrane, bringing back r_m and i_m. By using infinitely small increments of x, the change of current in the cytoplasm of the axon Δi_l can be written as: $\partial i_l / \partial x = -i_m$. The flow of

charge towards the membrane, which is often referred as displacement current (i_c), results in a capacitance, that can be included in the formula:

$$i_c = c_m \frac{\partial V}{\partial t} \tag{2.3}$$

Expressing the current that passes the membrane (i_r) as $i_r = V/r_m$ results in the following equation using $i_m = i_r + i_c$:

$$\frac{\partial i_l}{\partial x} = -i_m = -\left(\frac{V}{r_m} + c_m \frac{\partial V}{\partial t}\right) \tag{2.4}$$

The first term of the equation represents the change of longitudinal current per unit length. Combining equation 2.4 and equation 2.3 results in a first version of the cable equation, which is represented by a second-order partial differential equation:

$$\frac{1}{r_l}\frac{\partial^2 V}{\partial x^2} = c_m \frac{\partial V}{\partial t} + \frac{V}{r_m}$$

Here $V(x,t)$ is the voltage across the membrane at time t and position x. A characteristic length $\lambda = \sqrt{r_m/r_l}$ and time $\tau = r_m c_m$ can be defined, reducing the cable equation to:

$$\tau \frac{\partial V}{\partial t} = \lambda^2 \frac{\partial^2 V}{\partial x^2} - V. \tag{2.5}$$

With this equation, the correlation between axon diameter and conduction speed can be understood. A smaller diameter decreases the membrane capacitance c_m and more charge needs to be transferred to establish a transmembrane voltage ($Q = CV$). As the resistance increases at the same time less charge is transferred and the time constant τ increases. On the other hand the characteristic length λ increases with an increase in diameter, which results in a faster conduction velocity. Based on these correlations, unmyelinated neurons with a longer axonal range must exhibit larger axonal diameter to maintain a rapid expansion of electrical impulses before they fade.

Synaptic transmission

For synaptic transmission of an action potential to an adjacent cell, it firstly needs to reach the axon terminals. The intra-cell propagation velocity is $\approx$ 10 m/s [50] and can be neglected for considerations of synaptic transmission. When the signal reaches the axon terminals, it can be transferred to an adjacent cell via a synapse. Two types of synapses are known, chemical

and electrical synapses. Chemical synapses are predominantly found in the central nervous system and they shall be described here. The chemical synapse is composed of two morphologically different components, the presynaptic terminal on the axon and the postsynaptic terminal on the opposing cell. A variety of connections between two cells can be formed. While axon to dendrite is the most common one, also axon-to-axon, axon-to-soma [9, 51] and rarely dendrite-to-dendrite [52] connections are known to occur. The terminals of the synapse are separated by the synaptic cleft of roughly 20 nm [9]. The membrane of the presynaptic terminal is equipped with voltage gated Ca^{2+} channels, activating a signaling cascade resulting in neurotransmitter release as response to a potential change, induced by an incoming action potential. Prior to release, the neurotransmitters are stored in vesicles that then fuse with the membrane and thereby unleash the transmitter into the synaptic cleft. On the postsynaptic side, ion channels equipped with specific neurotransmitter receptors are incorporated into the membrane that trigger the opening of sodium channels upon binding events. Thus, the postsynaptic membrane gets depolarized and the actioin potential is transmitted. As the transmitter movement is a diffusion mediated process the signal transmission is delayed for $1 - 6$ ms [9, 53] from pre- to postsynaptic neuron. The presence and absence of neurotransmitter is of paramount importance for regulated signal transmission, unrequired transmitter species need to be removed from the cleft. Therefore, the presynaptic terminal is peppered with membrane spanning proteins reabsorbing neurotransmitter to load new vesicles for subsequent vesicle fusion.

2.1.3 Neuronal development

Neuronal development in general can be categorized into five stages of maturation, which are described here in more detail. At first, dissociated neurons settle to the bottom of the dish where they form thin filopodia, small hair like sprouts, on the outside of their membranes (see Figure 2.5, Stage 1) and start their development. In a second step after several hours, immature neurites are formed that all show the same length and are morphologically equal [54] (Stage 2). Cycles of growth and retraction are performed by these minor processes. In the third stage, roughly half a day after plating the cells, one neurite extends rapidly [55, 56] and becomes the axon, while the other neurites develop slower for up to a week before they evolve further and become dendrites in [57]. At stage 4 matured dendrites develop with reducing diameter at distal positions. Additionally Y-shaped branching appears in the dendritic sprouts [54, 58], developing the highly ramified dendritic structure. In contrast to dendrites, axons remain a thin neurite strand with a lower tendency of branching. In the last stage, stage 5, dendritic spines are formed, that facilitate the connection between neighbouring cells and thereby enable the

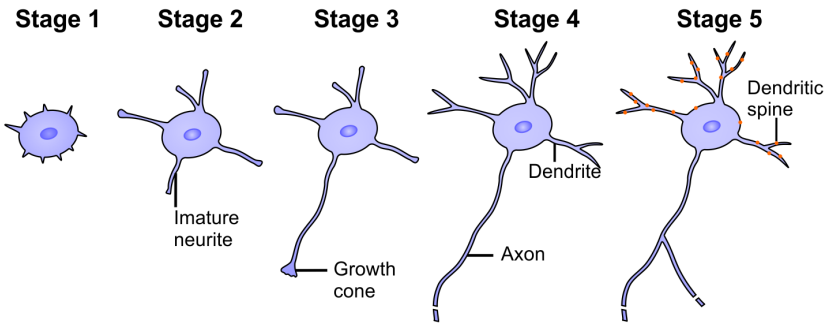

Figure 2.5: Schematic of the neuronal development. Soon after plating small protuberances are formed around the soma (Stage 1). The number of protuberances reduces and immature neurites that have a rather symmetrical appearance with a growth cone (Stage 2). One of the immature neurites sprouts faster than the others and breaks the symmetry, whereby the cellular polarity is immediately established (Stage 3). Several days later, remaining neurites branch and elongate. The characteristic dendritic tree is formed at this time (Stage 4). At roughly 7 days *in vitro*, synaptic contacts are formed via dendritic spines and axon terminals to assemble a neuronal network (Stage 5). Figure adapted from Fukata [54] and Arimuar [17].

communication among single neurons in a network.

Axonal development

The underlying mechanisms of axogenesis are still not completely understood yet. It remains unclear which cue leads to the development of distinct compartments - the axon and dendrites - with different compositions of proteins and their resulting functionality. Immature neurites constantly undergo an extension and retraction, which is coupled with an internal cell feedback system. The extension of a neurite causes a blocking feedback signal to the other neurites, a retraction in contrast causes an activation of growth for the other neurites. Actin filaments and microtubules inside neurites are regulated by morphogens, that decide which immature neurites becomes the axon [59]. Continuous self-activating feedback is given to the axon when the balance between blocking and activating feedback is broken [59, 60]. At the same time the other neurites receive blocking feedback that hinders their maturation. Even though the axonal fate is determined in an early state of neurogenesis it can change during development. Under certain conditions a dendrite can differentiate into an axon instead of the transected axon [60] depending on its length, while the previous axon transforms into a dendrite. The newly assigned axon elongates rapidly while the previously assigned axon shrinks.
On the way to their final destination the neurites are subjected by a variety of cues influencing their outgrowth. Intrinsic cues like centrosome position [15] can determine the axonal sprout-

ing and thereby the neuronal polarity. At later stages of development the interaction with surrounding cells becomes emphasized and the evolving axon responds to secreted proteins that mediate axon guidance and migration of cells [16, 17, 61–64]. As well as axonal guidance dendritic outgrowth is affected by chemoattractants that direct the apical orientation of the dendritic tree [65–67]. These chemoattractants are soluble and can occur freely distributed or bound to the substrate, as a result spatio-temporal protein gradients and patterns are formed that guide neurites to their final fate. Albeit, there are differences in the neuronal development *in vivo* and *in vitro* [68, 69], decoding the different impacts on axonal and dendritic growth *in vitro* helps to understand the situation *in vivo*.

Behavior on substrate-bound protein

For *in vitro* applications on culture dishes, substrate-bound proteins are of major interest as they can mimic the extracellular matrix (ECM), which offers diverse binding sites. *In vivo*, the ECM provides mechanical buffering, assists intra- and intercellular communication, and compartmentalizes different tissues. It is composed of a complex mixture of proteins and polysaccharides. Besides fibronectin and proteoglycans, laminin is one key component of the ECM by offering binding sites for adhesion proteins incorporated in the cell membrane. All known laminins share a similar trimeric structure [70] and are required for neuronal migration [71, 72] as their binding motifs predominantly interact with the integrins [73, 74]. These binding sites offer substantial attachment points, facilitating the axons stretching and conduct forces to the ECM [75, 76]. Integrins are membrane spanning proteins that represent the major cell-adhesion receptor family [77, 78]. In mammals eighteen α and eight β subunits of the integrins are known [79] that form the functional integrins in 24 different α - β combinations occur. Predominantly integrins represent receptors for ECM proteins such as laminin and collagen. A binding of integrins to ECM stands for a linkage to filaments of the cytoskeleton. Thus connecting the inside of a cell to ligands such as laminin [80]. Thereby, not only linkage is conveyed but also a repertoire of signal transduction capabilities is credited to these integrins [81–83]. The cell-cycle is influenced by an impact on progression, cell survival and gene expression. That means the cell adhesion strongly affects the morphology and the development of a cell, whereas the loss of adhesion is associated with cell death.
As described in the previous paragraph, the growth cone responds to proteins and even a concentration gradient of a single protein. This means that the growth cone can sense the margin of substrate-bound proteins and induce a turning event [34] to maintain the axon on attractive proteins. Combining the effects of attractive and repellent agents, a variety of approaches arose to guide neurons by combining a cell repellent surface with a pattern of cell

attractive protein [84–87]. Nonetheless, it remained challenging to specifically control axonal outgrowth and the resulting cellular polarity. Even though it is known that continuous and discontinuous substrate-bound protein gradients impact axonal polarity [88], it took some effort to implement this property for single cell guidance [86, 89, 90]. Beside the ambition to control neuronal outgrowth and polarity on a single cell level, other attempts were followed to culture populations of neurons with a confined geometry *in vitro* such as photolithographic patterning [27,28], laser micropatterning [29], microcontact printing [30,31], and microfluidic devices [19]. Ideally all approaches of patterning for individual cells, as well as populations of neurons should be compatible with techniques to interact with for potential measurements and manipulations. Here the focus shall be concentrated on microcontact printing, a technique that relies on the effect of substrate-bound proteins to pattern neuronal cultures.

2.2 Microcontact printing

A crucial criteria for *in vitro* cell culture applications is the presence of cell adhesion promoting proteins, but so far these proteins cannot be synthesized on a solid surface. Conferring sculptued network growth with this consideration clarifies the urgent need for a patterning technique that relies on selective adsorption of proteins. Furthermore, effects on cellular guiding and network shape induced by surface topography [91] should be avoided. Here, the potential of substrate-bound proteins for exclusive patterning of neuronal populations with directed cell growth and signal propagation should be proven. Microcontact printing (μCP) is the microstructuring method of choice for the applications in this thesis. This technique is commonly used in silicon technology [92, 93] to generate patterns of self-assembled monolayers with regions terminated by different chemical functionalities. It is also applicable for biological purposes and a variety of different types of proteins such as antibodies and synthetic peptides such as poly-L-lysine (PLL) can be printed onto hydrophilic and hydrophobic substrates [89,93,94]. It is possible to pattern large areas (> 1 cm^2) at a time with submicrometer resolution and an efficiency of $> 99\%$ after short contact between the stamp and substrate [30]. In contrast to other micropatterning techniques, like in photolithography, no strong acids or bases are needed [27,28] resulting in a good biocompatibility of microcontact Printing (μCP). Other biocompatible methods like laser patterning [29] are restricted in their pattern complexity, caused by limitations of interface techniques, which makes μCP a versatile and popular alternative technique. Nonetheless, the success of *in vitro* cell culture on a printed substrate-bound protein pattern relies heavily on the stamp material, the inter-structural spacing and the plated cell density.

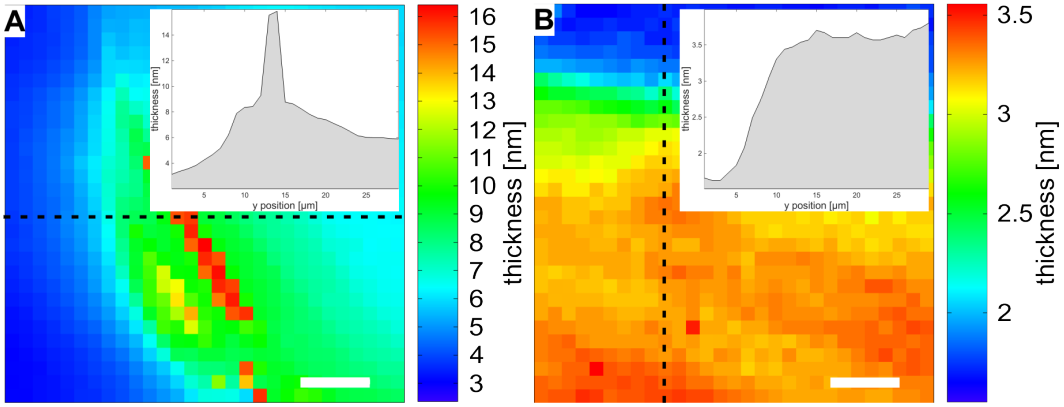

Figure 2.6: Surface plasmon microscopy (SPM) measurements of the thickness of protein layers printed with POP stamps. **A**) and **B**) show images of the edge of printed protein layers obtained from scanning localized SPM, that shed light on the thickness of the printed protein layer. The radially polarized light is focused through the objective onto the gold film. For image acquisition 29 $\times$ 29 scan points with a step of 1 μm were imaged. The inserts in the upper right corners indicate the protein thickness along the dashed lines. Scale bars: 5 μm. Figure B is adapted from: [33]

Elastomeric stamps are used to print monolayer quantities of proteins on a solid surface [32, 95], wetting of stamps is a crucial step in this process. Proteins are brought to the stamp surface by diffusion during this procedure, where they immobilize by specific or non-specific adsorption [96–100]. At the surface, the target molecules diffuse into the rubbery bulk, which provides a reservoir of reactants. Here the major issue is the solubility of the proteins, as many proteins from the extracellular matrix are not soluble in aqueous solution. μCP additionally requires drying the stamps as no specific printing could be achieved with a wet stamp as the protein solution would bleed all over the substrate. This lowers the number of available proteins for inks, as the target protein must not collapse at the dry state, while maintaining full functionality at the same time. For an adequate protein transfer with a resolution that reproduces the features of the stamp, flexible stamps are needed to allow sufficient contact between stamp and substrate surface. The local delivery of the target occurs by the absorption during the contact between the stamp and substrate, where the target molecules are electrostatically bound to the substrate surface [101]. This method enables printing of protein pattern with accurate dimensions ($\pm$ 50 nm) and sharp edges of 20 nm scale transition between protein pattern and surrounding [30, 102] when using poly(dimethylsiloxane (PDMS) stamps. In addition, printing of multicomponent patterns consisting of different target molecules printed in autonomous steps with independent orientation is possible with this technique [103, 104]. However, the major limitation of PDMS stamps is their low stiffness of these stamps, and

corresponding lack of rigidity. This prevents precise alignment and geometrical control of the pattern. In particular, sagging is a severe problem for PDMS stamps that generates unwanted contact between stamps and substrate resulting in undesired protein transfer [101]. To tackle the problem of sagging, polyolefin plastomer (POP) stamps can be used. Their performance in terms of transfer quality and efficiency is comparable to PDMS stamps [105]. To quantify the layer thickness of microcontact printed substrate-bound protein transferred by POP stamps to exclude surface topology effects on neurons, surface plasmon microscopy measurements were performed and revealed a thickness of 4.9 $\pm$ 1.1 nm [33]. Even though homogeneously coated protein layer with a thickness of 1.1 $\pm$ 0.3 nm are thinner than printed structures, topographic effects from the substrate-bound protein pattern can be excluded [33]. These values for a microcontact printed mixture of PLL and laminin are consistent with those for a printed mixture of poly-D-lysine and extracellular matrix protein measured with atomic force microscopy reported by Schwaab and colleagues [32]. Printing large areas with proteins results in inhomogeneities and wrinkles with higher protein layer thickness of up to 17 nm. These inhomogeneities are accused to be caused by multiple stacks of protein layer, that are not expected to influence neuronal outgrowth on a single cell level. Thus a guiding effect is anticipated at the step wise edge of the protein layer [33], see Figure 2.6. Also, sagging is not an issue with POP as the Young's modulus of POP (80 MPa) is roughly fifty times higher than that of PDMS [106]. POP's prevents undesired contact between stamp and substrate. Nonetheless, PDMS still is a popular material for microcontact printing, as it is a widely spread and easy to use material for patterns that do not sag or care about squishing.

2.3 Immunofluorescence analyses

To elucidate neuronal growth *in vitro*, immunofluorescence is the method of choice. Here cell components of microbiologic samples can be visualized with a fluorescence microscope. The visualization is facilitated by specific binding between antibodies and antigens, which enables targeting a fluorescent marker to specific biomolecules. With this technique the distribution of target molecules across a sample can be shown. For this purpose antibodies are modified and fluorophores are incorporated in their structure, making this method applicable for tissue sections, cultured cell lines or individual cells, where the arrangement of proteins, and small biological and non-biological molecules can be analyzed. Furthermore a combination with other non-antibody based methods for fluorescent staining like 4',6-Diamidin-2-phenylindol) (DAPI) to label DNA is possible.
As the cell membrane is not permeable for the antibodies used for staining of cells, just epi-

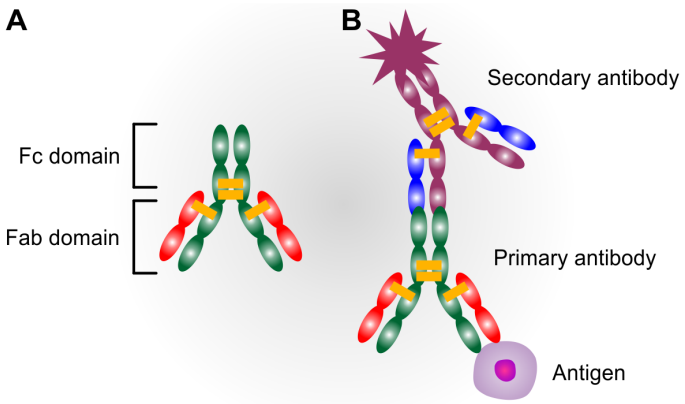

Figure 2.7: Cartoon of antibody structure and antigen binding. **A**) Sketch of the structure of an antibody. Every ellipse represents an amino-acid domain and the combination of green ellipses forms the constant region of the antibody responsible for molecular structure, the red ellipses represent the variable part for antigen detection. Disulfide bonds between polypeptides are represented as orange rectangles. **B**) Depicted binding events between primary antibody and antigen, and primary and fluorophore-conjugated secondary antibody. Figure adapted from [108].

topes on the outside of the cell can be visualized without any additional treatment. To overcome this limitation a permeabilization of the cell membrane needs to be achieved, with the consequence of a collapsing cell. The cell collapse can be prevented by a fixation of the cell, which preserves the inner structure of the cell for later visualization [107].

The two major types of staining techniques that can be applied to fulfill these requirements are direct and indirect immunofluorescence [108]. For direct immunofluorescence fluorescent labeled antibodies bind directly to the target antigen and the target molecules can be observed by fluorescence imaging techniques. The advantages of this technique on the one side are the low background signal and the absence of cross reactions. On the other side this technique yields a high false negative staining which complicates the differentiation of specific components. In addition, just a small number of antibodies are available for this technique making it cost intensive. Indirect immunofluorescence in contrast requires a primary and a fluorophore-conjugated secondary antibody, see Figure 2.7. In general, an antibody itself consists of two different main components, the constant region, that is responsible for the molecular structure and the variable region responsible for antigen detection. While the constant region consists of two strands of four amino-acid domains, while the variable region is composed of two strands with two amino-acid domains, ellipses in Figure 2.7. The different polypeptide strands are linked by disulfide bonds and the Y-shaped antibody is categorized into two distinct domains the Fc (fragment that crystallizes) and the Fab (fragment with antigen binding site) domain.

Antibodies with the same target antigens (variable region) can be generated with different constant regions by raising the antibodies in different species, as the constant region is species specific. In this way it is possible to generate a variety of antibodies with the same constant region but different antigen binding properties. In particular, this method offers a larger signal amplification as multiple secondary antibodies can bind to the primary antibody and each secondary antibody emits the same light intensity. At the same time, a huge diversity of primary antibodies is available from different species allowing the visualization of multiple cell components at time.
Colloquial, both the direct and indirect immunofluorescence suffers from some limitations. Photobleaching during image acquisition is a crucial factor and gratuitous light exposure should be avoided. Thus, a reduction of light intensity and the time span of illumination is advisable. As mentioned before, immunofluorescence is only applicable on fixed substrates and *in vitro* changes cannot be revealed by this method. In addition the fixation might cross-link proteins of interest and result in false positive signals. False negative signals in contrast occur for non-specific antibody binding.

2.4 Functional imaging

Besides neuronal outgrowth, neuronal activity is of particular interest in *in vitro* cultures, as it reveals much additional information about connectivity and functionality. Over the years different approaches arose to measure cellular activity optically and they can be classified in two major groups: ion sensitive and voltage sensitive indicators. The most commonly used technique is the detection of ions, where calcium is the most popular target. Ion sensitive techniques indicate the calcium status of a tissue or an individual cell *in vivo*, as well as *in vitro*, by changes in the fluorescent properties of the indicator in response to Ca^{2+} binding. The first real time optical recording of calcium kinetics in cardiac cells was performed by Cannell in 1986 using intensified video cameras [109]. Nowadays these experiments are performed either with CCD or sCMOS cameras and a fluorescence microscope with different light sources ranging from mercury-vapor lamps to laser excitation. In general, there are two commonly used types of indicators, genetically encoded and synthetic indicators [110], however only synthetic indicators were used for this thesis.
Synthetic indicators are small molecules that are able to chelate ions, thereby changing the fluorescent properties of the indicator. The most commonly used Ca^{++} indicators are Fura-2, Indo-1, Fluo-3, Fluo-4 and Calcium Green-1. These molecules are based on ethylene glycol tetraacidic acid (EGTA), which is known as a chalting agent with a high calcium binding affin-

Table 2.1: Characteristics of the Ca^{2+}-indicators Fluo-3, Fluo-4, and Cacium Green-1 [111, 112]

Ca^{2+}-indicator	Exponential decay $t_{1/2}$ [s]	$K_d(Ca^{2+})$ [nM]
Fluo-4	339	345
Fluo-3	143	325
Calcium Green-1	123	190

ity. The lipophobic properties of their indicators impede the penetration of the cell membrane. To overcome this limitation the molecules with the chelator carboxyl-groups are masked as acetoxymethyl esters (AM), drastically increasing their lipophilic properties to allow transport through the cell membrane. Here, the cellular esterase will free the carboxyl groups and the indicator can bind calcium ions from the cytoplasm. At this point it is noteworthy that the acetoxymethyl ester (AM) can also enter the endoplasmatic reticulum and mitochondria [111], which show a higher calcium concentration then the cytoplasm, resulting in fluorescence signals that are not representative for calcium status inside the cell related to electrical activity. Binding of calcium ions to the fluorescence indicator leads to an increase in quantum yield during excitation with light of an appropriate wavelength [112]. The above mentioned indicators show differences in their properties, such as the calcium binding affinity K_d and quantum yield upon calcium binding. The stronger the bond between the indicator and calcium, the faster is the chelating of calcium but also the slower the release compared to lower K_d [112]. As a consequence, at first it has to be defined for what purpose the calcium imaging recordings shall be performed to choose the synthetic indicator with appropriate binding affinity. In a second step, the quantum yield, bleaching rate, and excitation and emission wavelength of the indicator are of interest. A high quantum yield upon calcium binding ensures the detection of slight changes of calcium concentration in the cytoplasm while a low bleaching rate facilitates longer recording times with low loss in fluorescence intensity. In this thesis, Fluo-4 AM is used, as it has a high binding affinity [112] and a low bleaching with an exponential decay [111], enabling a detection of action potentials with little delay outperforming the majority of Ca^{2+}-indicators, see Table 2.1.

3 Material & Methods

This chapter will provide detailed information about the methods and techniques applied in the presented thesis. At first the sample preparation including clean room fabrication processes, stamp design, surface modification for *in vitro* application, and substrate characterization will be described. Consecutive paragraphs will focus on neuronal cell culture, live cell imaging and immunohistochemistry analysis to elucidate neuronal outgrowth, and calcium imaging for functional analysis of cultured neuronal networks. Lastly, data analysis for all experiments will be described and a general introduction to the MATLAB based script for signal propagation analysis of calcium imaging recordings will be given.

3.1 Sample preparation

To achieve patterned neuronal networks, it is of paramount importance to control cell adhesion. The following paragraphs illustrate the applied stamp production and surface modification techniques to obtain exclusive cell growth on patterned substrates. In particular clean room processes for stamp production will be illuminated containing detailed information of casting for POP and PDMS stamps. Subsequently, a circumstantial presentation of the structure design will be given including the nomenclature at the gateway. Finally the stamping processes for polyolefin plastomer and poly(dimethylsiloxane are described.

3.1.1 Stamp production

Mold fabrication

The stamps used to pattern substrate-bound proteins are molded from a structured SiO_2 wafer, therefore the mold production and subsequent stamp molding process itself are described. At first, a dark field chrome mask with arrays of the designed structures is written by an electron beam writer for later photolithography processes. A 0.6 mm thick dehydrated silicon wafer (5” diameter, MEMC Electronic Materials, USA) was spincoated with a 5 - 12 μm thick layer of photoresist (AZ 4562, Clarion GmbH, Germany) for photo-structuring purposes and subse-

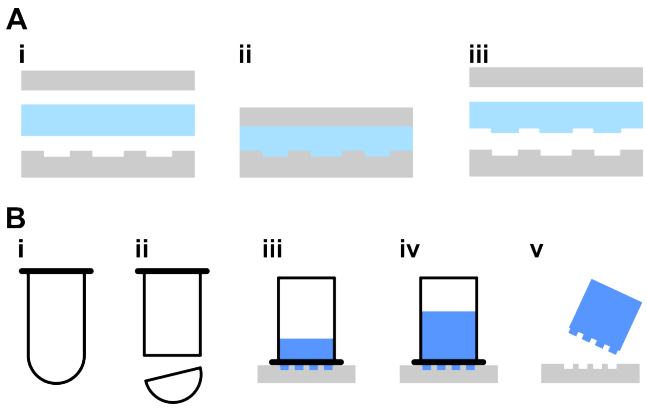

Figure 3.1: Molding of POP and PDMS stamps. **A**) Hot embossing of POP. i) POP film is positioned between a structured and an unstructured SiO_2-wafer. ii) Heat and pressure transfers the structures into the POP. iii) After removal of the wafers the structures remain in the POP. **B**) PDMS stamp production. i-ii) Cutting of the bottom of a 2 ml Eppendorf tube. iii) Pouring 750 μl PDMS into the tube placed on a structured silicon wafer and cure at 60°C for 3 hours. iv) Add another 750 μl of PDMS and curing over night at 60°. v) Cut open the tube and remove the PDMS stamp from the surface.

quently dried for 60 s at 130°C to stabilize the resist by removing solvents and partly desorb water from the resist layer. In a mask aligner the chrome mask is pressed onto the coated wafer and the structures are transferred by UV-photolithography to the photoresist. Here, the areas of the resist exposed to UV-light change their chemical properties by photochemical reactions and become soluble in the developing agent. A subsequent hard bake at 140°C for 90 s removes remaining water and fixes the structure. Subsequently, the resist is developed in MF-24-A (Karl Süss GmbH, Germany) for 50 s and the reaction is stopped by washing with Milli-Q water. In this step the light exposed areas of photoresist are removed. Reactive ion etching with SF_6 at -100°C and 150 W for 10 min transfers the structures 4.5 μm deep into the SiO_2 layer. In a last step of the clean room process the remaining resist is removed by an oxygen plasma treatment at 0.04 mbar and 100 W for 3.5 minutes and final washing with acetone and propanol. A release layer of (Tridecafluoro-1,1,2,2-tetrahydrooctyl)trichlorosilane (FOTCS) (Sigma, Germany) is covalently bound to the clean SiO_2 by vapor deposition of FOTCS at 45 mbar for 1.5 h in an argon atmosphere after plasma activation in an oxygen plasma at 0.8 mbar at 80 W for 3 minutes before stamps are molded.

Stamp casting

As described in Chapter 2.2 there are two different stamp materials that require different stamp fabrication methods. Polyolefine plastomer (POP) stamps are molded by hot embossing as described by [100, 113]. Briefly, a POP film is positioned between a structured and a planar SiO_2

wafer, both coated with FOTCS, see Figure 3.1 A. The whole system is heated and by pressing the wafer on the plastomer the structures are transferred to the POP. Dimensions are retained as the system cools down. Prior to stamping, 1 × 1 cm pieces are cut from the film containing an array of structures. The fabrication of poly(dimethylsiloxane (PDMS) (Sylgard 184, Dow Corning Corporation) stamps is a multistage process as depicted in Figure 3.1 B. At first, the bottom is cut off of 2 ml Eppendorf tubes and these tubes are placed upside down above the structures on the wafer. Subsequently, 750 μl PDMS in the ration 10:1 (base:curing agent) is poured into these tubes and cured at 60°C for 3 h. Another 750 μl of PDMS is poured onto the polymerized PDMS and cured over night at 60°C to obtain a stamp of a proper weight. In a final step, stamps were removed from the silicon wafer and the Eppendorf tubes were cut open to release the PDMS stamps. At the end, stamps of approximately 2 g and a diameter of 1 cm are obtained.

3.1.2 Stamp design

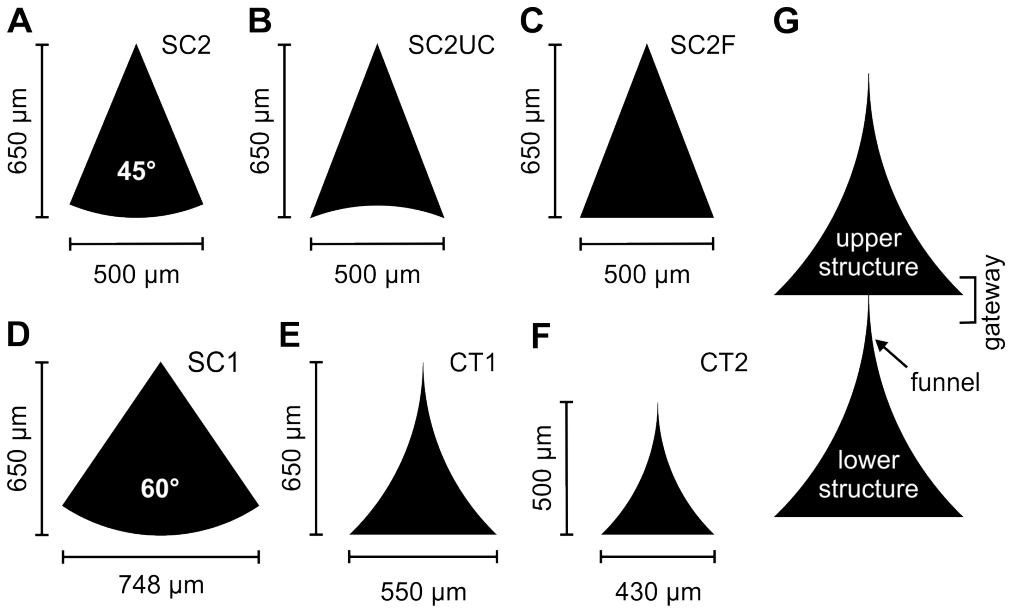

Figure 3.2: Cartoon of the different structure designs used in this thesis. **A**)-**C**) show a sector of a circle (SC) structure with an apex angle of 45° and different designs of the base. The curvature of the base for **A**) and **B**) is the same but opposed orientation. Base variations are also applied for all other structures, designs not shown here. **D**) depicts another SC structure with an apex angle of 60°. **E**) and **F**) show curved sided triangle (CT) structures of different height. **G**) Close up of a gateway between two adjacent CT structures in a daisy-chained arrangement including the nomenclature used in this thesis.

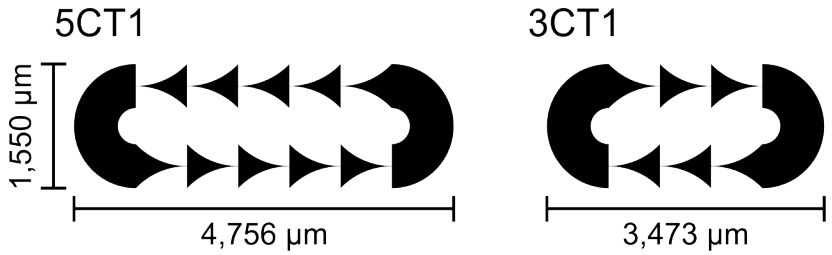

Figure 3.3: Cartoon of the two neuroCAP structures 5CT1 and 3CT1 with annotation of individual width. The height is stated once as it is same for both structures.

For the first experiments lines of identical daisy-chained triangular structures were arranged in an array of 1 cm $\times$ 1 cm with a horizontal 200 μm separation of the lines. Four different basic structures were designed. Two sector of a circle (SC) structures with opening angles of 60° and 45° and a height of 650 μm are denoted, 'SC1' and 'SC2', respectively. In addition, two triangular structures with curved sides (CT1, and CT2) were designed. A sketch of all triangular structures is shown in Figure 3.2. To validate the influence of the curvature of the base of a triangular structure on neuronal outgrowth at the gateway between adjacent structures and the resulting connectivity, three different base designs were used, exemplary depicted for an SC2 structure in Figure 3.2 A - C. Here the curvature is varied from normal bend of a sector of a circle over a straight line to a bend of the same radius as a circle with radius $r = 650$ μm but orientated contrarily to the SC structure. This variation is applied to all SC and CT structures; resulting designs area shown in Appendix Figure A.1. CT1 and CT2 only differ in height. The design of the CT structures was obtained by subtracting two circles of the same diameter that contact the base and the tip of a isosceles trapezoid. Circles with a radius of $r = 900$ μm and a trapezoid with height h $= 650$ μm, width of the small side $l_s = 2$ μm and base $l_b = 550$ μm were used to construct the CT1 structures. For CT2 structures circles with $r = 700$ μm and trapezoids with h $= 500$ μm, $l_s = 2$ μm, and $l_b = 430$ μm were used. The daisy-chained lines of structures are arranged in a way that the tip of a structure touches the center of the base of the adjacent structure to form a predefined gateway, see Figure 3.2, resulting in up to 15 structures in one daisy-chained line.

At a later stage of the thesis a new design was used as an advancement of the CT structures. The purpose of the new structure was to achieve neuronal circulating action potential (neuroCAP). Here the neuronal activity is supposed to follow the shape of the structure. To prove this hypothesis contrarily oriented lines of 3 and 5 daisy-chained CT1 structures were arranged with a pitch of 1000 μm. These lines were connected by an arc with a width of 550 μm, see Figure 3.3. Varying the chain length resulted in two distinct designs 5CT1, 4CT1, and 3CT1 to study revolving action potentials in a closed system.

3.1.3 Surface modification

Prior to *in vitro* cell culture experiments a surface modification needs to be performed to achieve exclusive cell growth on the substrate. At first, the hydrophobicity of the glass substrate is increased by silanization with FOTCS. Prior to cell culture substrate-bound proteins are transferred by microcontact printing to the surface to provide anchoring points for neuronal outgrowth.

Silanization

Glass surfaces are known to allow cell adhesion without any additional treatment. The cells adhere on the hydrophilic surface and form networks of neurons even though the maturation is slower than on protein coated surfaces. Thus, for patterning the glass surface needs to be modified to reduce the cell attractive behavior. Here, silanization is an easy to use method with high efficiency and reproducibility to achieve this characteristic. Two different approaches can be followed to mediate cell repellent properties. On the one hand, a surface charge can be introduced by covalently binding an epoxy-silane to the glass surface that results in a positively charged surface, thus resulting in a cell retraction by electrostatic repulsion. On the other hand the hydrophobicity of the surface could be increased by covalently binding FOTCS to the surface. In this thesis the second approach is chosen to increase the surface energy and thus the contact angle between distilled water and the surface from 51° (glass) to 108° for FOTCS coated glass. Hereby, the cell adhesion to the surface is drastically reduced. To generate a FOTCS coated surface, glass coverslips are rist activated in an oxygen plasma at 45 mbar for 3 minutes at 80 W. Thereby, contact with water forms reactive OH-groups at the glass surface that can mediate silane binding. Immediately afterwards, glass cover slips are transferred into an argon atmosphere where FOTCS is covalently linked to the glass surface by vapor deposition at 45 mbar for 1.5 h resulting in a silane monolayer covering the glass surface. This layer is stable for up to two month at normal atmosphere conditions and for long term cell culture for up to four weeks *in vitro*.

Microcontact printing

In this thesis two different stamp materials, PDMS and POP, were used to transfer the protein pattern onto the glass coverslip. The treatment of the stamps prior to printing is the same and just the printing procedure itself differs for the two materials. Sterilized and clean stamps are required for microcontact printing, thus they were cleaned in 70% ethanol for 15 minutes in an ultrasonic bath. Here all dust particles from storage as well as residues from previous

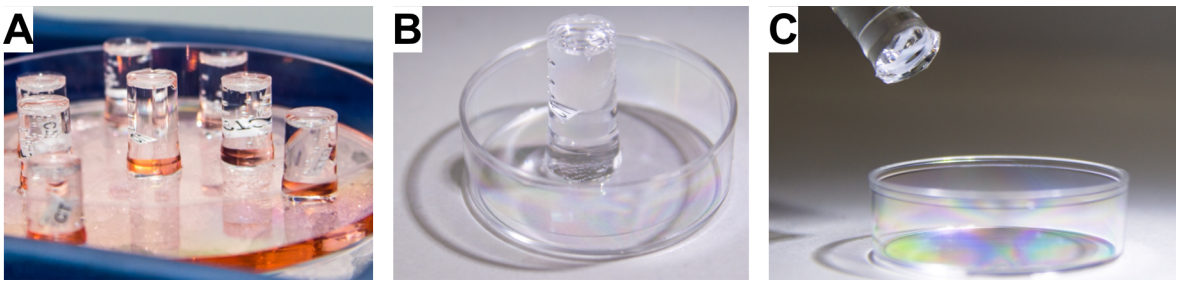

Figure 3.4: Microcontact printing procedure with PDMS stmaps. **A**) Inking of the stamps in protein solution. Here, the solution is colored for a better visualization. **B**) The dried stamp is placed on the silanized coverslip for protein transfer. **C**) Finally, the PDMS stamp is removed and the substrate is stored at 4°C prior to cell culture.

application of the stamps are removed. At the same time glass cover slips are sterilized under the sterile bench by UV-light exposure for 20 minutes. Subsequently, a protein solution is mixed on ice, containing 10 μg/ml FITC labeled poly-L-lysine (PLL) and 5 μg/ml laminin diluted in Gey's Balanced Salt Solution (GBSS) (Sigma, Germany). After thoroughly drying the stamp in a nitrogen stream they are immersed structures down into the protein solution for 20 minutes, see Figure 3.4 A. Afterwards, the stamps were thoroughly dried in a nitrogen stream and positioned with the structures face down in the middle of the coverslip. From this point, the stamps of the two materials are treated differently. For PDMS stamps it is sufficient to place them on the substrate for 20 minutes and their weight will lead to protein transfer to the surface. In contrast, POP stamps have to be slightly pressed down for 2 minutes for sufficient transfer of the proteins. Finally, the stamps, either PDMS or POP, are removed from the surface and the substrates are stored for 1 to 6 days at 4°C in the dark prior to cell seeding. This guaranties a stable protein coverage without degeneration and prevents a bleaching of the FITC (FITC) label.

3.2 Cell culture

For all cell culture experiments in this thesis cortical neurons from rat embryos of either sex were used. The embryonic cortices were obtained from E18 Wistar rats and immersed in Hanks Balanced Salt Solution without calcium and magnesium ($HBSS^-$) for at least 3 minutes. Subsequently, the cortices are mechanically dissociated with a silanized pasteur pipette by sucking and ejecting. This step is repeated with a pasteur pipette with a smaller diameter to ensure proper isolation of individual neurons. In a next step, 4 ml Hanks Balanced Salt Solution with calcium and magnesium ($HBSS^+$) are added and the suspended cells rest for

three minutes on ice. During this time the majority of glial cells bind the available calcium and magnesium ions and settle to the bottom of the tube. The bound ions activate surface adhesion proteins, which are higher expressed in glial cells and thus they are more likely to clump what increases their weight. As a consequence, neurons and glial cells settle in two layers and can be isolated. Neurons are extracted from the suspension and centrifuged for two minutes at 200 gand 25°C to separate the cells from the buffer. At last, the neuronal pellet is diluted in neurobasal medium (Life Technologies GmbH, Germany) with 1% B-27 supplement (Life Technologies), 0.5 mM L-glutamine, and 50 μg/ml gentamicin. For all experiments a cell concentration of 16,000 cells per cm^2 was seeded. Three hours after plating the cells the entire medium was replaced to remove cells that had not adhered thus far. Cells were kept at 37°C, 5% CO_2, and 100% humidity in the incubator and subsequent media changes were performed every 3 to 4 days when half of the medium was exchanged.

3.3 Live cell imaging

Conventional *in vitro* cell culture conditions offer little to no information about cellular development and the reaction to external cues during development, only snap-shots of neuronal development can be provided by light microscopy outside of the incubator. To gain more information about cellular development and the impact of applied external cues like geometrical restriction time-laps microscopy, henceforth live cell imaging, can be applied. Here, conditions comparable to regular cell culture experiments can be obtained with the opportunity to image cells to observe their development. In this thesis live cell imaging is used to survey neuronal outgrowth starting from day one *in vitro* for at least three days *in vitro* (DIV). Experiments were performed on a Zeiss Observer.Z1 equipped with a Zeiss Colibri system, a PCO.edge 5.5 scientific complementary metal-oxide-semiconductor (sCMOS) camera, and a Picon incubation chamber with temperature, CO_2, and humidity control. Additionally, a motorized xy-table (Märzshäuser, Germany) and a Zeiss Definite focus unit are used to stabilize the focus over time. Thus, the system is capable of imaging multiple positions for several days maintaining *in vitro* culture conditions with a temperature of 37°C, 5% CO_2, and a humidity of 100% and a shift in x-, y-, and z-direction below 1 μm. Limiting factors during the experiments are drift of the coverslip in the dish and the light sensitivity of the cells. To overcome these limitations ibidi dishes were used, in which a glass slide is embedded as the bottom of the dish and the light intensity is chosen as low as possible to reduce the number of photons per cell but at the same time ensure a good image quality by a reasonable exposure time. As the location of the cell on the substrate is of paramount importance to evaluate outgrowth

with respect to geometrical restriction, one combined reference image with fluorescence of substrate-bound protein and phase contrast was acquired. Subsequently, only phase contrast images were taken. The exposure time for the fluorescence image was 500 ms at 100% light intensity of the 470 nm LED while the phase contrast image was acquired every 25 minutes with an exposure time of 200 ms at a voltage of 3.0 V for the light source. To receive detailed information about neuronal outgrowth and the impact of cues to turning events a high resolution was chosen with an image size of 2560 pixel $\times$ 2160 pixels resulting in a frame of 416 μm $\times$ 315 μm (pixel size: 0.163 μm $\times$ 0.163 μm).

3.4 Immunofluorescence

To visualize neuronal cell morphology for individual cell components such as axons and dendrites 18 mm glass coverslips were used to culture neurons for immunofluorescence analysis. After the neuronal network developed for 7 to 14 days *in vitro* the cells were rinsed thrice with preheated PBS prior to fixation for 10 minutes at room temperature (RT) with 4% paraformaldehyde diluted in PBS. Subsequently, the substrates were rinsed three times with PBS and permeablilized with 0.3% Triton X-100 (Sigma) in blocking buffer (BB) (2% bovine serum albumin and 2% heat inactivated goat serum diluted in phosphate buffered saline (PBS) for 10 minutes at RT. Prior to blocking unspecific binding sites with BB at 4°C in the dark overnight, another three rinsing steps with PBS were applied. Afterwards, substrates were rinsed thrice with PBS and incubated in primary antibody solution. For this, antibodies against mcirotuble-associated protein 2 (MAP2) (2 μg/ml, rabbit, Milipore) and Anti-200 kD Neurofilament Heavy (NFH) (2 μg/ml, chicken, abcam) were diluted in BB 1:500 and 1:2000 respectively. A drop of 70 μl of the antibody solution was deposited on a plastic sheet covered with parafilm for every coverslip and the substrates were placed cells down on the droplet. The primary antibody is incubated for 2.5 hours at RT in a wet and dark chamber. Subsequently, the substrates were thoroughly rinsed three times with PBS before they were incubated with the secondary antibody. Here a drop of 70 μl BB with secondary antibodies was deposited on a parafilm covered plastic sheet and the substrates were incubated for 1.5 h at RT in dark wet chamber. The secondary antibodies used for these experiments are goat-anti-mouse Alexa Fluor 633 and goat-anti-chicken Alexa Fluor 546 both diluted 1:500 in BB. Optionally an additional 4',6-Diamidin-2-phenylindol) (DAPI) staining of the deoxyribonucleic acid (DNA) could be applied, thus resulting in a visualization of the following cell components: nucleus (DAPI), dendrites (MAP2), and axons (NFH), as well as the substrate bound protein (FITC). AT last, the incubated substrates are rinsed once with PBS and twice with Milli-Q water be-

fore they are embedded in fluorescent mounting media (Dako) and dried over night. A Zeiss Observer.Z1 equipped with a Zeiss Colibri system, a PCO.edge 5.5 sCMOS camera, and a motorized xy-table (Märzhäuser) was used for images acquisition with ZEN blue software. Resulting images were manually analyzed with respect to axonal and dendritic growth at the gateway between adjacent structures.

3.5 Calcium imaging

Calcium imaging is used to visualize and measure spontaneous neuronal activity on the substrates. Therefore neurons were cultured for 14 to 24 days *in vitro* on 30 mm coverslips in 35 mm Petri dishes, as they provide a large area for stamping and a minimal shift of the coverslip during calcium imaging experiments. Prior to these experiments substrates were rinsed three times with preheated (36°C) extracellular patch solution (E-patch). E-patch contains (mM): $CaCl_2$ 2, HEPES 10, KCl 3, $MgCl_2$ 1, NaCl 120; the pH value of the solution was adjusted with 1M NaOH to a pH of 7.3. In case the osmolarity of the culture medium exceeded the osmolarity of E-patch by more than 10 mOsmol/kg, the osmolarity of E-patch was adjusted to match the value of the medium directly before the experiment with D-(+)-Glucose (Sigma). To visualize neuronal activity optically the cells were incubated with 4 μM Fluo-4 AM (Invitrogen) diluted in E-patch for 45 minutes in the dark at RT. Subsequently, the cells are rinsed twice with warm E-patch (36°C) to remove Fluo-4 that is not taken up by the neurons and to avoid unspecific background signals during the recordings. The final amount of 2 ml E-patch is added to the substrate and an additional rest time of 10 minutes in the dark at RT is applied, which was found to benefit the spontaneous neuronal activity during the recordings. Sequences are acquired with a Zeiss Observer.Z1 equipped with a Zeiss Colibri system and a PCO.edge 5.5 sCMOS camera with 2560 $\times$ 2160 pixels. To achieve a maximal excitation of the dye the intensity of Colibri Light Emitting Diode (LED) ($\lambda = 470$ nm) is chosen with 100%. Time sequences with a length of 15-30 seconds were recorded with Zeiss ZEN blue software at an exposure time of 5 ms and a frame rate of 200 frames per second. These settings exceed the limit of the imaging system at full frame size. Therefore the active area of the sensor that is read out needs to be reduced to facilitate these high speed recordings. Thus, a 2 $\times$ 2 binning was applied and the active area of the sensor was reduced to 512 $\times$ 480 pixels (1.30 μm/pixel) resulting in an image of 665,6 μm $\times$ 624 μm.
At later experiments the exposure time could be increased to 10 ms, as this was shown to be sufficient to track propagating signals on the substrate. Therefore, the frame size could be increased to 1280 $\times$ 586 pixels when 2 $\times$ 2 binning was applied. This results in a frame size of

1,664 μm $\times$ 761 μm, facilitating recordings of multiple gateways and the designed neuroCAP structures, see Chapter 3.1.2. At the same time the recording time could be increased to 40 seconds without increasing the file size . Prior to MATLAB analysis of the sequences the recordings are converted into uncompressed AVI files. Here, it is of paramount importance to adjust the tonal value correction and histogram properly to accentuate the active cells from the background to facilitate meaningful data analysis.

3.6 Data analysis

In the presented thesis three major sets of data were acquired, live cell imaging image sequences, immunofluorescence images, and calcium imaging sequences. For each data set the focus lies on different aspects, thus different methods of analysis have to be applied. Live cell imaging sequences and immunofluorescence images were analyzed manually, whereas sequences from calcium imaging were analyzed automatically. Therefore a script was developed that adapts to image contrast and analysis the direction of signal propagation within and among adjacent populations of neurons. A detailed description of the script will be given in Chapter 4.3.1 including parameter settings and their impact on the results. Most methods are straight forward and intuitive, but others need a more detailed description. Here two methods will be introduced that require a deeper understanding of the theoretical background. First a filter algorithm and some of its parameters will be discussed and second a method to evaluate causalities between different spots on the pattern will be presented.

Savitzky-Golay filter

Time series data from calcium imaging experiments in general are very noisy and the important data is masked behind the high fluctuations of the signal. Thus a reduction of the noise is indispensable, but at the same time the characteristic of the target signal should be influenced as little as possible. As a consequence a moving average filter or even a Gaussian filter are not suitable for this application. Here the Savitzky-Golay (SG) filter comes into play [114]. This filter is based on a polynomial regression in a specified temporal window. The beauty of the SG filter is that the high frequencies are not cut of but included in the calculations. Thereby, relative maxima, minima, and variance are preserved, which would be falsified by conventional filters. An additional trick can be applied that helps reducing the noise while preserving the underlying features of the trace: Bisect the original window size and apply the filter with the resulting window from both sides of trace.

Granger conditional causal analysis

There are different ways to visualize propagating signals and mutual influence between different region of interest (ROI) on a substrate. A very intuitive way is to calculate the delay between occurring activity in the ROIs, but in the end this is not conclusive evidence for a direction of the mutual influence between ROIs. Therefore another method, originating from the field of economics, is more and more used in neuroscience: Multivariate Granger causality analysis. This causality analysis is based on the Wiener-Granger causality test [115], which is a statistical hypothesis test, that can be used to identify whether one time series can be used to forecast another. The test applies for a two variable system **X** and **Y** and is based on the concept of cross prediction. A time series **X** Granger-causes **Y** if the past values of the time series **X** help predicting the future of **Y** with higher statistical significance than the past of **Y** itself. For any time series **X** and **Y** the efficacy of cross prediction can be inferred by the residual error of prediction [116–118] or the magnitude of the predictor coefficients [119] in a linear regression model of **X** and **Y**. To calculate the causality prediction, the multivariate Granger causality MATLAB toolbox provided by A. Seth [118] is used. A vector autoregression is applied in the causality analysis and the computation is limited to a two variable process, neglecting the influence of a third variable **Z** on **X** and **Y** with different lags. This method allows the prediction of the underlying measurable variables, **U**, of the process with the order p by:

$$\mathbf{U}_t = \sum_{k=1}^{p} A_k \cdot \mathbf{U}_{t-k} + \varepsilon_t \tag{3.1}$$

Where A_k are the regression coeficients that represent the predictable structure of the data and ε_t are the residuals that represent the unpredictable structure of the data. For a valid Granger causality analysis equation (3.1) needs to be stable and square summable, requiring $\sum_{k=1}^{p} \|A_k\|^2 < \infty$.
Using a series of t-tests and F-tests on lagged values of **Y**, the prediction error represented by the residuals can be reduced thereby receiving the causal correlation between **X** and **Y**. The multivariate Granger causality analysis MATLAB toolbox is capable of calculating the causalities in time and frequency domains, whereas only the time domain is used in this thesis to visualize the influence on a ROI by surrounding ROI. The work-flow in the script is as follows:

1. **Estimation of model order**: A vector autoregressive model is fited for every model order p up to a chosen maximum and evaluated by the likelihood to find the best model order p.

2. **Vector autoregressive model estimation**: The corresponding model parameters (A_k, ε_t) are estimated for the selected model order.

3. **Autocovariance calculation**: Use the Vector autoregressive parameters to calculate the autocovariance sequence to a suitable number of lags.

4. **Calculation of time domain**: For each conditional causality $F_{\mathbf{Y}\to\mathbf{X}|\mathbf{Z}}$ different aspects are required:

   i Use the full and the reduced regression to calculate the vector autoregression paramters from the autocovariance sequence.

   ii Calculate the time-domain conditional Granger causality.

   iii Testing the significance of the resulting causalities at a given level.

This process results in a matrix with F-test values correlating all ROI with each other as well as matrices of the same dimension indicating the significance value for each entry for a selected significance level. As a consequence, a correlation in dependence of the distance between selected ROIs can be calculated.

4 Results & Discussion

4.1 Culturing small populations of neurons

The first part of this section concerns the successful structuring of adjacent small populations of neurons, where most attention is focused an the protein patterning and the quality of transfer. Within a pattern, the population is supposed to exhibit a high ramification and freely develop in to a mature network. To achieve this network growth the surface need to be coated homogeneously with proteins on a large area compared to the dimension of a single soma. Figure 4.1 shows an image of a CT1 structure [1] in a daisy-chain that is transfered by micro-contact printing to a glass surface. For visualization and control of protein transfer to glass the printed poly-L-lysine (PLL) is fluorescently labeled. The entire area of the structure is covered with PLL and exhibits sharp edges. Inhomogeneities in fluorescence intensity indicate that not all parts of the structure are covered with a monolayer of protein but with multiple layers. A comparison with data from surface plasmon microscopy measurements shown in Figure 2.6 A, reveals that stacks of multilayer can occur within several micrometer in x-y direction. Additionally other artifacts can be spotted on the patterned surface. Small circular holes, cracks and lines reveal defects on the stamp surface induced by handling, storage, or production. Nonetheless these defects do not critically influence neuronal outgrowth, as their dimensions are too small compared to dimensions of the soma and the lack of adhesion promoting protein is barely noticed by the neurites.

Limitations on neuronal growth and the influence of the pattern structure kick in as soon as a neurite, either an axon or dendrite, reaches the edge of a structure. The protein boundary evokes a turning event of the neurite, as a cell attractive area is required for cell adhesion and growth, which is not provided by the cell repellent surrounding of the pattern. In consequence the gateway between adjacent structures needs to be shaped in a way that it funnels axons in one and dendrites in the opposite direction. Therefore, it is essential to structure large areas for network growth and fine structures influencing single cell and neurite growth at the same time with the same transfer efficiency. Stamps either made by PDMS or POP provide the required

[1] See Chapter 3.1.2 for description of structure design.

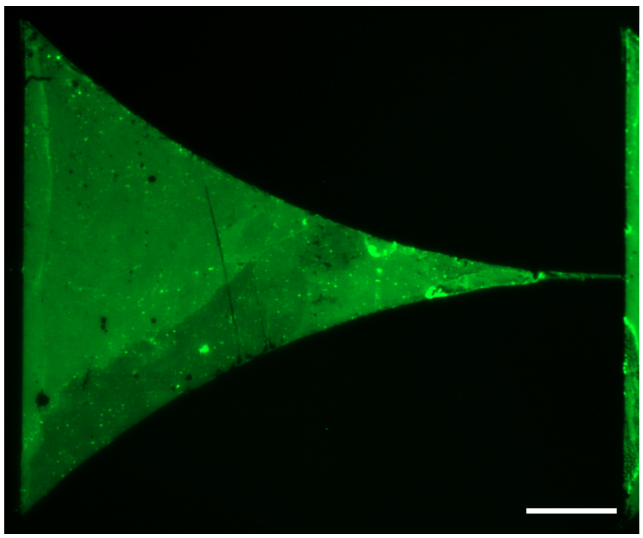

Figure 4.1: FITC labeled protein is transferred by microcontact printing with a POP stamp to a silanized glass surface. All structure details are well preserved and the edges of the protein are well defined. The fluorescence is rather homogeneous and only little defects can be seen such as circular holes and cracks in the pattern. Scale bar: 100 μm

transfer quality on the entire array of daisy-chained structures, spanning a total area of 1 $\times$ 1 cm with feature size down to 2 μm at the gateway of adjacent structures. To ensure this high stamp quality the material needs to be treated carefully to prevent defects in the structures such as cracks. As a consequence, the number of repeated utilizations of a specific stamp is limited, as every use carries the risk of damaging their fragile structures. PDMS stamps can be used up to 10 times before the quality of protein transfer significantly decreases, while for POP stamps this is the case after 8 applications. Also the printing procedure itself requires careful handling. Here, placing and removing of the stamps are the crucial parts in the process, as a heedless placement of the stamp easily results in double printed protein pattern with an offset of several micrometer. The same can occur at the removal of the stamp from the surface. Thus, shear forces need to be avoided at any time during printing and any applied pressure needs to be perpendicular to the surface of the coverslip. For PDMS and POP stamps it is most suitable to approach the stamp slightly tilted to the surface and roll it down starting from the first contact point.

4.1.1 Different stamp materials

Beside pure transfer quality of the protein, also accuracy and false printing is a crucial criteria for successfully culturing patterned populations of neurons. Figure 4.2 A shows the gateway between two CT1 networks on adjacent structures cultured with neurons for 10 days *in*

vitro (DIV). Inside the structure a highly branched network formed connecting neurons within the network. Thick bundles of neurites can be recognized at the edges of the protein pattern that are especially prominent at the gateway, where bundles come from the lower structure and grow towards the upper structure where they fray. However, in this culture severe sagging between laterally separated structures occurred, resulting in cell adhesive areas surrounding

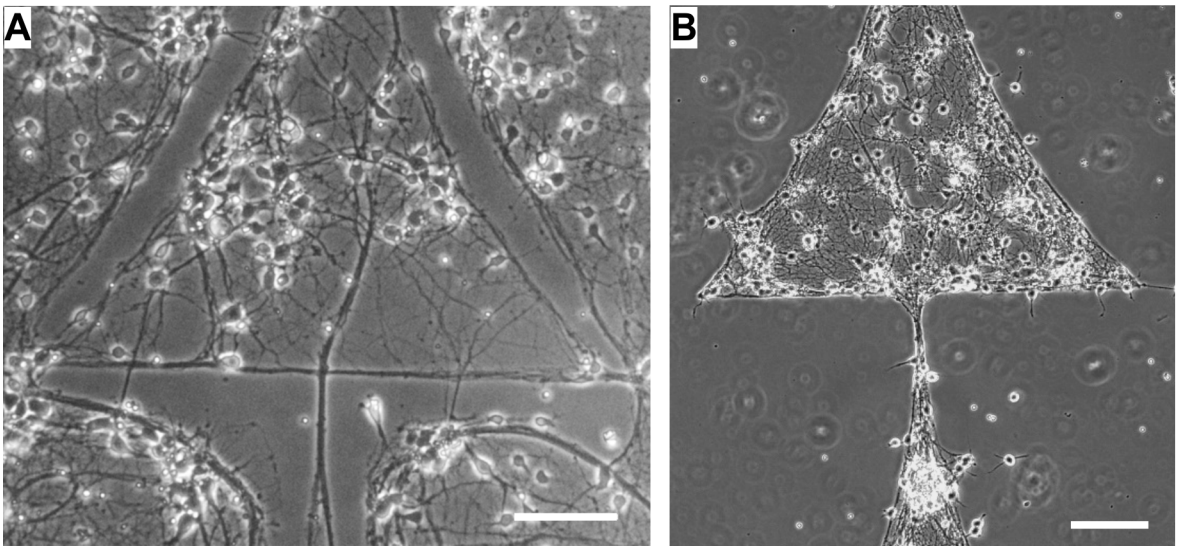

Figure 4.2: Cell growth on pattern printed with PDMS and POP stamps. **A**) 10 DIV old culture on a PDMS stamped CT1 pattern. Severe sagging problems are obvious that impede populations of neurons with predefined gateways. On the protein coated area the cells form ramified networks and neurite bundles at the edges are visible. Nonetheless unintended connections to the surrounding cells are formed that influence neuronal signaling. **B**) Neurons are cultured for 14 DIV on a CT1 protein pattern printed with a POP stamp. Within the structure a ramified network has formed and the neurites stay within the pattern. At the edges of the structure neurite bundle have formed that frame the structure. Scale bars: 100 μm.

the CT1 structures. Neurites show bundle formation at the edge of the intentionally printed as well as sagged protein, while a ramified network is formed elsewhere. Unintentional connections between the surrounding protein and the CT1 structure are formed ruining the controlled connectivity between adjacent CT1 structures.

A clear demarcation between the printed pattern and its surrounding can be observed at the CT1 structure stamped with a POP stamp in Figure 4.2 B, where a gateways between two adjacent structure is shown. After 14 DIV the network formation is similar to that one observed on structures stamped with PDMS. A highly branched network interconnecting the entire population is formed with single cells and some agglomerations of cells. Like with the PDMS patterned substrate, a neurite bundle formation is obvious at the edges, which is more

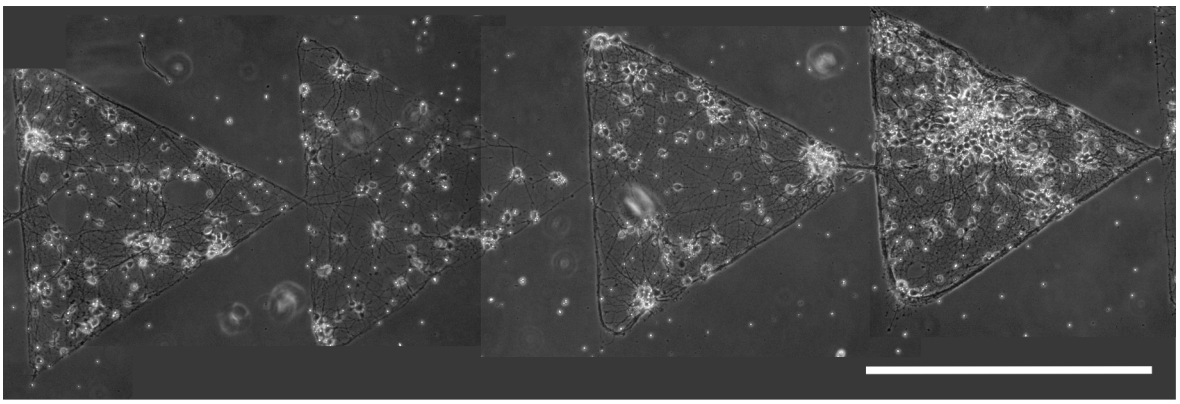

Figure 4.3: Stitched images of four SC1F structures from a daisy-chain of 14 structures after 10 DIV. All populations developed well and formed a ramified network within the structure. Bundles of neurites with different thickness formed at the edge of the pattern. Scale bar: 500 μm.

prominent at some parts of the edge than on others. In the lower left corner another interesting effect can be observed, the bundle growing into the corner of the structure is pulled towards the center of the structure, resulting in a rounded network growth at this point. On the opposing side of the structure the bundle follows the design of the structure and is not pulled in, indicating that proximity to the soma is required to generate this tension, as there are somata present in the left but not in the right corner. Additionally, an incoming bundle can be spotted on the left side of the base of the center structure. This is typically the case, if some cell components or dead cells are located in close proximity to the gateway on the unpatterned surface. These components attract neurites during early stages of outgrowth and mediate cross growth of single neurites and bundles. Due to the quality of transferred pattern and the absence of sagging for POP stamps caused by the fifty fold higher Youngs's module in comparison to PDMS [106], the stamping procedure was switched to exclusive stamping with POP after the first experiments. This results in a reliable patterning of populations of neurons with sharp edges. Figure 4.3 shows tiled images of four SC1F structures after 10 DIV from a column of 14 daisy-chained structures with maintained dimensions of the gateway of 2 μm. All networks were well developed and connected to each other, while the cell density within the structures varies. No sagging or unintended cross growth between separated structures occurs in the lateral spacing between two columns of structures. To prevent cross growing at least a lateral separation of 200 μm is required, otherwise neurites can cross this gap and form connections between two columns. Neurites forming these connections do not show any anchoring points between the columns and are just attached at the edges of the two protein structures. An additional option to prevent cross growth and vaulting between structures is to tune the number

of cells per structure, whereby the best compliance with respect to mature network formation and restricted growth was found empirically and is displayed in Table 4.1. Cell density for SC1 and SC2 structures does not vary much, even though the number of cells per structures is lower on SC2 structures. Interestingly, the density for CT1 and CT2 increased in comparison to SC1 and SC2 but also with respect to each other, where CT2 exhibits a slightly higher cell concentration; thus potentially resulting in a denser network and a higher connectivity. Nevertheless the low number of cells found for CT2 structures might influence the cellular activity, as a certain number of cells is required to generate spontaneous activity covering the entire population. For a synchronized activity with a low interval between two burst events at least 15 cells are required on a CT2 structure. This value is comparable to those values reported by Yamamoto and colleques [120, 121]

Table 4.1: Average number of cells on the substrates and the resulting cell density.

Structure	Number of cells	n	Cell density [cells/mm^2]
SC1	66 ± 12	19	266 ± 48
SC2	42 ± 15	19	254 ± 91
CT1	39 ± 12	19	347 ± 109
CT2	31 ± 7	21	457 ± 109

4.1.2 Influence of serum containing medium on cell growth

Nervous tissue *in vivo* consists of the same amount of neurons and glial cells [9], while our *in vitro* cultures are glial free or at least contain a low number of glial cells. Thus the environmental conditions for neurons are different and as a consequence it is expected that they might behave differently. To overcome this potential limitation culture conditions were optimized by adding fetal bovine serum (FBS) to the medium in varying concentrations (0.5%, 1%, and 2% FBS in culture media) and at variable points in time. FBS has a low level of antibodies and contains more growth factors, which promote cell maturation not only in neuronal but also in glial cultures [122]. Thus the network formation and the establishment of connections between adjacent populations could be improved, but on the other hand the proliferation rate of glial cells increases with serum containing medium. On homogeneously coated substrates this is not an issue, but on substrates with patterned substrate-bound proteins with fine structural features that aim for defined connectivity this might cause problems. Proliferating glial cells are not as strictly restricted in outgrowth by the pattern as neuronal cells, and hence overgrow small features and offer anchoring points for neuronal cells which undermines the defined con-

nectivity. To tackle this problem 0.01% 5 mMol arabinofuranosyl cytidine (Ara-C)[2] was used to reduce glial proliferation, but at the same time neurons were negatively affected by Ara-C. Here, the application of different amounts of Ara-C at different points in time during culture was tried. At all attempts to block glial proliferation with Ara-C neurons were suffering and did not show spontaneous activity or died prior to measurements.
In the test it could be shown, that the time for maturation of a neuronal network and even manifestation of spontaneous action potentials within the population could be decreased from 21 DIV to 14 DIV with comparable activity by adding 0.5% FBS to the culture medium. However, at the same time the number of glial cells increased drastically, making this approach unfeasible for populations of neurons patterned with microcontact printing. Even additional Ara-C could not improve the situation as the neurons suffer from this medication and show apoptosis. Concluding that this approach is suitable for homogeneous cultures or microfluidic systems but not for microcontact printed substrate bound protein patterns.

[2]Ara-C is mainly used in treatment of cancer by interfering with the DNA synthesis [123].

4.2 Protein patterning and neuronal outgrowth

4.2.1 Axonal turn angle

To discriminate neuronal outgrowth induced by pattern geometry two different sets of samples were investigated in live cell imaging experiments: substrates with homogeneous and CT1 patterned substrate-bound protein. For both sets the same protein solution was used and the same amount of cells was seeded, see Chapter 3.2. Neurons under both culture conditions were investigated with respect to their axonal turn angle and changes occurring in these angles over time. To elucidate changes in axonal turn angles over time, images of neuronal outgrowth were acquired every 0.5 DIV. In every image the axonal path was reconstructed with individual lines and the angle α between two adjacent line segments was determined with ImageJ, see Figure 4.4. Resulting angle distributions were mirrored at 0° as the obtained $\alpha \geq 0$ and the distribution of turning angles is assumed to be symmetric. On homogeneously patterned substrates the axonal development could be followed up to 5 days *in vitro*, whereat patterned substrates only offered the chance to investigate neurite growth for 2 DIV. At later stages it was impossible to differentiate axons and dendrites without any imunohistochemical staining to distinguish different cell components.

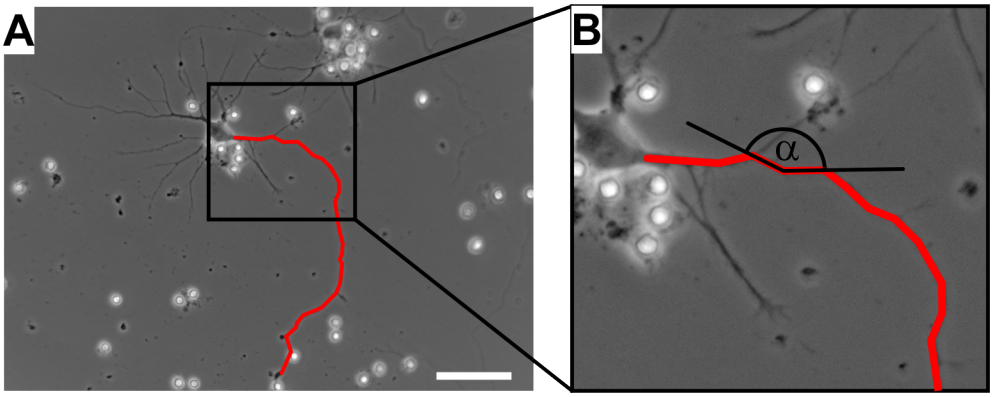

Figure 4.4: Draft of the analysis of live cell imaging data from neurons grown on homogeneously coated substrates. **A**) Lines that reconstruct the path of the axon were drawn. Scale bar: 50 μm. **B**) Measuring the angle α between two axon reconstruction lines that meet.

Homogeneous growth

Neurons cultured on homogeneously coated substrates are not restricted in their direction of outgrowth. They can exhibit every possible turn angle and just underlie internal changes

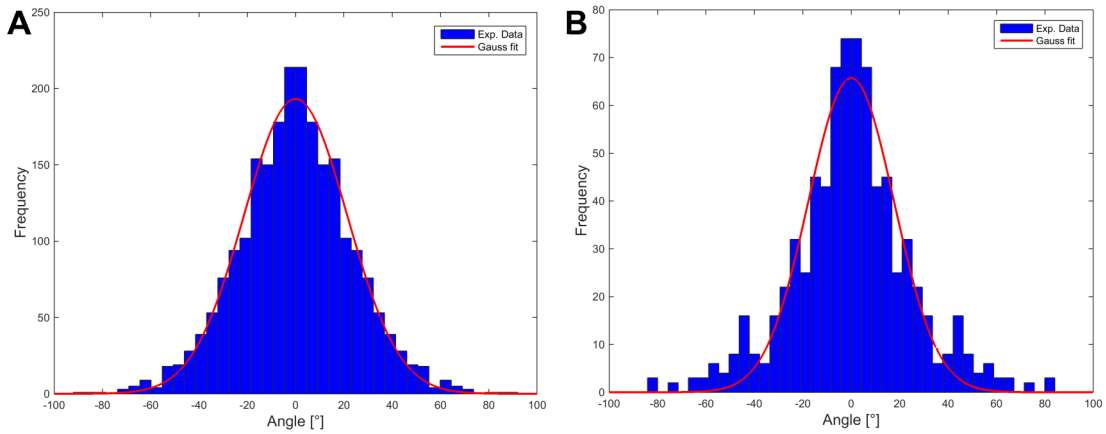

Figure 4.5: Comparison of axonal turn angles on homogeneous and patterned substrates. **A**) Turn angle distribution of axonal turn angles of neurons grown on homogeneously coated substrates for 4 DIV. The σ-interval of the Gaussian distribution is $\sigma = 21° \pm 2°$ with a $\chi^2 = 0.98$. **B**) The over all turn angle distribution of axons growing on a CT1 pattern for 2 DIV is considerably narrower $\sigma = 17° \pm 1°$ with a $\chi^2 = 0.92$ than that for homogeneously patterned substrates.

and limitations inside the axon. For this survey only single neurons were selected, as they offer a clear differentiation between axons and dendrites during their elongation process. At the beginning of the outgrowth a broader regime of axonal turn angles appears that slightly narrows over time. After four days *in vitro* the turn angle distribution (Figure 4.5 A) is similar to the normal distribution, which is confirmed by the fit parameters for the normal distribution with $\chi^2 = 0.98$ and the full width half maximum is determined to be $\sigma = 21° \pm 2°$. This narrowing of the measured angle range can be attributed to internal processes inside the neuron [124–127]. In the initial state of elongation microtubules inside an axon are cross-linked to each other and are not parallel near the growth cone. During protrusion a force pointing towards the direction of growth cone elongation is generated, that transfers to the microtubule, resulting in a stretching of the axon. This lengthens the microtubules and aligns them almost parallel. More importantly this effect is not locally restricted to the part of the axon adjoining the growth cone but transfers to the entire axon. As a consequence turn angles narrow as a result of the new alignment of the microtubules inside the axon.

Beyond that, axons approaching a contact partner, with which they form connections, could be observed. But more interestingly, it could be followed how the polarity of a neuron changed. An axon from a neuron A elongates toward one direction without reaching any contact partner. At the same time a dendrite of the same neuron gets in proximity to another neuron B. At this point the primary axon retracts and the dendrite in proximity to the neuron B rapidly elongates (see Figure A.2 in the Appendix) in this way the polarity of the neuron was changed.

Patterned culture

Neuronal growth on patterned substrates was investigated starting at 1 DIV. Until this time the cells subsided and started their development already resulting in premature neurons that exhibit a clearly visible axon. Figure 4.6 shows the representative development of a neuronal culture on CT1 structures starting from DIV 1 in 0.5 DIV steps till 3.5 DIV. The green lines indicate the edge of the protein structure, reconstructed from a reference image of the FITC labeled PLL that was acquired directly before the live-cell imaging experiment. In the first stage the axons sprout and elongate in the same direction during the first 1.5 days *in vitro*. Whereat after DIV 1.5 an axon crosses the junction from the lower to the upper structure, see white arrow in Figure 4.6 B. In the following days this axon branched and the new sprays grow in a meandering structure in different directions to find contact partners. At the same time, the neurons in the upper structure react to the incoming axon and approach its sprays. After 2.5 DIV it is virtually impossible to differentiate between axons and dendrites on the structures. But what can be clearly recognized is a stretching of some neurites, which are presumably axons, as could be observed on homogeneously coated substrates. Another interesting effect that can be monitored in this example culture, is the migration of neurons on the pattern and the impact of the pattern. It is not only the neurites searching for the most adhesive substrate areas and contact partners, but is also the somata changing their position for a more profitable position. A prominent example is the neuron at the right side, marked with a white circle. This cell moves approximately 50 μm within 2.5 days to the edge of the structure, where its neurites follow the pattern. Also the axon that pierces through the gateway from the lower structure, grows at the edge of the lower pattern, indicating the attractiveness of protein boundaries.
Analyzing the turn angle changes of the axon during elongation results in a turn angle distribution for the different points in time that are shown in Figure A.3 in the Appendix. The analysis was only performed until DIV 2 as a differentiation of axons and dendrites could not be performed after that stage of development. It can be seen that the distribution for the angle is wide and not uniform at the beginning and becomes narrower and more uniform for later points in time. Summarizing the turning angle of all axons growing on the pattern to one histogram plot results in a turn angle distribution that is shown in Figure 4.5 B. Here, the distribution is narrower than the one on homogeneously coated substrates, what can be determined by the characteristics of the fitted normal distribution. The fitted data match very well ($\chi^2 = 0.92$) to the experimental data. The sigma-environment is decreased by almost 4° in comparison to homogeneous cultures, down to $17° \pm 1°$. This result is unsurprising, looking at the axon piercing from the lower to the upper structure and the neurites, that follow the edge of the protein pattern. These external cues influence neuronal outgrowth and direct the axons

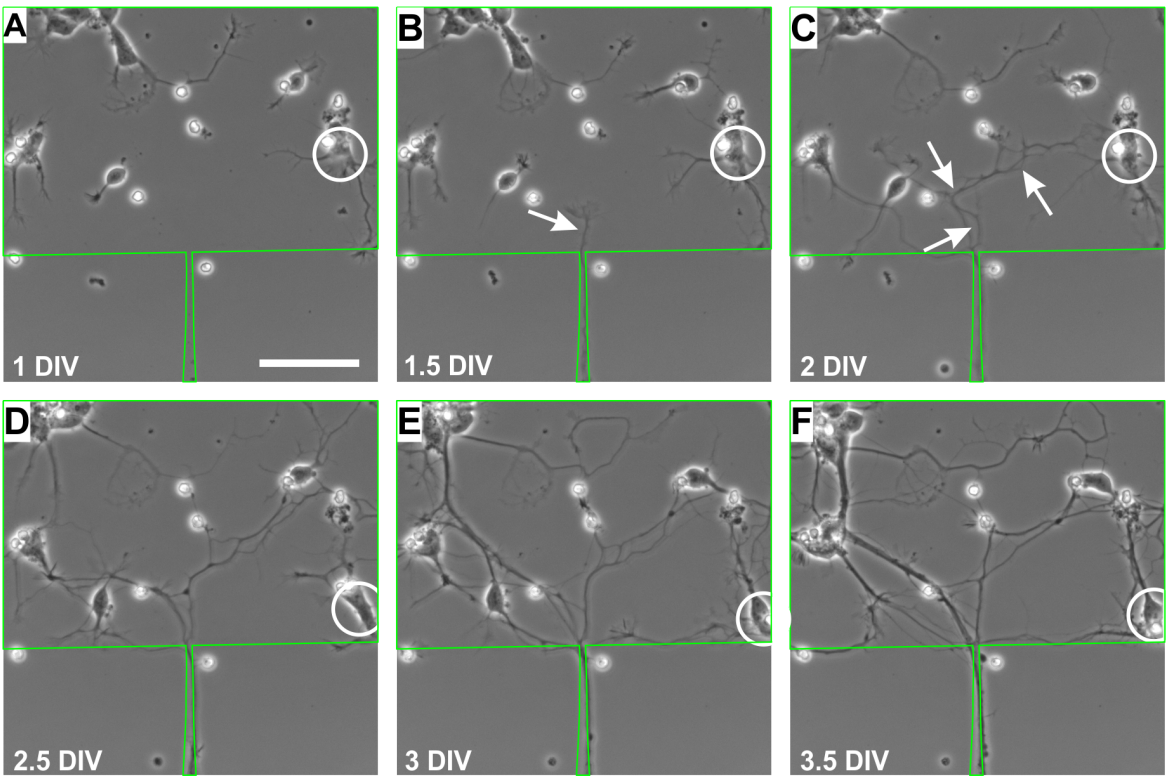

Figure 4.6: Images from live cell imaging of neurons at the gateway of a CT1 structure indicated by the green lines. Pictures were consecutively taken after 1 DIV, 1.5 DIV, 2 DIV,..., 3.5 DIV. **A**) All neurons formed neurites and axons are sprouting from the soma. **B**) Axonal elongation starts and an axon pierces through the gateway into the upper structure, see white arrow. **C**) The axon from the lower structure branches and the growth cones search for contact partners (white arrows). During this process the axon exhibits a meandering structure. **D**) - **F**) The sprouting axon reaches contact points and reduces its meandering structure. In the end, the axon coming from the lower structure almost consists of straight lines and the total number of turning points is reduced. Scale bar: 50 μm

to a straighter growth, but it remains unclear if the different neurites are influenced differently. A clear downside of this method for analyzing the axonal path is that numerous turn events with small angles are undetected as they might be overlooked during path reconstruction. To overcome this downside, a constant segment length could be used for reconstruction but this approach would not consider varying segment length between two turn events. Thus, it is questionable if the results of constant segment analysis are conclusive and provide additional information. To respect varying growth rate during axonal elongation, segments with variable length are used to reconstruct the axons, accepting an under-representation of small variations in direction.

Simulation of neuronal growth

When it comes to experiments that require the extraction of animal tissue, ethical issues arise and the number of animals should be as low as possible. To reduce the amount of rats that have to be killed for the investigation of signal propagation among populations of neurons an *in silico* model could be generated. With the help of this model the optimal parameter for neuronal outgrowth and could be simulated and later validated in *in vitro* experiments. There is a variety of scientific approaches to this topic and two of the major platforms are NETMORPH [128] and NeuVision [129] that mainly feature 3D network formation. But for the desired application a 2D network with boundary conditions is required. NETMORPH officially features the growth of two dimensional networks, but it is shown in the master thesis of Dennis Lenthe, that the full functionality of neurite growth and synapse formation is not given in 2D [130]. However, the axonal growth in the framework is one of the crucial points, as it is suspected to determine the connectivity between adjacent populations. Therefore different axon growth models were investigated, that should exhibit a similar behavior to what was described in the previous paragraph. As a consequence one might want to apply a model, where the axonal turn segment angle is distributed like depicted in Figure 4.5. On the other hand this model does not represent the internal tension of the axon that lead to the sketch in Figure 4.7 of the history model to evaluate the length and orientation of the next segment. The impact of the last segments before the turn event straightening of the axon. Therefore NETMORPH suggests a history model for axonal growth that is depicted in Figure 4.7 A. The

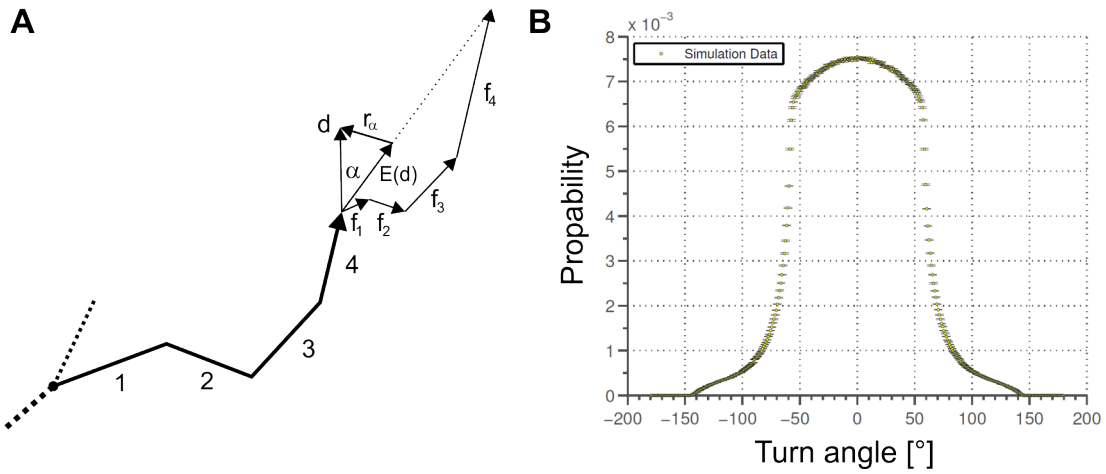

Figure 4.7: History model of axonal growth. **A**) The orientation of previous segments is weighted and combined with drawing an angle α from a distribution leading to a new segment d. **B**) Resulting turn angle distribution for the applied history model. The highest probability appears for a straight growth and a wide angle regime is accessible for turning events. Figure adapted to Lenthe [130].

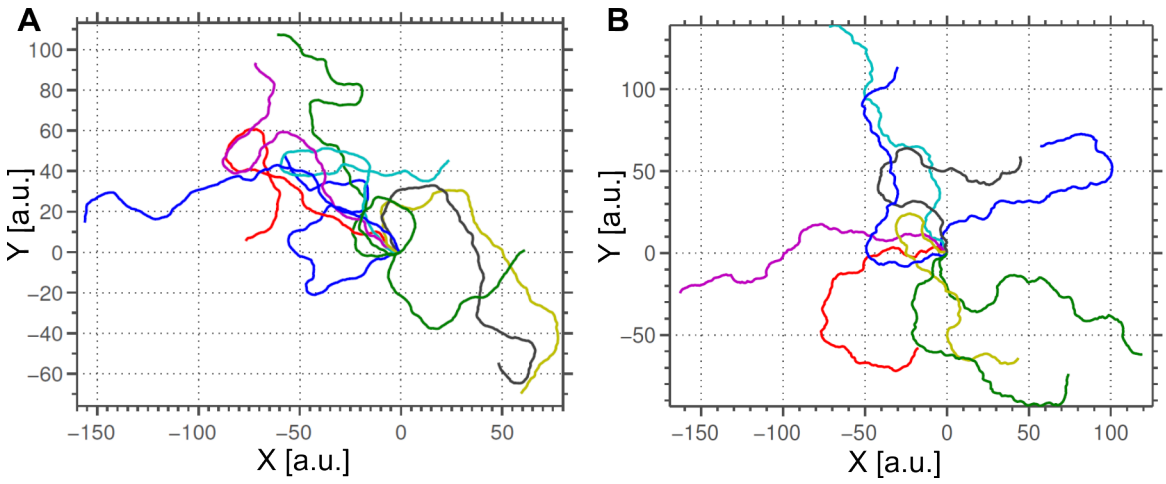

Figure 4.8: Trajectories of modeled axonal growth. **A**) Restricted walk: The segment length is fixed and the turn angle is drawn from a normal distribution. **B**) History walk: The history of the walk influences the orientation of the next segment. Figure adapted to Lenthe [130].

axonal elongation is separated into individual segments and a turning event occurs at the end of every segment. To determine the orientation of the next segment an angle α is drawn from a distribution. In addition the last segment steps are combined to a weighted vector, where the weight of the individual segments decreases with the distance. This results in a history vector E(d). The combination of the history vector and the drawn angle results in the final segment d and its orientation. Considering this history model the turn angle distribution shown in Figure 4.7 B results. This distribution varies by changing the number of history segments and the impact of the individual segments considered in the calculation. For a detailed description see the master thesis of Dennis Lenthe [130].

Applying a random walk, where the orientation of the next segment is drawn from a Gaussian distribution, results in trajectories like those shown in Figure 4.8 A. The axons grow quite straight, but some harsh turn event occur that do not look physiologic. Also loop formation can be observed, where the axon forms a turn and crosses its own trajectory. In contrast, the axons resulting from a history walk, shown in Figure 4.8 B, are not as smooth as those from the restricted walk but their over all orientation is straighter in comparison to those in A. But over all the results of both walk simulations appear to be similar and it is legit to use the history walk model to generate a network. So far a simulation of a complete population of neurons on a patterned area could not be performed and thus the aim to reduce the use of animal tissue is still out of reach. However, first steps are made towards its reduction even though a lot of afford has to be spend to develop and implement a reliable software tool that can partly replace

animal tissue.

4.2.2 Impact of pattern geometry on neuronal outgrowth

Live cell imaging experiments revealed that the neurites show the tendency to follow the edge of a structure, while it remained unclear whether axons or dendrites are preferentially guided by the boundary of the pattern. Thus immunohistochemical staining of neurons against mcirotuble-associated protein 2 (MAP2) and Anti-200 kD Neurofilament Heavy (NFH) were performed to visualize dendrites and axons, respectively. Figure 4.9 shows representative images of neurons growing in the proximity of the boundary of a protein pattern. One thick bundle of neurites is prominent in the phase contrast image, which forms a border between a ramified network on the one side and no cell growth on the other. Based on the immunohistochemical staining axons and dendrites can be identified on the FITC labeled protein pattern,

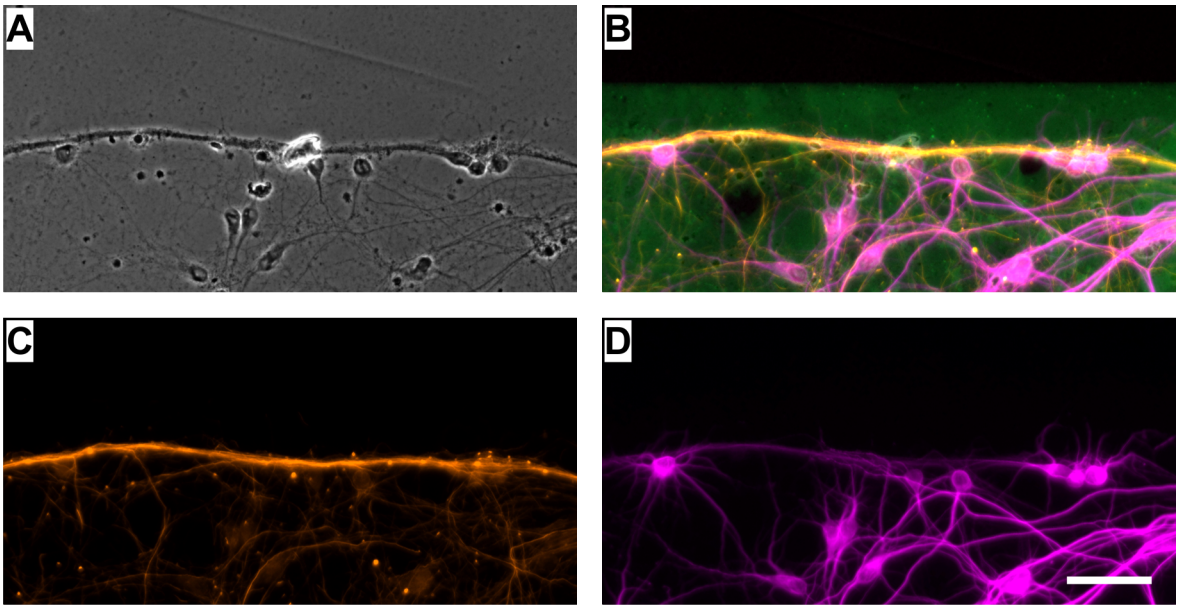

Figure 4.9: Neuronal growth at the edge of a protein pattern after 14 days *in vitro*. **A**) Phase contrast image of of the boundary of a protein pattern. A thick bundle of neurites is formed while a ramified network is exhibited in the lower part of the structure. **B**) A merged image of immunohistochemical staining of the neuronal culture in A. The printed protein is FITC labeled (green). Axons are visualized by Anti-200 kD Neurofilament Heavy (NFH) (orange) and dendrites by (MAP2) (magenta). **C**) Axons (NFH) form the major component of the bundle growing in proximity to the edge of the structure, but also generate a ramified network with fine protrusions. **D**) After 14 DIV dendrites form a less ramified network in comparison to axons, but exhibits an interconnecting mesh of branches, restricted by the pattern. Scale bar: 50 μm

see Figure 4.9 B. Interestingly the bundle is not located directly at the edge of the protein structure but some 20 to 30 μm away. Comparing these observations after 14 DIV with those from live cell imaging after at least 4 DIV, where the neurites tend to grow along the boundary, a change in growth behavior can be seen, which indicates that the network within a population exhibits an internal force pulling the neurites towards the center. Nevertheless, the images identify different outgrowth characteristics for dendrites and axon. Axons form a uniform and highly branched network within the pattern but at the edge they bundle up and follow the boundary, see Figure 4.9 C. Dendrites in contrast do not exhibit a comparably ramified mesh, but uniformly cover the pattern. At the same time, dendrites are not as attracted to the edge as the axons, see Figure 4.9 D. Motivated by these results, it can be speculated that a different behavior for axons and dendrites can be observed at the gateway of the structures and that the design of the junction might influence their outgrowth differently.

4.2.3 Gateway design impacts neural development

Elucidating the impact of different gateway geometries on the outgrowth of dendrites and axons was performed via immunohistochemical stainings of neuronal cultures after 6 to 14 days *in vitro*. Acquired images were analyzed with respect to the orientation of axonal and dendritic outgrowth at the gateway. Here, only those with cell growth on the pattern were counted. Junctions at which neurites vault unpatterned surface for a distance larger than 30 μm were not included in the survey, as an influence from the structure on neuronal outgrowth can not be granted. Neurite growth at the gateway is classified into three categories according to nomenclature introduced in Figure 3.2: lower $\rightarrow$ upper; upper $\rightarrow$ lower; both. Wherein, the first two categories only apply if there is exclusive growth of axons or dendrites in the distinct direction. If axons or dendrites grow in both orientations at the same time, the growth of the axons and dendrites is assigned to the third category. Neurites on both sides of the gateway are affected differently by the gateway geometry. As can be seen in Figure 4.10, an axonal bundle pierces through the junction from the lower to the upper structure where it roves. While at the same time the axons in the upper structure form a ramified network with a roving bundle approaching the gateway but these grow across the connection of the two adjacent structures without entering the funnel of the lower structure. At the same time, the dendrites also exhibit branched outgrowth but in contrast to the axons they converge on the gateway and show a tendency to enter the funnel from the upper to the lower structure.

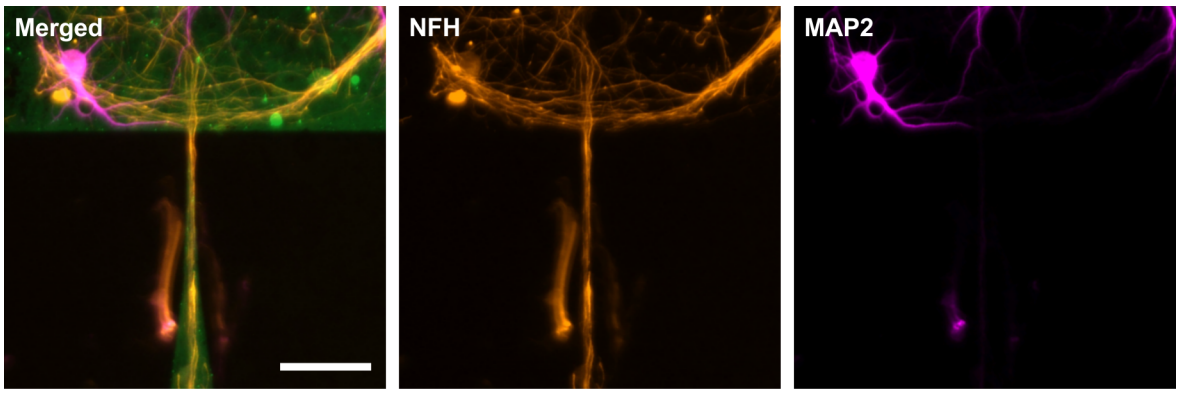

Figure 4.10: Neurite growth at a CT1 gateway after 14 days *in vitro*. The merged image shows the arrangement of the axons and dendrites on the protein pattern (green). **NFH** staining displays the axonal growth on the structure and **MAP2** staining visualizes dendritic growth. Scale bar: 50 μm

Impact on Dendrites

MAP2 staining of neuronal cultures on all four different structures reveals that the SC and CT structures manifest different influences on dendritic growth at the gateway. Unswayed by gateway geometry, the network formation within the structure is similar for all structures. However, the different opening angles strongly impact the orientation of dendritic growth. SC1 structures show a low funneling effect for the dendrites, which vault across unpatterned areas towards the adjacent structure, see white arrow in Figure 4.11. With this vaulting, the influence from the protein structure is reduced, as exclusive cell growth is lost and uncontrolled, or rather unintentional, connections are formed. A similar situation can be found for SC2 structures (white arrow in Figure 4.11), where dendrites also vault the uncoated area resulting in undesired connections. This vaulting effect results from two competing protein patterns, the funnel restricts the direction of outgrowth of the dendrites while the upper structure attracts the dendrite at the same time. As a consequence, the dendrite leaves the funnel in proximity to the gateway and crosses towards the adjacent pattern. For vaulting in the opposite direction the presence of a soma in the lower structure in proximity to the gateway is required. Neurotrophic factors, secreted by this neuron, attract axons and dendrites from the upper structure to cross uncoated area to form a connection. In contrast to the SC structures, both CT structures show a clear funneling of dendritic growth without any noteworthy vaulting of dendrites across uncoated areas. All dendrites growing on these structures are concentrated at the fine tip of the structures. Nevertheless the percentage of dendrites growing from lower to the upper structure does not vary too much for SC1, SC2, and CT1, see Figure 4.12. These three structures show 53 - 58%, while the CT2 design exhibits 40% guidance of the dendrite in the

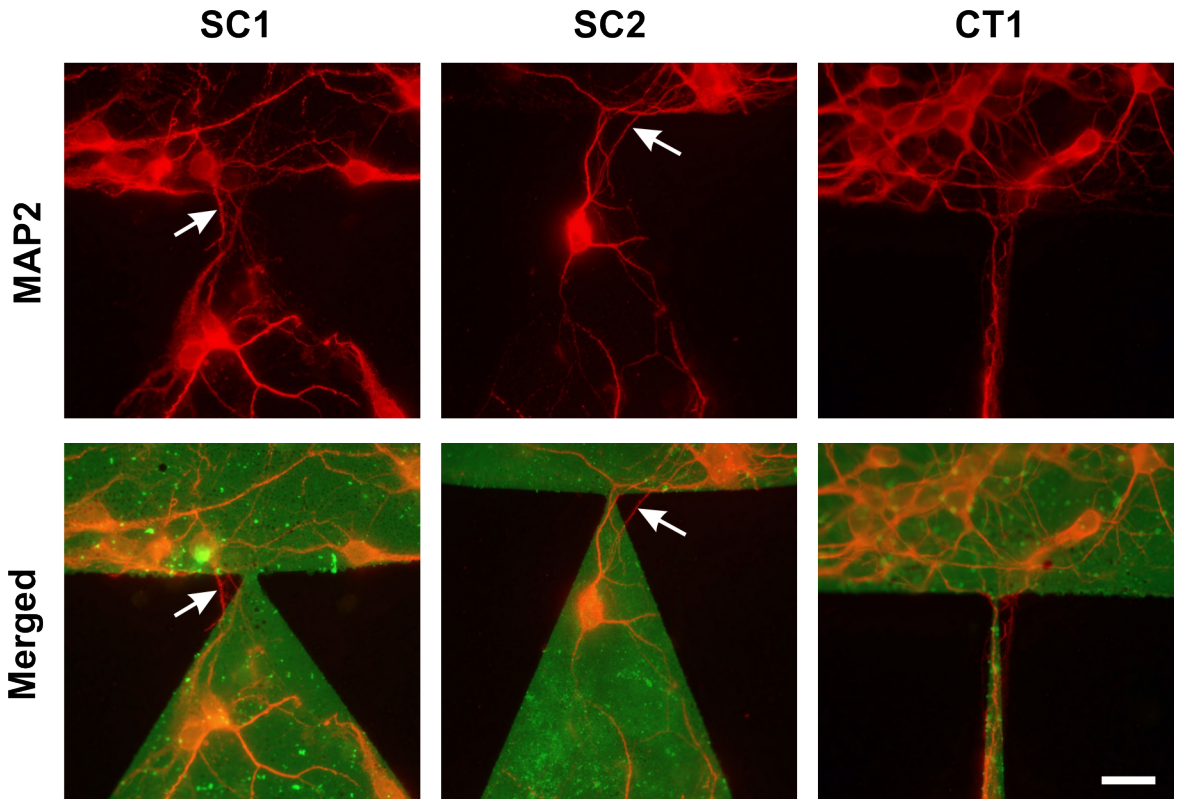

Figure 4.11: Dendritic growth at the gateway of different structures after 6 days *in vitro*. **SC1** Dendrites form a ramified network on the structures on both side of the gateway but they vault up to 30 μm of unpatterned area, see white arrow. **SC2** Neuronal growth is stronger funneled in comparison to SC1 structures, but still vaulting of unpatterned areas, indicated by the white arrow, occurs. **CT1** A clear focusing effect occurs at the funnel for the dendrites from both sides of the gateway. Scale bar for all images: 50 μm

direction lower to upper.

In contrast, for the opposite direction the situation changes, where the percentage of dendrites growing from upper to lower structure is at most 25% for SC structures while at least 34 - 40% of the dendrites on CT structures sprout in this orientation. For the third category (both) there is not much of a difference for all four structures. Exclusively evaluating dendritic growth there are weak reasons to speculate about a directionality of signal propagation induced by dendritic growth.

Impact on Axons

Including the axonal growth in this consideration offers a new perspective. In contrast to the dendrites axons are affected differently by the diverse gateway designs. The impact on axonal

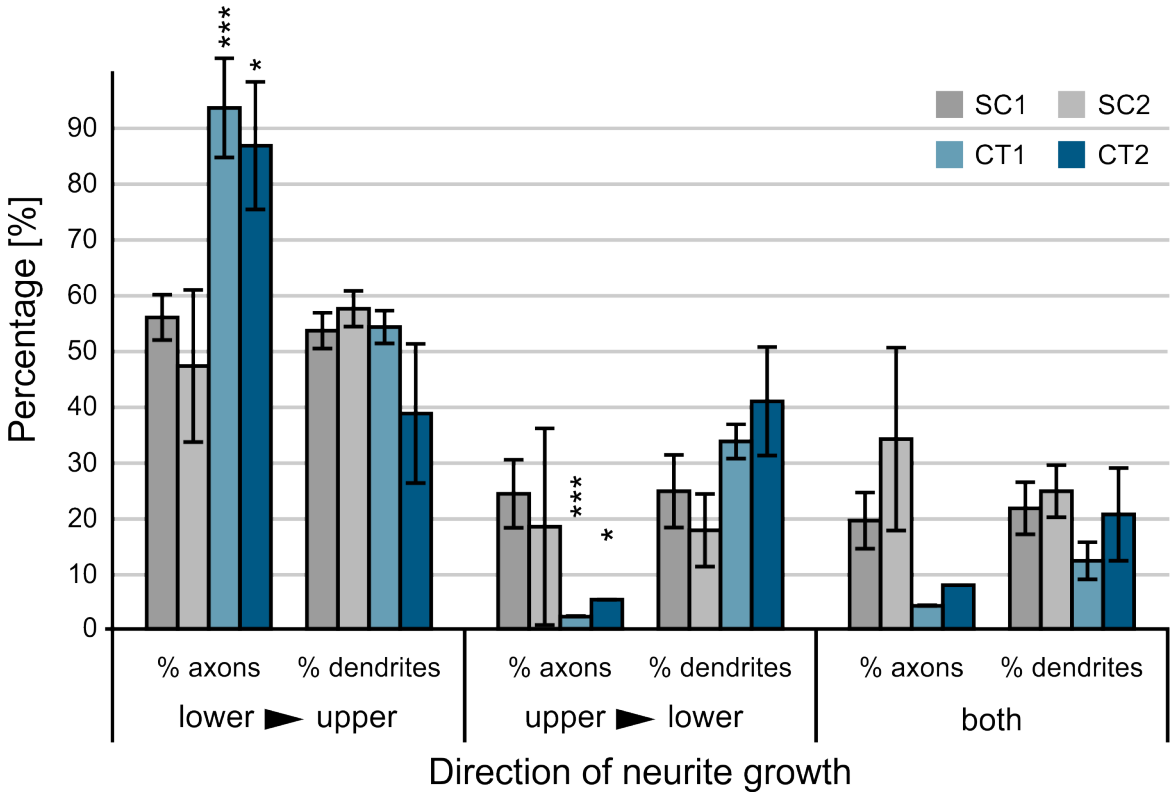

Figure 4.12: Orientation of axonal and dendritic growth at the gateway of adjacent structures. Immunohistochemical stains of axons and dendrites after 6 - 14 DIV were analyzed with respect to the direction of neurite outgrowth. Significant differences of dendritic and axonal growth within one orientation are marked: ***: $p < 0.001$, *: $p < 0.05$.

growth, induced by the CT structures varies drastically for individual orientations, but not among CT1 and CT2 structure designs. Axonal growth from the lower to the upper structure is promoted up to 92% in comparison to the other orientations, see Figure 4.12. Significantly less than 10% of the axons grow in each of the other directions. Here, the curved form of the flanks and the needle like tip of the structure collect the bundles of axons and funnels them towards the junction.

At the same time the axonal growth on SC structures exhibits a completely different behavior in comparison to the CT structures. Independent of the opening angle the influence of the SC structures to funnel the axon to the tip and guide them from the lower to the upper structure is as distinct as the guiding of the dendrites. Even though the degree of impact on axonal and dendritic growth for the individual direction on the SC structure differs, it remains similar for both neurites within one orientation, see Figure 4.12. Additionally, not all axon bundles growing at the edge of the SC structures reach the tip of the funnel, but turn around and grow in the opposite direction at the other flank of the structure. This effect is more prominent on

SC1 structures than on SC2 and reduces the possible number of connections formed between adjacent populations. For both CT structures in contrast this behavior could not be observed.

Conclusions on structure design

Gateway design is of paramount importance to gain a specific guidance of axons in contrast to dendrites. Based on the findings discussed in previous sections and displayed in Figure 4.12 it is obvious that a thin needle like tip, like the one used by CT structures, is highly selective for the direction of axonal outgrowth. For both orientations lower $\rightarrow$ upper and upper $\rightarrow$ lower a significantly different impact on axonal and dendritic growth by the structure can be seen, CT1: $p < 0.001$ and CT2: $p < 0.05$. This different behavior of axons and dendrites can be understood by the effect seen in in Figure 4.9 and 4.10, where axonal bundles follow the edge of a pattern and thus are collected by the funnel. The shape of the edge of the protein pattern evoked by the geometry of the funnel and the base of the adjacent structure transfers to the growth of axon bundles as they were shown to follow and adopt the form of the edge. This is a possible explanation for the selective cell growth as the prior orientation of the cytoskeleton highly impacts the outgrowth direction of the axon by a tension generated by microfilaments and microtubules [31,124–127,131]. The turn angle distributions on homogeneous and patterned substrates shows axons preferably turn with a lower turn angle and harsh turns are rather unlikely. As a consequence, it is more than comprehensible that axons growing in the upper structure of a CT gateway just enter the funnel at most 5% of the same time. SC structures are constructed with an opening angle of 60° or 30° and thus the turn angle for axonal growth is between 90° and 60°, or rather 75°. Turn events with these angles are not as unlikely as those for the CT structures and thus a higher number of axons growing from upper to lower structure is explainable. To overcome these limitations and to achieve a high selectivity of axonal growth also for SC structures, additional semicircles were added as features at the base of the SC and CT structures, see Figure A.4 in the Appendix, to increase the area of growth for every population. Furthermore the above described internal tension was intended to yield additional guiding of axons at the base of the new structure, as axons growing on the edge of a semicircle would be directed towards the center of the population. Unfortunately, the added features did not show the desired effect on axonal growth. Quite the contrary, neurites vault the distance between the semicircle and the tip of the lower structure and form undesired connections between the two structures.
Additionally, different base curvatures were investigated, as depicted in Figure A.1 in the Appendix. Here, the intention was to determine whether or not a different orientation of the curvature has an impact on the growth of neurites between adjacent structures. Apparently

the curvature of the different designs was not strong enough to impact the internal tension within the axons such that the orientation of their outgrowth is changed. As a consequence, the original structures SC1, SC2, CT1, and CT2 were used for all experiments performed in this thesis, see Figure A.4 in the Appendix.
At the bottom line one might be mislead to conclude to design thin triangular structures with a needle like tip and an opening angle of 6° or less, such as the tip of a CT structure. But as a consequence the growth area of the structures would drastically decrease and a network formation would be impeded, resulting in line like structures [85, 86, 89]. Thus, curved sides have been implemented to increase the growth area and allow ramified network formation with a defined junction between adjacent populations of neurons. In the experiments an aspect ratio of height/width of 1 - 1.2 appeared to be best suited for network formation [33]. For higher values the total number of cells within a population is to low for the formation of a vital network that generates spontaneous neuronal activity and a long term stability in culture. With the performed investigations in this thesis it is not possible to give a critical number of cells, but the observations showed that populations with 10 cells on a CT2 structure showed a significantly lower firing rate than those populations with 20 or more cells on the same pattern design. On the other side, aspect ratios below 1 can not achieve directed cell growth at the gateway. The mean population per pattern type that exhibit reliable spontaneous activity with a good firing rate are: SC1: 66, SC2: 42, CT1: 39, and CT2: 31. Additional approaches to increase the area of the structure by maintaining the guidance characteristic at the same time, see Figure A.4 in the Appendix, were not prosperous, as additional features lead to unintended vaulting to span a gap of up to 100 μm.

4.3 Patterned cultures and neuronal activity

Neurons were cultured for 14 to 24 days *in vitro* on patterned substrates until they matured and exhibited spontaneous activity that covered the entire population. The direction of propagating signals among adjacent populations of neurons is revealed by optical recordings of action potentials. Therefore neurons are labelled with a calcium sensitive dye for visualizing changes in intracellular calcium concentration by changes of fluorescence intensity. The concern of this chapter is the analysis of acquired time sequences from optical recordings, including critical parameter during event extraction and correlation. Moreover, the impact of pattern geometry on directed signal propagation will be presented and discussed.

4.3.1 Optical recordings

The number of video sequences obtained from calcium imaging experiments performed for this thesis reached a level, at which it is not wise to perform the analysis manually. In addition, an automated analysis is independent of user bias and leads to more comparable results. Of course, human perception is tuned to identify patterns, which makes it perfect for image recognition. On the other hand the recognition of small intensity changes in separated frames and a quantitative analysis is impractical for the human visual system. Therefore, intensity analysis has to be done based on a digital analysis software. Regions of interest (ROIs) for intensity analysis can be selected manually or automatically. As a manual selection is very tedious, caused by the sheer number of recorded sequences ($n > 400$) and a number of ROIs to be selected for every sequence, it is wise to conduct automated sequence analysis. Thus, one part of this thesis was the development of a script for automated sequence analysis based on MATLAB. This script will be presented in the following chapter in full detail and applied parameters will be discussed. But first the work-flow of the script, as shown in Figure 4.13, is depicted, followed by a detailed description of the applied methods.

A)**Data import and selection of active traces**: Read AVI files to current work-space and find time traces that exhibit fluorescence intensity changes induced by neuronal activity that is above a certain threshold. Traces with above threshold intensity are considered as active traces.

B)**Smooth and normalize time traces for event detection**: Time traces show high frequency fluctuations of fluorescence intensity. These fluctuations need to be reduced for reasonable analysis. At the same time a normalization of intensity values is performed for better comparability across individual traces. Changes in fluorescence intensity in-

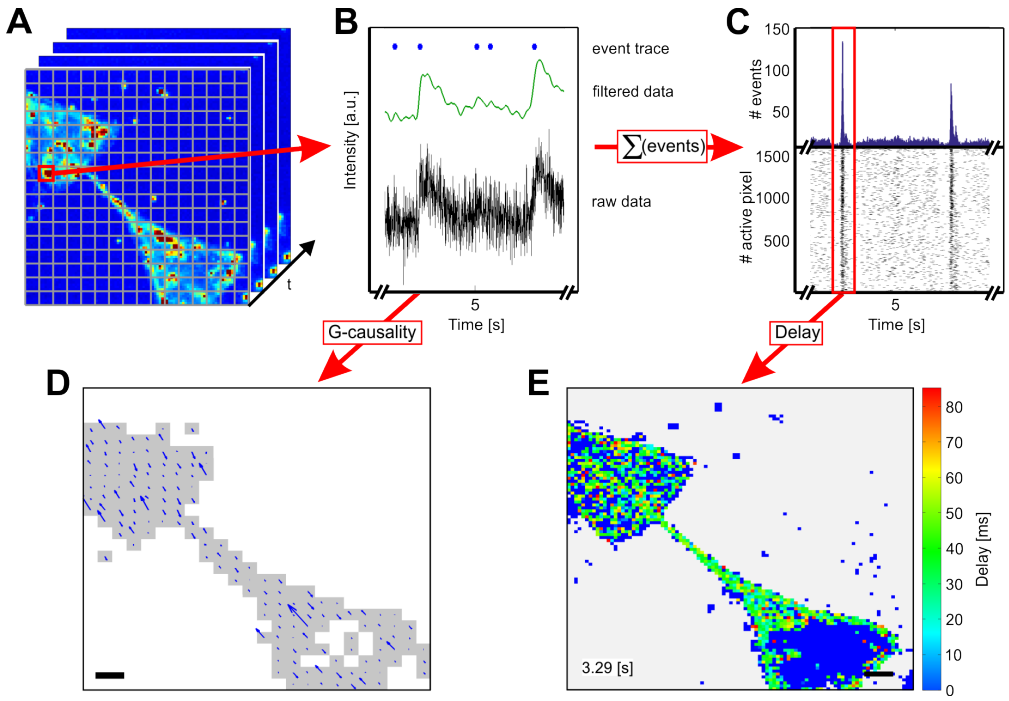

Figure 4.13: Work-flow of the MATLAB script used to analyze fluorescence sequences from calcium imaging. **A**) Additional binning is applied resulting in a resolution close to the dimensions of the cells. **B**) Raw data are extracted from sequences and filtered. Fluorescence intensity increases related to action potentials are detected by the first derivative of the filtered data and converted into an events trace. **C**) Summation of the events over time results in a histogram (upper half) facilitating the identification of substrate spanning excitation. Lower half depicts occurring activity for every pixel. **D**) Plotted direction of influence determined by Granger causality analysis. Scale bar: 50 μm, vector scale: 1.5. **E**) Color-coded delay plot of the substrate spanning excitation marked with the red box in **C**. The insert in the lower left corner indicates the point in time of the first single event in the substrate spanning excitation relative to the whole raw recording. Scale bar: 50 μm.

duced by neuronal activity are identified and according to their occurrence event traces are generated.

C)**Identification of substrate spanning excitation**: By summing up all event traces of all the active traces a histogram over time is generated that is used to identify substrate spanning excitation.

D)**Multivariate Granger causality analysis**: A multivariate Granger causality analysis is performed with smoothed intensity traces to estimate causality based connectivity between individual ROIs.

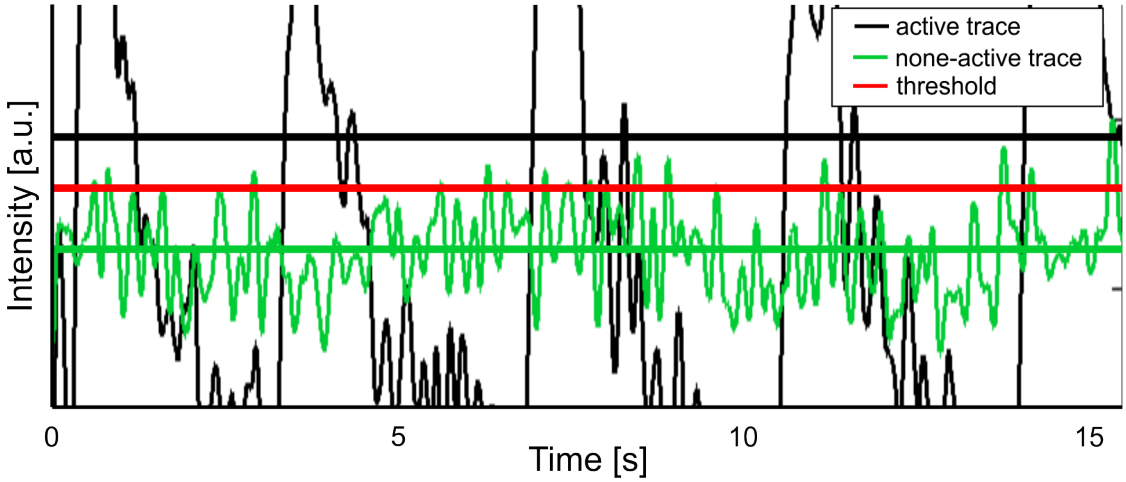

Figure 4.14: Thresholding to identify active traces. Two intensity traces, black and blue, are shown with their calculated $|\text{mean}_{\text{trace}} - \text{median}_{\text{trace}}|$. The red line indicates the threshold criteria $A * 0.95$. Large amplitude fluctuations in the black trace increase B_{black} and thus categorize the black trace as an active trace. The green trace is considered non-active, as its B does not exceed the threshold.

E)**Temporal delay**: Calculate the temporal correlation of individual time traces in substrate spanning excitation and generate color-coded temporal delay plots.

Data import and selection of active traces: The most challenging aspect of the analysis of calcium imaging sequences was the automated identification of ROIs from intensity sequences. At first the original files were converted to uncompressed AVI files which were subsequently read by a multiselection into the MATLAB script. As the sequences have an original resolution of 1.3 $\times$ 1.3 μm per pixel, which is by far beyond single cell resolution, an additional 5 $\times$ 5 binning is applied to avoid oversampling and achieve a resolution slightly higher than a single cell dimension (6.5 $\times$ 6.5 μm per pixel), see Figure 4.13 A. For every of these resulting pixels a combined intensity trace is generated by averaging all individual pixels. Resulting raw data intensity traces, see Figure 4.13 B, are further processed to separate traces that exhibit intensity changes corresponding to neuronal activity from those that do not. This is necessary, since the number of pixels (102 $\times$ 96 pixel) is still very high, so that the calculations would be time consuming and no additional information would be provided.
To differentiate between active and non-active traces, all time sequences are smoothed for thresholding with a Gaussian filter with the window size of 45 frames. This is feasible as the time of peaks is not of interest but their amplitude. To define a decision criteria the mean intensity and its standard deviation of the entire sequence is calculated: $A = |\text{mean}_{\text{frame}} + \text{std}_{\text{frame}}|$, see Figure 4.14 red line. Subsequently the absolute difference between mean and median in-

tensity for every pixel related intensity trace is calculated ($B = |\text{mean}_{\text{trace}} - \text{median}_{\text{trace}}|$). As large intensity variations induced by neuronal activity, have a stronger impact on the mean intensity than on the median the following should be true: $B_{\text{active}} > B_{\text{non-active}}$, see Figure 4.14. Thus A and B can be used as a criteria to identify active and non-active pixels. In the calculations performed for this thesis, traces were considered as active if $A * 0.95 < B$. In this way, active pixels are separated from background pixels without spontaneous neuronal activity. By varying the threshold value to a lower level more pixels are considered active including incorrect pixel for analysis. A further increase of the threshold does not decrease the number of active pixels as much as a lower threshold, see Figure A.5 in the Appendix. As a consequence $A * 0.95$ has been chosen as threshold criteria for all sequences.

Smooth and normalize time traces for event detection: After identifying non-active and active traces, all traces are smoothed and normalized for time correlation analysis. Normalization is performed by $\Delta F = (F - F_0)/(F_{\text{max}} - F_0)$, where F is the measured raw intensity and F_0 the minimal and F_{max} the maximal intensity in the sequence. At the same time, high temporal intensity fluctuations were reduced with a Savitzky and Golay filter [114] with a polynomial order of 3 and an appropriate window size. The selection of a well fitting window size is essential for the validity of later analysis. The fluctuations in the raw data in Figure 4.15 are clearly visible. The underlying characteristics of the raw data are best preserved by a Savitzky and Golay (SG) window of 25 frames, whereat the filter is applied from both sides of the trace. At the same time this trace still exhibits some fluctuations with a lower amplitude than the raw data, while the characteristics and especially the shape of the rising flank is well preserved. An increase to a window size of 60 frames strongly reduces the intensity fluctuations, while at the same time the shape of the rising flank of the signal changes, the slope decreases. This effect is caused by the larger window size as more values from the period of decreasing intensity are considered in the calculation of the filtered value. For a window size of 100 frames and above, the slope of the rising flank gets too flat and a meaningful characteristic at the rising flank is not maintained. As a consequence, a window size of 38 frames, see Figure 4.15, was selected for data processing in this thesis. This size was the best compromise between preserving the characteristics of the intensity trace while reducing the intensity fluctuations. With this window size the slope of the fluorescence is sufficiently conserved and the onset of the rising flank can be detected easily without any disturbance by large intensity fluctuations.

Non active traces were analyzed to estimate the background noise level. Therefore the first derivative of the intensity traces for non-active pixels was calculated and plotted in a histogram. Subsequently a normal distribution is fitted to the resulting histogram to receive the 1-σ environment of the distribution as an estimation of the background noise level. For

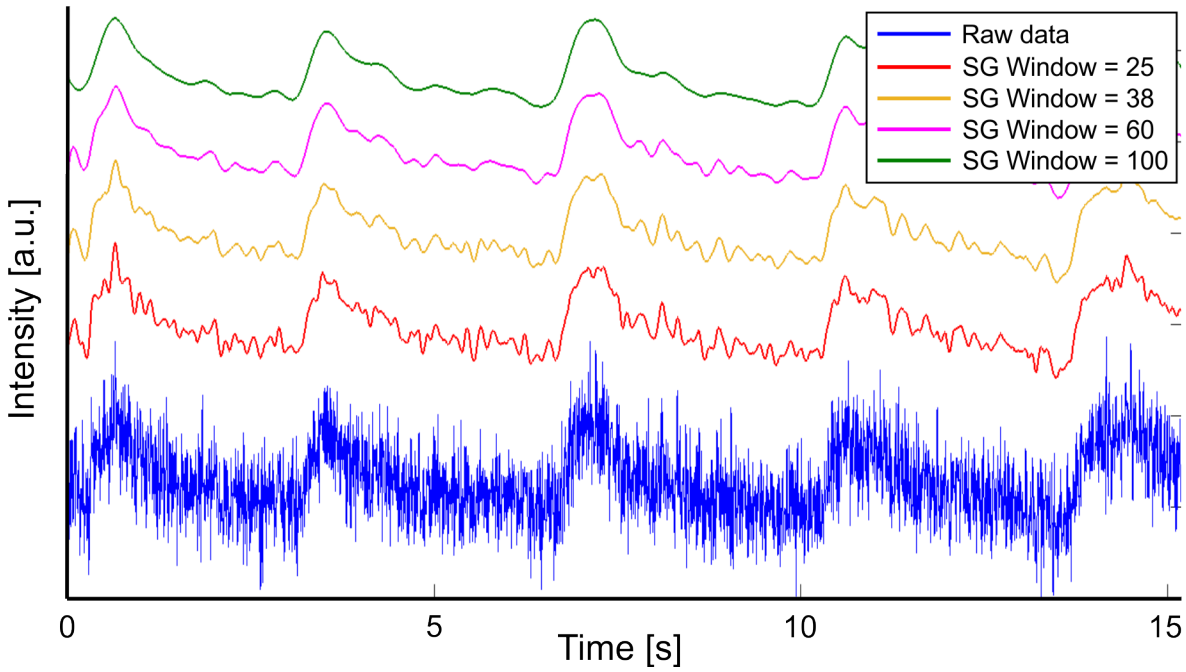

Figure 4.15: Savitzky-Golay filter comparison for different window width. A representative intensity trace (blue) is filtered with different widow sizes. Resulting traces are shown in different colors and shifted in intensity. The polynomial order for all filter was three.

peak detection in active traces, the first derivative of the intensity traces were calculated and smoothed with a Savitzky-Golay filter (polynomial order: 3; widow size: 11 frames). A potentially occurring linear trend resulting from bleaching in the first derivative of the time trace is removed prior to peak detection. Large peaks in the derivative of the time trace of active pixels represent fluorescent changes and those corresponding to neuronal activity have to be identified. Thus a minimal peak height of $3 * \sigma$ is required where σ is the previously calculated background noise level. Additionally, a minimal temporal separation of the peaks by 400 ms is required as this is conservatively assumed to be the maximal time an excitation needs to travel across the pattern observed in a sequence. As a consequencem every active trace can maximally contribute one event to a substrate spanning excitation (SSE), even though there might be a higher number of events occurring in a trace for a SSE. A smaller time window would lead to a higher number of false detected neuronal activity related events. This leads to some false event detection, see marked events in Figure 4.13 B that do not correlate to any noticeable neuronal activity. As these falsely detected events are caused by background signals their over all number for a specific point in time is low compared to the number of active traces and the selectivity does not need to be improved for the peak detection routine. On the basis of the detected peaks, binary event traces of the same length as the intensity traces were

generated for every pixel.

Identification of substrate spanning excitation: To identify SSE all event traces are summed over time and plotted in a histogram, see Figure 4.13 C. Additionally, events are marked for every active pixel that compose the histogram in the upper part of the image section. For a SSE a high number of events occurs in a small time window resulting in a high event count in the histogram. These peaks can be demarcated from surrounding background by the region properties function from MATLAB. The background is mainly composed of falsely detected activity. Here it becomes visible that the distribution of the falsely detected signals is quite homogeneous over time and seems to be caused by sensor based fluctuations in the intensity signal. A lager window in the Savitzky-Golay filter reduces the number of falsely detected signals but at the same time strongly influences the shape of the rising flank, as not all events exhibit the same amplitude and decay time. Thus the number of falsely detected events is tolerated as the original characteristic of the intensity trance is preserved as far as possible.

Multivariate Granger causality analysis: Smoothed intensity traces are used for multivariate Granger causality analysis. As the number of active traces is too high for a reasonable calculation of causal dependence, an additional binning is applied to the active traces. The size of the newly generated pixels is 26×26 μm, assuming a pixel size of 1.3 μm in the AVI file. For every newly generated active pixel the causal influence from and to every other active pixel is calculated, resulting in a $n \times n$ matrix $\mathcal{F}$ with causality coefficients representing the Granger-causality (G-causality) between all n newly generated active traces. The MATLAB toolbox used, provided by A. Seth [118], also determines the significance of these values. The significance level (p-value) can be chosen freely. For all analysis three different significance levels were chosen: 5%, 1%, and 0.1%, but the obtained results for all three levels are the same, resulting in a significance of $p < 0.001$. To visualize the G-causality, a vector is generated for every single active pixel, representing the orientation of the influence. Therefore the difference between the values $\mathcal{F}(X,Y) \equiv \mathcal{F}_{\mathbf{X}\to\mathbf{Y}}$ and $\mathcal{F}(Y,X) \equiv \mathcal{F}_{\mathbf{Y}\to\mathbf{X}}$ is calculated to determine whether X influences Y or the other way around. If $\mathcal{F}(X,Y) > \mathcal{F}(Y,X)$ than the intensity trace of pixel X influences the trace of pixel Y. The length of axons and dendrites is limited and thus the influence on an individual pixel needs to be reduced, as all active pixels are included in the calculation of the G-causality. Therefore a radial dependence is defined and causality visualizations are generated for r = 100 μm to r = 400 μm in 100 μm steps. Figure 4.16 shows how the influence of a pixel on another pixel is calculated. A circle with the radius r is drawn around a pixel of interest and all active pixels (gray) inside the circle are considered in the calculation. The causality matrix tells whether the orientation of the influence is $\mathcal{F}_{\mathbf{Y}\to\mathbf{X}}$ or $\mathcal{F}_{\mathbf{X}\to\mathbf{Y}}$. All x- and y-components of the active pixels are combined and a resulting orientation

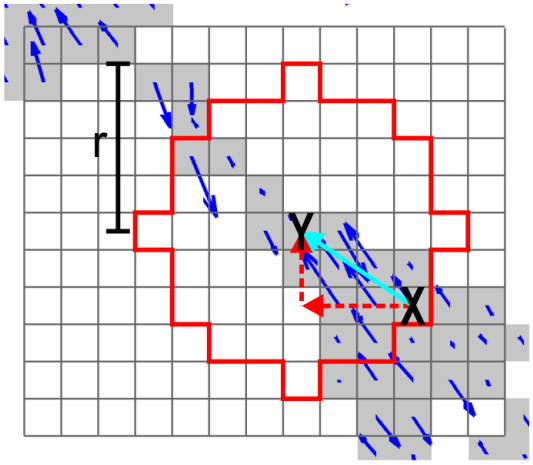

Figure 4.16: Granger-causality calculation with distance dependence. A circle with radius r (red) is placed around a pixel of interest and the influence of all active (gray) pixels within the circle is divided into an x- and a y-component. The combination of the individual x- and y-components (red arrows) and their strength of causality results in the blue arrows, depicting the orientation of G-causality for every pixel.

is achieved that is visualized by the blue arrows in Figure 4.16. The length of these vectors indicates the degree of causal dependence.

Temporal delay: In addition to multivariate Granger causality analysis, the temporal delay between individual time traces in a substrate spanning excitation is calculated. As depicted in Figure 4.13, the event traces are used to identify the first single event (SE) in a SSE and calculate the temporal delay between this SE and every subsequent SE. According to this information, color-coded temporal delay plots of the frame are generated, where the time of the first SE is annotated in the lower left corner and a scale bar of 50 μm is inserted at the lower right corner. Subsequently, the color-coded delay plots are analyzed manually with respect to the direction of the propagating signal during a SSE. SSEs are categorized in three classes: lower $\rightarrow$ upper; upper $\rightarrow$ lower; both, as were already introduced for neuronal growth in immunohistochemical analysis. Hence, multiple orientations can occur for a single recording resulting in a standard deviation of the final result. Besides the pure delay between pixels on the substrate, it is also interesting to know if there are any predominant signaling pathways on the pattern. To identify these pathways the activity information of every pixel within a SSE is processed. Every active pixel in a SSE is identified with one and non-active pixels with zero. Subsequently it is summed over every pixel and divided by the number of SSEs. The resulting plot for a sequence represents the recurrence of individual pixels in the different SSEs. Additionally the delay information of every single SSE is merged into one conclusive plot presenting the average delay. Therefore the delay for a single SSE is normalized prior to

averaging, as this reduces the over representation of large delays in the resulting plot. These averaged delay plots reveal the orientation of recurrent signaling pathways on the pattern.

4.3.2 Analysis of Granger conditional causality

Granger conditional causality analysis (GCCA) is a well established method to investigate causalities between different parts of a neuronal network. It applies to investigation of fMRI data [132] and other brain network analysis [133] but also to *in vitro* cultures on microelectrode array (MEA) [134]. Thus it is just more than consequential to apply GCCA on time traces from fluorescence imaging, such as calcium imaging. Here the great challenge is to chose appropriate regions of interest in the automated sequence analysis. This is done as described above with the downside that not every pixel is necessarily associated with a nucleus. The low impact in causality analysis caused by these pixels is considered in the GCCA. Another aspect that has to be considered in the analysis is the different length of axons and dendrites. In microfluidic devices it was shown that axons reach a length of more than 500 μm without effort while the radius of the dendritic tree is limited to roughly 300 μm [19]. As a consequence, an appropriate radius for GCCA needs to be determined. Figure 4.17 shows an excellent example how the causal influence differs with radial dependence. This becomes obvious in particular at the junction between the adjacent populations in the Figure 4.17. In **A** the causal influence at the gateway is oriented to the lower structure for r = 100 μm. The impact of surrounding

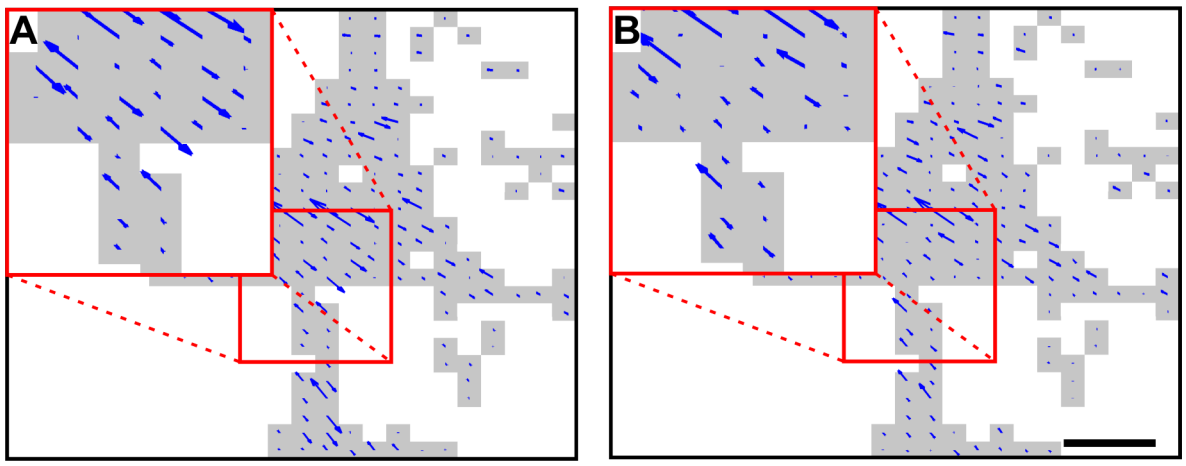

Figure 4.17: Different influence radius for Granger conditional causality analysis (GCCA). This figure shows the resulting causality plot for different influence radii of GCCA. **A**) The GCCA behavior at the junction is illustrated in the insert, r = 100 μm. **B**) The orientation of the GCCA behavior changes with increasing radius, r = 300 μm. The conclusive radius needs to be chosen according to potential axonal and dendritic length. Scale bar: 100 μm.

Table 4.2: Orientation of Granger conditional causality analysis on different structures with differing influence radius r.

Structure	Orientation	r = 100 μm [%]	n	r = 200 μm [%]	n	r = 300 μm [%]	n	r = 400 μm [%]	n
SC1	lower → upper	15.8	19	15.0	20	13.6	22	18.2	22
	upper → lower	42.1		35.0		36.4		45.5	
	both	42.1		50.0		50.0		36.4	
SC2	lower → upper	25.0	4	50.0	4	20.0	5	20.0	5
	upper → lower	0.0		0.0		20.0		20.0	
	both	75.0		50.0		60.0		60.0	
CT1	lower → upper	51.2	84	56.0	91	82.7	98	76.0	96
	upper → lower	15.5		19.8		6.1		10.4	
	both	33.3		24.2		11.2		13.5	
CT2	lower → upper	69.1	55	62.9	62	84.8	66	77.3	66
	upper → lower	5.5		12.9		7.6		9.1	
	both	25.5		24.2		7.6		13.6	

pixels drastically changes for r = 300 μm, as can be seen in the insert in Figure 4.17 **B**. Nearly all arrows at the junction exhibit a high fraction of influence from the lower structure. The resulting plots from Granger conditional causality analysis were manually categorized in the three classes lower → upper, upper → lower, and both. Obtained values are listed in Table 4.2. Obviously the causal influence differs depending on the radius. For r = 100 μm a slight preference from lower → upper can be recognized for CT structures with values slightly above 50%. The SC structures do not exhibit any preferred direction and show high values for the category both. This does not change if the radius is increased to r = 200 μm. A completely different situation can be seen for r = 300 μm. Here a significantly predominant orientation of the direction of causal influence can be recognized from lower → upper ($p < 0.001$), where more than 80% of both CT structures in the recorded sequences manifest a causal influence from lower → upper, see Figure 4.18. For both SC structures there is still not any preference visible other than the orientation in both directions. With a further increase of the radius the impact on the CT structures decreases while the characteristics for the SC do not change significantly. Potential reasons for this behavior will be discussed below, in an attempt to unravel the underlying mechanisms.

As already mentioned axons and dendrites show a different length and thus are impacted differently by changes in analysis radii. For r lower than the radius of the dendritic tree the ratio of dendritic impact outweighs the axonal influence from surrounding pixels. Certainly there is a causal connection caused by axons in the small circle but it will colloquial be dominated by

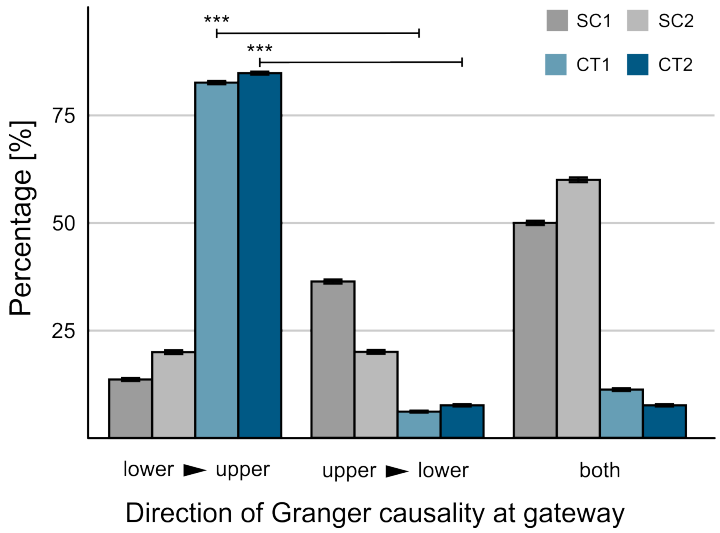

Figure 4.18: Direction of conditional Granger-causality at the gateway for r = 300 μm. A predominant orientation of causal influence for CT structures from the lower to upper structure with more than 80% is established. This orientation is significantly higher than upper $\rightarrow$ lower, ***: $p < 0.001$. At the same time no preferred orientation is exhibited for the SC structures.

dendritic connections. As the dendritic growth is not influenced as much as the axonal growth by the geometry of the funnel, no preferred orientation for conditional Granger causality is established. With increasing distance, more pixels are included that are potentially connected to the pixel of interest, including those with longer connections that are increasingly likely axonal. As the immunofluorescence experiments revealed, neither axons nor dendrites grow in straight lines but furthermore perform turns and exhibit meandering growth. Consequently, an actual axonal path is longer than the radius in the investigation. Following this argument it is clear that the percentage drops for r = 400 μm, as the number of additional axons influencing the pixel of interest drops. As a consequence pixels are included in the calculation that do not exhibit any influence in reality but are falsely considered in the calculation. Additionally, it has to be considered that at some point the radius of influence exceeds the dimensions of the recorded frame. It is obvious that the cells on the recorded pattern receive input from cells further away in the daisy chain that can not be included in the calculation. Despite this, the region of interest is the junction between the observed populations and the image section is chosen such that this junction is almost in the center of the image. Thus a huge impact from missing pixels that were not included as they lie outside the image, can be excluded.
The obtained plots illustrating the GCCA disclose another interesting aspect. Numerous plots show arrows with a high fraction of vectors pointing from the edge of the structure towards its center. Additionally snap-shots from the calcium imaging sequences reveal regions with

high activity. These regions can be recognized in the orientation of the arrows in the image resulting from GCCA. As a consequence, proposed signaling pathways on the pattern can be ventured. Analyzing the resulting plots lead to the assumption that signals follow the bundles of axons described previously at the edges of the pattern. A very important property of the Granger conditional causality analysis is that no above threshold signals are required to calculate causalities. Even sub-threshold changes in fluorescence intensity are sufficient for the evaluation. This offers the opportunity to access information from those traces where a high background signal is present and no delay plots can be generated. Even though these results have to be handled with caution as they might be influenced by artifacts from the imaging procedure.

4.3.3 Analysis of delayed neuronal activity

Other than for conditional Granger causality analysis, intensity traces with distinct intensity increase are required for the analysis of delayed neuronal activity. The MATLAB script is able to identify signals with a signal to noise ratio of at least 2.7 in the normalized intensity traces. Combining this sensitivity with the spatial resolution facilitates the detection of signals in axonal bundles and even in smaller neurites, which becomes obvious when comparing Figure 4.19 A and B. In the snap-shot of the calcium imaging sequence, the fluorescence intensity values are illustrated in a jet colormap, such that high intensity values are shown in red and low ones in blue. Some red spots are visible and indicate positions where single or clusters of somas are located. All of these spots can be found in the delay plot as the soma is the place of highest calcium concentration change and thus exhibits large intensity changes. Furthermore it is noteworthy, that the signals in either structure follows the edge of the pattern and just partly spreads in its center. This can be attributed to the axonal bundles that were described in Chapter 4.2.2. Interestingly the ramified network of neurites in the center of the structures does not show strong activity, except for the two visible sprays. Thus, signaling pathways can be identified by the delay plots, even though a single excitation does not reveal much about recurrent signal cascades within a pattern. The identification of signaling pathways will be discussed at the end of this section.

Figure 4.19 shows an example of a delay plot generated for a single SSE. A snap-shot of the sequence is presented in A, while the delayed neuronal activity for a SSE starting after 10.27 s of the sequence is depicted in B. The activity starts in the lower structure and spreads towards the upper one. The orientation of the propagating signal for all substrate spanning excitations is manually analysed for all sequences and categorized in the aforementioned three classes. Results from all obtained delay plots can be seen in Figure 4.20 that shows the percentage

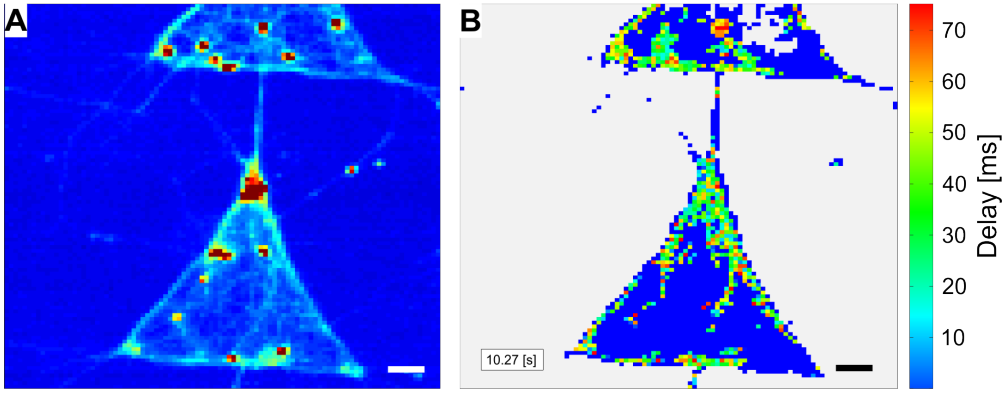

Figure 4.19: Analysis of signal propagation on a CT2 structure. **A**) Image of the first frame of the sequence that visualizes spots of high fluorescence intensity in red for an overview of nuclei. Scale bar: 50 μm. **B**) Color-coded delay plot of a SSE. The signal starts in the lower structure and propagates towards the upper one. The time of the first SE is annotated in the lower left corner. Scale bar: 50 μm.

of signals propagating apportioned in every category and pattern design. Included error bars indicate the standard deviation. Eye-catching is the significant percentage of signals propagating from lower $\rightarrow$ upper for both CT structures. 85 $\pm$ 2.9% of CT1 ($p < 0.001$) and 79.2 $\pm$ 2.3% of CT2 ($p < 0.001$) signals are guided by the funnel towards the adjacent structure and more importantly, the signals induce an excitation in the next structure. Conversely, this means that just a very low fraction of the signals spreads from the upper towards the lower structure or in both directions for a single sequence. Considering the SC structures, the situation changes drastically. For neither SC1 nor SC2 is a preferred direction of signal propagation determinable. Both orientations lower $\rightarrow$ upper and upper $\rightarrow$ lower exhibit almost the same fraction of signals spreading in one of these categories. Thus it is not surprising that the amount of excitation spreading in both orientations within one sequence is the predominant category for these structures. Summarizing these results one can say that the design of the gateway is decisive for directed signal propagation.

Another aspect in signal propagation, which is accessible by the plots of delayed neuronal activity, is the signal velocity. To extract this with high precision, the signalling pathway, as well as the exact time the signal needed to traverse the distance, is required. Consulting the plots of delayed activity to extract the propagation velocity exhibits the downside that neither the exact path nor the required time can be extracted with high precision. Analyzing all resulting plots of delayed neuronal activity for all structures, the propagation velocity can be approximated to 13 $\pm$ 3 mm/s. This result is an order of magnitude below the reported literature values from *in vivo* studies [135] and cerebral slices [136, 137]. To explain this difference the different ex-

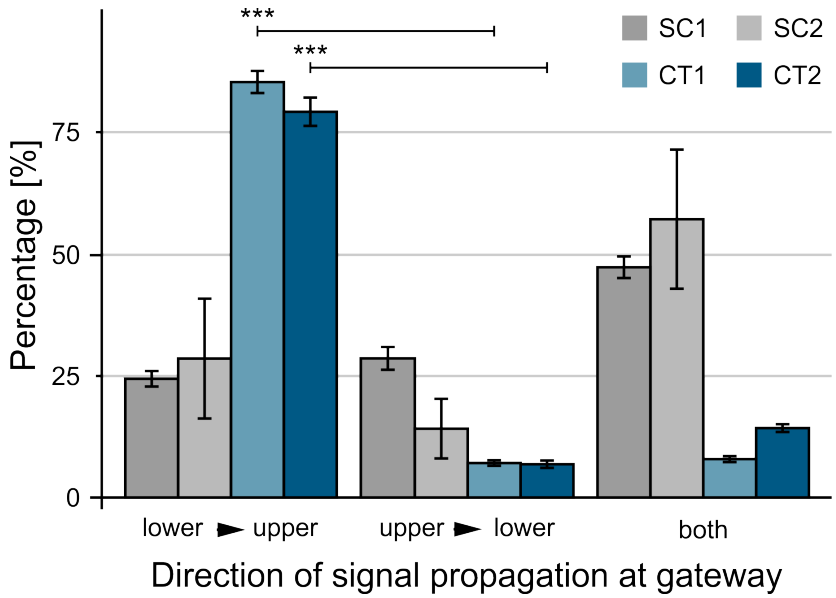

Figure 4.20: Quantification of directed signal propagation among patterned populations of neurons. Color-coded delay plots were analyzed with respect to the direction of signal propagation at the gateway. For both SC structures no preferred direction could be noticed. Whereas for both CT structures a significant bias from the lower to the upper structure of more than 80% is visible, ***: $p < 0.001$. All values with standard deviation.

perimental conditions need to be considered. The highest impact on signal velocity within the neuron comes from the myelination of the axons, as described in Chapter 2.1.2. Neurons in *in vivo* and in slices exhibit a coverage with myelin, whereas the *in vitro* cultures used for this thesis are not insulated. As a consequence, the propagation velocity is expected to be lower for the *in vitro* cultures used than for experiments in slices and *in vivo*. In addition the experiments performed in this thesis were conducted in normal atmosphere with 0.04% CO_2 and 21% O_2 at 24°C room temperature, while the other experiments were performed at 32-36°C and 95% O_2 and 5% CO_2. Just concentrating on the temperature difference of roughly 10°C between the experiments a decrease in nerve conduction velocity can be argued by simply applying the Arrhenius equation for reaction kinetics [138]. Arrhenius stated that the rate constant k of a reaction depends on activation energy E_a, the absolute Temperature and the universal gas constant R: $k \approx e^{-E_a/(RT)}$. Following this formalism the Q_{10} temperature coefficient can be calculated as:

$$Q_{10} = \left(\frac{k_2}{k_1}\right)^{10/(T_2-T_1)},$$

where $k_{1,2}$ are the reaction rate at the temperature T_1 and T_2. Using this formalism, a reduction of the nerve conduction velocity by a factor of 2-4 can be calculated for a temperature differ-

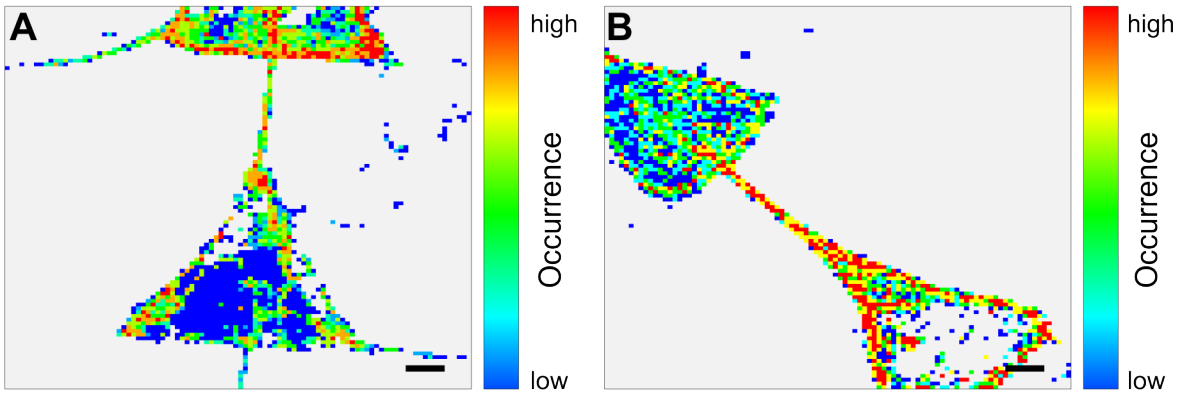

Figure 4.21: Averaged sum of activity for pathway analysis. Both plots **A**) and **B**) reveal collimating signal propagation along the edges of the pattern for a CT1 structure after 24 DIV. Scale bar: 50 μm.

ence of 10° [139]. Beside temperature effects on the propagation velocity within and among the populations, connections between neurons and thus synaptic delay has to be considered in the calculations. It is well known from literature [9] and double-patch clamp experiments performed in my diploma thesis [53], that the synaptic delay between adjacent neurons can range from 1-5 ms. Whereas these values are from experiments performed at 36°C and therefore the applicable values are presumably slower than those reported, as the synaptic communication is a diffusion driven process. Here, the distance dependence can be written as $dx^2 = Ddt$ and this leads to $dt \propto 1/D$, with the diffusion constant D. This constant itself is directly proportional to the temperature ($T \propto D$) and it can be written: $dt \propto 1/T$. With this we have a difference in propagation speed of neurotransmitter within the synapse of:

$$\Delta t = \frac{T_1}{T_2} = \frac{297K}{309K} \approx 4\%$$

Additionally the number of synapses involved in the signalling pathway is unknown and thus the resulting total synaptic delay in the path can only be approximated. As a conclusion the determined signal propagation velocity for a neuronal signal dispersing on the patterned neuronal network can be considered reasonable, even though the impact of different gas concentrations remains disregarded in the considerations.

Nonetheless, signaling pathways are still not easy to determine from plots of delayed neuronal activity. Therefore the averaged sum of active pixels in all SSEs of a sequence is calculated, resulting in plots like those in Figure 4.21. These pathway analysis plots reveal that signals an all four designs follow the bundles of axons that collimate along the edges of the protein structure, as described in Chapter 4.2.2. Interestingly, the specified axonal growth behavior at

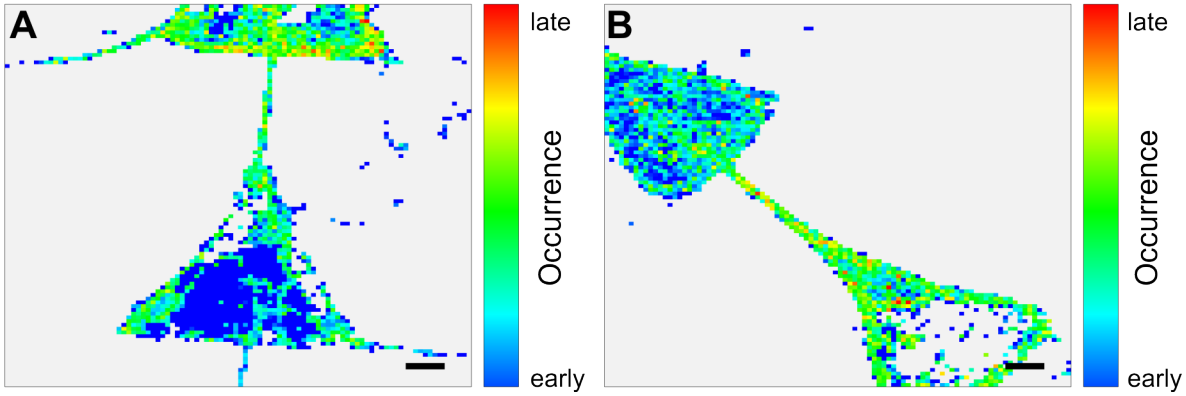

Figure 4.22: Averaged delayed activity for pathway analysis. Either plots **A**) and **B**) reveal collimating signal propagation along the edges of the pattern for a CT1 structure after 24 DIV, starting at the lower structure and spreading into the upper one. Scale bar: 50 μm.

the junction can be found in these pathway analysis plots. Axon bundles sprout from the lower into the upper structure, where they rove into a fan-like structure. Beside the axon bundles, also cell bodies can be identified as neuronal activity accumulates at these spots, even though they are not as prominent as the bundles, as they are not necessarily involved in every substrate spanning excitation. Surprisingly, the inner part of the pattern is not as involved in signaling cascades as the edges of the pattern, even if there are cell bodies and neurites located. This suggests that almost all neurons are represented by an axon in the bundles, so the bundles light up during every SSE even if not all neurons represented in the bundle are included in every excitation.

These discovered signaling pathways can also be recognized in the averaged normalized delayed activity as depicted in Figure 4.22. Here the pathways are not as pronounced as at the averaged activity plots, but they still can be distinguished. In addition these plots reveal the underlying order of the excited pixels. Figure 4.22 A impressively shows the start of the excitation in the lower structure, spreading into the upper structure, visualized by the different color-coding. For Figure 4.22 B this is not as distinct as for A, but still a tendency for later occurrence of activity in the upper structure can be noticed. The summary of the mean delayed activity on the substrates results in the similar results as were found for GCCA and the analysis of the delayed excitation of singles SSEs.

4.4 Impact of structure design on network polarity

Chapter 4.1 to 4.3 revealed different aspects of neuronal cultures growing on substrate bound protein patterns. In this section these findings will be combined and concluding implications will be drawn. For an overview the obtained and already presented results are summarized in Table 4.3. Obviously various apex angle and shape of the funnel exhibit different impacts on neurite growth and the resulting guided functionality. These mediated effects are independent of culture age, as the presented experiments were performed between 14 and 24 DIV without noticeable changes. Even though recordings after 14 DIV exhibit spontaneous activity an increase in neuronal activity can be seen for experiments conducted later than 21 DIV, indicating an advanced network maturation that is represented by a higher firing rate and shorter interval between two SSEs. Also the signal propagation velocity is not affected by the degree of maturation or the different funnel designs. Although most of the parameter of neuronal signaling are not changing with gateway layout, the resulting direction of signal propagation does, which is the most important impact for this study.
Here, it is crucial to take a closer look at the orientation of axons and dendrites at the gateway and the resulting direction of signal propagation. For instance the huge variance between axonal and dendritic growth from lower $\rightarrow$ upper on CT1 and CT2 structures, compare Table 4.3, results in a clear dominance of signals propagating in this direction. Whereas less than 10% of the signals on both CT structures spread in the opposite orientation. Only a small single-digit percentage of axons yet more than 33% of the dendrites sprout from upper $\rightarrow$ lower resulting in the signal propagation behavior. The SC structures manifest a completely different characteristic. Here, neither for SC1 nor for SC2 a distinct orientation of axonal or dendritic growth is found. Albeit the amount of neurites growing from lower $\rightarrow$ upper is, with roughly 50%, larger than those in the other orientations, but as there is no predominant orientation for axons or dendrites, no dominating orientation of propagating signals manifests. For both distinct orientations, the amount of signals oriented alongside these directions is about 25%, whereas the number of sequences that exhibit excitation spreading in both ways is at about 50%.
As a consequence of these results some design rules are expressed: First of all vital and healthy populations are required to record any type of reliable activity on the pattern. Thus an aspect ratio of height/width by 1 to 1.2 is proposed as this guarantees a population with a reasonable amount of neurons. If the number of cells per population is decreased to far weak to no spontaneous activity will occur within the population. For example SC2 structures at least 10 neurons per structure are required to generate recurrent excitation that includes all cells on the pattern. Here, the critical cell density for cell seeding is about 15,000 cells per cm^2 to create

Table 4.3: Orientation of neurite growth, signal propagation, and Granger causality (G-caus.) on differently shaped substrate bound protein pattern investigated by the different methods described in Chapter 4.1 to 4.3.

		Neurite growth						Signal Propagation			G-causality		
Structure	Orientation	% of Axons	STD	n	% of Dendrites	STD	n	% of Signal	STD	n	% for r=300 μm	STD	n
SC1	lower → upper	56.1	4.1	41	53.6	3.2	114	24.1	1.8	91	13.6	0.4	22
	upper → lower	24.8	6.1		24.8	6.5		28.6	2.5		36.4	0.5	
	both	19.5	5.1		21.6	4.7		47.3	2.4		50.0	0.5	
SC2	lower → upper	47.4	13.7	38	57.6	6.4	85	28.6	12.4	7	20.0	0.5	5
	upper → lower	18.4	17.7		17.7	2.8		14.3	6.2		20.0	0.5	
	both	34.2	16.4		24.7	2.2		57.1	14.3		60.0	0.6	
CT1	lower → upper	93.7	8.9	48	54.2	3.0	107	85.0	2.9	124	82.7	0.4	98
	upper → lower	2.1	0.0		33.6	3.1		7.1	0.6		6.1	0.3	
	both	4.2	0.0		12.2	3.4		7.9	0.9		11.2	0.3	
CT2	lower → upper	86.8	11.5	38	38.6	12.5	44	79.2	2.3	123	84.8	0.5	66
	upper → lower	5.3	0.0		40.9	9.8		6.8	0.5		7.6	0.3	
	both	7.9	0.0		20.5	8.3		14.0	0.7		7.6	0.4	

networks with substrate spanning excitations and vital network growth within the pattern. The cell concentration on the pattern will increase by cell migration on the substrate. Besides the pattern dimensions and the cell density the funnel design turns out to be a very crucial factor in differentiated neurite guidance. Therefore an apex angle lower than 6° is suggested to form a needle like tip. As a consequence the aspect ratio can not be maintained and thus a curvature has to be introduced into the flanks of the structure, like those of the CT structures, to reestablish this ratio.

4.5 Neuronal circulating action potential

The experiments performed for this thesis so far, reveal a high impact on the orientation of signal propagation among adjacent populations of neurons by the geometries of their shape. To advance this knowledge and create a new tool for the investigation of recurrent signaling pathways and other aspects of signal processing within neuronal networks a system with potentially circulating neuronal action potentials (neuroCAPs) was developed. A layout of the design is shown in Figure 3.3 in Chapter 3.1.2. In general these structures consist of oppositely oriented daisy-chains of CT1 structures that are connected by two arcs. As the signal propagation on the daisy-chains of CT1 pattern is well characterized, the main focus of this chapter lies on the uncharacterized arc. So far it remains unclear if a signal that enters this part of the structure spreads and exhibits an excitation along the entire structure. Furthermore, it is not clear if the arc manifests the same directing properties in signal propagation like the daisy-chained CT1 pattern. However, these daisy-chains in the neuroCAP structures can be used to investigate recurrent signal propagation and to determine if there is a self triggering excitation going around the system.
In the first part of this chapter the neuronal cell growth on the arc is investigated in phase contrast images to reveal any obvious changes from growth behavior in comparisonm to CT1 structures. Subsequently, necessary modifications of the MATLAB analysis script are described, that had to be performed to fit the new design and requirements of the analysis. In the last part of this chapter the obtained results regarding orientation influence of Granger causality and delayed neuronal activity either in arcs and daisy-chains is described and discussed.

4.5.1 Cell growth on neuroCAPs

Neuronal development on neuroCAP structures is expected to be comparable to CT structures and differences are just likely to occur at the arcs that connect the two daisy-chains of CT1 structures. Within these arcs a ramified network is formed interconnecting the cells on the arc, see Figure 4.23 and Figure A.6 in the Appendix. Neurons growing on the pattern appear as single cells, but they also clustered in small groups, what is also observed for homogeneous cell growth *in vitro*. The very bright spots on the image are spheres formed by clusters of dead and alive cells. In fluorescence imaging analysis of cell activity for theses spheres barely exhibits fluorescence intensity changes. The amount of theses spheres depends on the quality of the mechanical dissociation of the cells during cell preparation. After 7 days *in vitro* the previously reported bundle formation at the edges of the protein structure is visible. Most

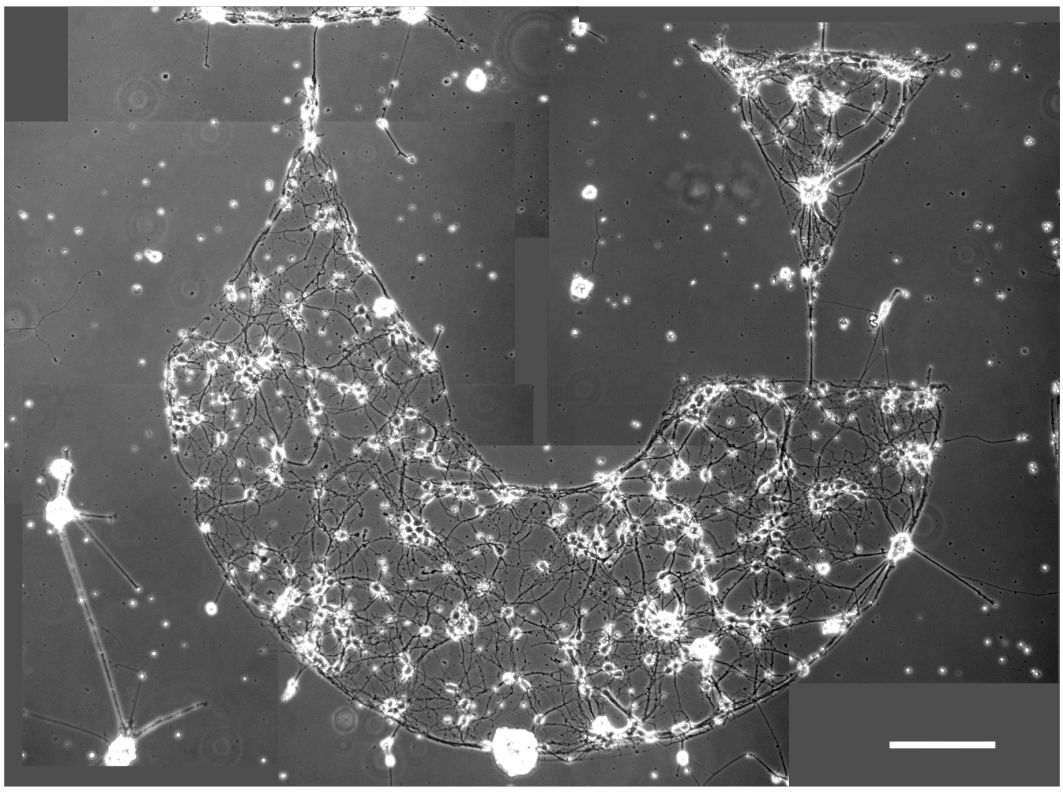

Figure 4.23: Stitched phase contrast image of cell grwoth on an arc of a neuroCAP structure after 7 days *in vitro*. Scale bar: 200 μm.

important in this observation is, that the bundles behave as it was seen for both CT structures[3]. At the flat end of the structure the bundle approaches the junction with the adjacent tip of the CT1 structure and crosses this point without any tendency of turning towards the funnel of the CT1 structure. At the same time bundles growing along the funnel of the CT1 pattern are guided to the flat end of the arc and enter it, where the bundle roves. On the other end of the arc, where it has the same shape as a CT1 structure, the axon bundles are channeled by the funnel into the adjacent CT1 structure. Whereas, cell growth at the gateway between these two structures behaves as previously described in Chapter 4.2.2. The neuronal outgrowth within the daisy-chained CT1 structures in the neuroCAPs does not differ from the growth on pure CT1 daisy-chains. As a consequence it can be expected that the orientation of signal propagation within these daisy-chains is the same or is at least similar to the one described in Chapter 4.4. Concluding that any potential of differing behavior is caused by the arcs and thus the signal propagation within them needs do be investigated in detail. Furthermore, the study of propagating signals on the daisy-chains can reveal interesting aspects of signal

[3]For comparison see Chapter 4.2.2

propagation such as periodicity of recurrent action potentials and the impact of structure size on the periodicity.

4.5.2 Modification of the analysis script

For calcium imaging experiments performed on neuroCAP structures some general changes in the recordings have been performed. As the dimensions of the structures are larger than those of single CT1 structures, the recorded frame size needs to be increased. Therefore the entire sensor (2160 $\times$ 2480 pixels) was used for sequence acquisition. This resolution would lead to sequenze size that could not be handled by the analysis script. Consequently, a 4 $\times$ 4 binning with a resulting resolution of 2.6 μm $\times$ 2.6 μm per pixel was applied during sequence recording and the exposure time was set to 7.5 ms. With these setting fluorescence time traces of 45 seconds could be recorded without exceeding a manageable file size of 5 GB for the exported AVI file.
In addition to the experimental settings some adaptations in the analysis script had to be done. Firstly, the intensity extraction from the frame differs for varying regions on the pattern. For recordings from an arc the entire frame has to be considered for image analysis, see Figure 4.24 A. Whereas, frames recorded from the daisy-chain part are divided into three parts: left (L), center (C), and right (R), see Figure 4.24 B. This individual treatment is necessary since the population on the arc pattern is connected and thus exhibits a causal dependence. Whereupon only adjacent populations on the daisy-chains can manifest a connectivity and opposing

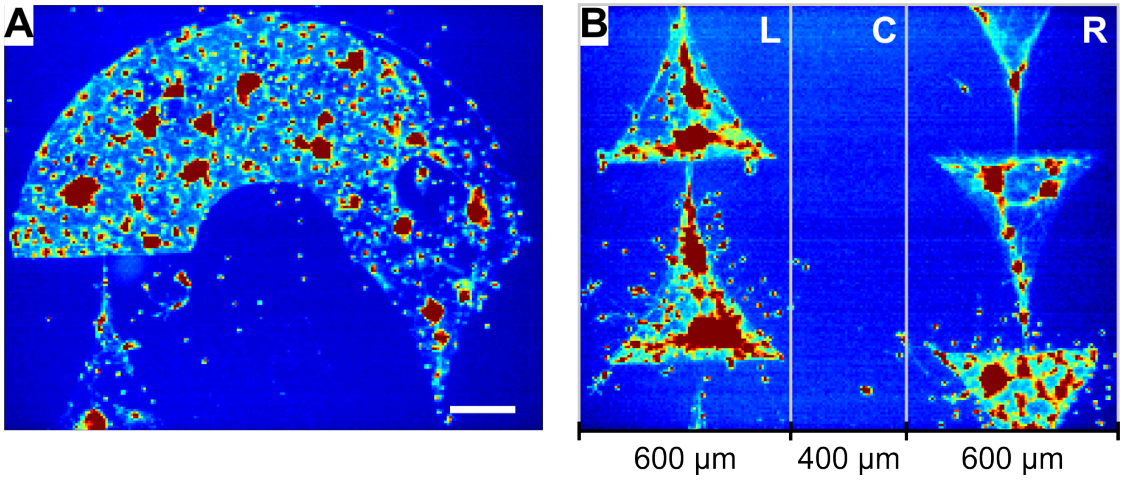

Figure 4.24: Two possible kinds of arrangement for Ca-imaging on neuroCAPs. **A**) For an arc of a neuroCAP the entire frame is considered for fluorescence analysis. **B**) For the analysis of the daisy-chain area of the neuroCAPs frames are cut into three parts: L, C, and R. Intensity analysis is only performed on L and R. Scale bar: 200 μm.

structures in L and R do not show any direct connectivity. Sequences recorded on both arcs and daisy-chains are analyzed using the extraction of active pixels and the resulting fluorescence time trace analysis described in Chapter 4.3.1, is applied. For an arc the script remains mainly unchanged, only the chosen binning results in a pixel size of: 13 μm $\times$ 13 μm. In contrast the different areas L and R on a daisy-chain frame are analyzed separately to find excitation that includes the entire left or right side. At the end the information about delayed neuronal activity within the populations on either side is compared to find temporal correlations between both sides. These correlations reveal information about recurrent signals propagating around the neuroCAP structure such as signal propagation velocity, time interval between excitations, and a dependence of the interval time and the size of the neuroCAP structure.

4.5.3 Signals on the arc of neuroCAP structure

Granger causality on the arc of neuroCAP structures

Calcium imaging sequences of arcs in the neuroCAP system, see snap-shot in Figure 4.25 A, were investigated to identify a predominant orientation of Granger causality on the pattern. Figure 4.25 B reveals that the G-causality can occur in an undirected state within a network, what means that there is not necessaryly a predominant direction of propagating signals within the pattern. The size of the network appears to be large enough to exhibit spontaneous activity, that is triggered by a pacemaker located within the pattern. The position of this potential

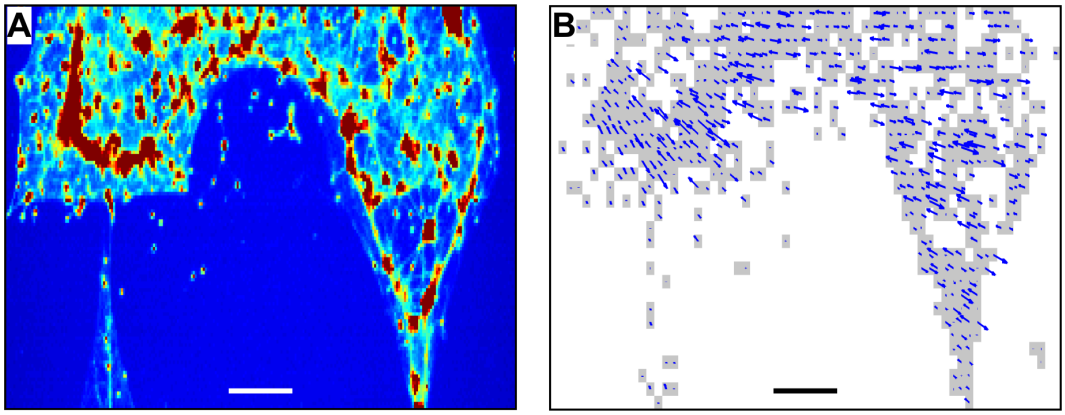

Figure 4.25: Granger conditional causality analysis (GCCA) of an arc of a neuroCAP structure. **A**) Snap-shot from calcium imaging sequence for visualization of the structure. **B**) Exemplary plot of GCCA. The orientation of the causality can be determined at the junctions of the arc. Within the network it is difficult to distinguish an orientation of the causality as a complex connectivity pattern is exhibited within the population. Scale bar: 200 μm.

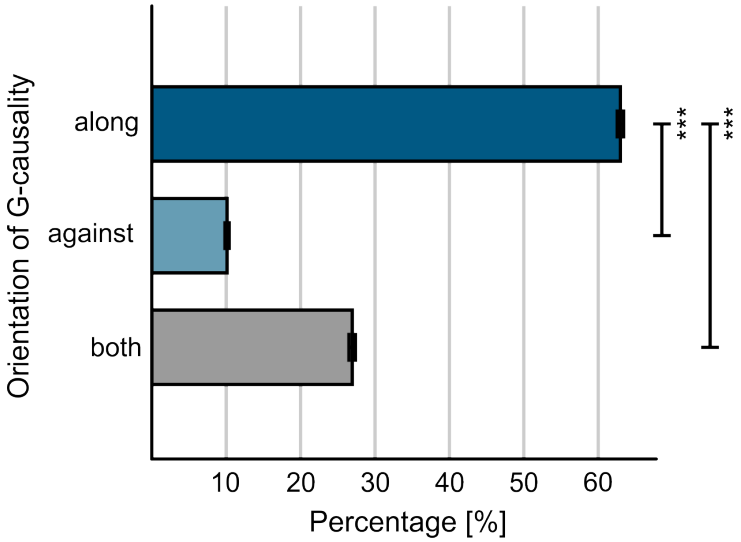

Figure 4.26: GCCA analysis of the arc in neuroCAP pattern. In a significantly larger amount of the recorded sequences the Granger causality is directed along the orientation of the arc (63%) in comparison to the other two orientations. ***: $p < 0.001$.

pacemaker determines the orientation of signal propagation within the arc and adjacent population. The rounded shape of the pattern itself could also influence the orientation of signal propagation on the structure, as an incoming signal needs to excite the entire network. As a consequence, the orientation of the G-causality at the gateway to adjacent structures on either sides of the arc was used to determine the orientation of the G-causality for the arc. This is assumed to be suitable as the connectivity within the network does not necessary determine the over all orientation of the signal within the population. As long as the signals come in on the one and leave the structure on the other side, the pathway within the pattern does not affect the in- and output of a network. To categorize the orientation of G-causality on the arc, it was assigned to one of the three classes: along, against, and both. Here, along means an orientation that corresponds to lower $\rightarrow$ upper in the daisy-chains of CT1 structures and Against represents the opposite orientation. Sequences that exhibit orientations of G- causality in both direction on either one or both sides or oppositely oriented G-causality on both sides are assigned to the category both.

The investigation of the orientation of the Granger causality at the junctions on both side of the arc revealed, that 63% of the signals propagate along the arc. This predominant orientation significantly exceeds the other two directions ($p < 0.001$). At the same time the relatively hight amount of causalities oriented in the category both (27%) indicates that the direction of signal propagation in the arc is reduced in contrast to the daisy-chain CT1 structures. Concluding, that there is a certain amount of undirectionality generated by the arc pattern. The

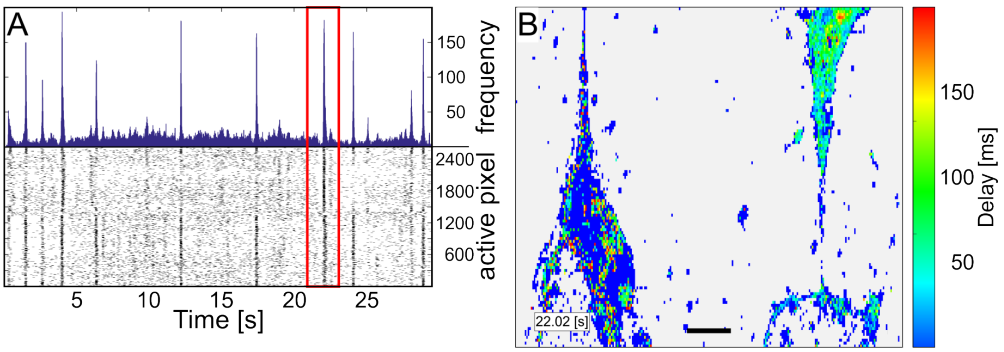

Figure 4.27: Signal propagation on an arc of a neuroCAP structure. **A**) Extracted activity from the recorded frame. Top row histogram of the activity per pixel depicted in the lower row. **B**) Delayed neuronal activity for the event highlighted with the red box in A. The excitation starts in the structure on the upper right and spreads into the arc, where the excitation extends across the entire structure. Scale bar: 200 μm.

remaining question, that can not be answered by Granger causality analysis is, if there is only arc spanning excitation or if there are also activities affecting a smaller region within the population.

Signal propagation on the arc of neuroCAP structures

To reveal if there are different pattern of neuronal activity occurring on the arc parts of the neuroCAP structures extracted intensity traces were analyzed with respect to their temporal correlations. The lower row in Figure 4.27 A indicates, that not every arising excitation affects the entire arc and adjacent pattern. The black marks, indicating the activity of each pixel, accumulate in different pattern, which do not necessarily involve all pixels. A clear separation between the lower and the upper half of the active pixels can be seen, at which the lower half exhibits a more synchronized firing pattern than the upper half of the active pixel. Even if the firing patterns are different, there are at least two events, that show a substrate spanning excitation (SSE) and the red box indicates one of them. Figure 4.27 B displays the activity on the recorded patter for the SSE highlighted in A. The excitation stars in the CT1 structure in the upper right and spreads towards the arc, where it triggers neuronal activity, that travels along the pattern and reaches the tip of the arc on the left side. Beside described only one other SSE occurs, all other excitation on the pattern only involve either the upper right structure, or parts of the arc.

For the categorization of arising events four different classes are established:

1) *in no out*: A signal reaches from an adjacent structure but does not trigger an output signal on the other side of the arc.

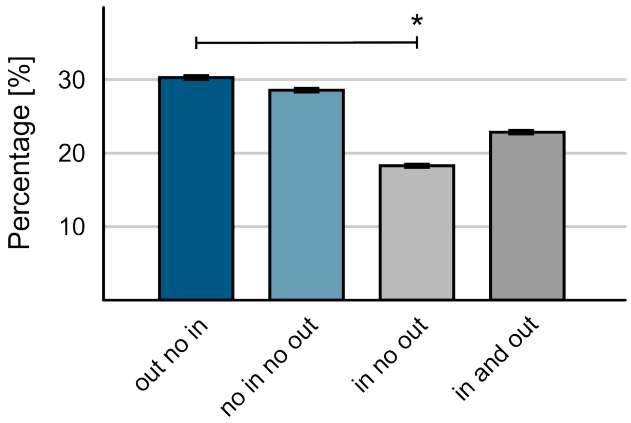

Figure 4.28: Statistics of propagating signals on arc parts of neuroCAP structure. Only 23 % signal propagation along the pattern could be observed in plots of delayed neuronal activity. The four categories represent the occurring cases of propagating signals. *: $p < 0.05$.

2) *out no in*: An output occurs at the tip of the arc without an input signal from an adjacent structure.
3) *no in no out*: An excitation within the population occurs without being triggered from an adjacent pattern. The arising excitation does not lead to an output signal of the arc.
4) *in and out*: An excitation enters at the base of the arc and activates the population. This activity travels to the tip of the arc, where it leaves the pattern and excites the population on the adjacent structure.

Analysis of the activity on all sequences recorded from 16 substrates reveals, that about 60% of the occurring signals in the arc structure are events spontaneously arising within the pattern, categorized as *out no in* and *no in no out*, see Figure 4.28. Due to the dimensions of the pattern, this spontaneous activity does not necessarily spread along the entire arc. Independent of the distance theses excitation travel roughly 50% of the signals are funneled towards the next CT1 structure, where they induce an excitation within the population. Here, neither for spontaneous activity arising from the arc pattern nor for activity starting in an adjacent population signal propagation against the orientation of the arc structure can be observed. On the other hand 56% of the signals, that have their origin in an adjacent structure, lead to an excitation of the population on the semicircular pattern resulting in an onward propagating signal (*in and out*). As a consequence it can be summarized that slightly more than half of all signals, that appear in the population on the arc pattern, lead to an onward propagation. At which only 23% of these signals have their origin in one of the daisy-chains within the neuroCAP structure.

4.5.4 Signals on the daisy-chain part of neuroCAP structures

The investigation of propagating signals in the daisy-chain part of the neuroCAP structures reveals, that the behavior observed for single daisy-chain strands is reproducible in the neuroCAPs. Figure 4.29 A shows a snap-shot of a calcium imaging sequence on a 5CT1 structure after 21 DIV. At the lower edge of the frame the beginning and the end of an arc structure can be spotted. The pattern on the right is exhibits a higher cell density than the one on the left part, but both sides are equally active during recordings. Figure section B reveals, that an excitation, that starts at the right structure, activates the arc and propagates towards the next CT1 pattern. The time of the first single event, that occurs during the excitation is noted in the box in the middle. Here it is clearly visible that a temporal delay between the two sides

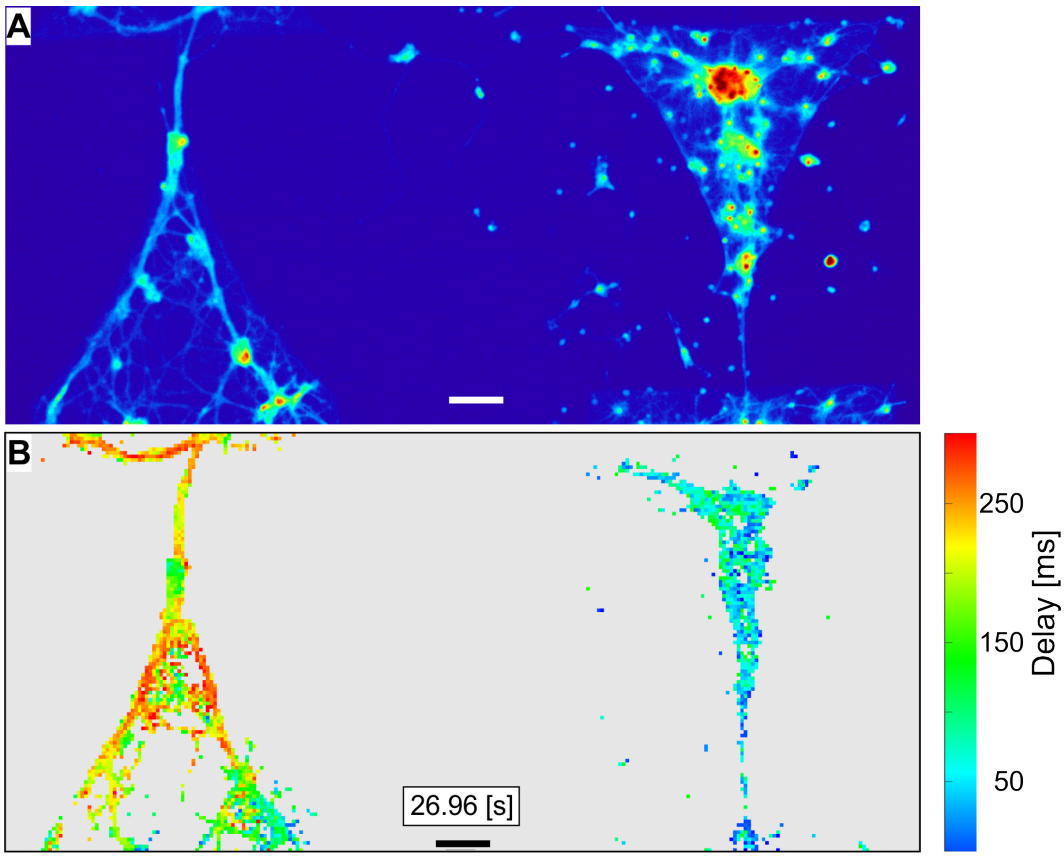

Figure 4.29: Signal propagation on the daisy-chain part of a neuroCAP structure. **A**) Snap-shot of the calcium imaging sequence. The two CT1 structures are directly adjacent to an arc part of the neuroCAP at the lower edge of the frame. **B**) Delayed neuronal activity on the pattern. An activity starting in the right side induces an excitation of the arc, what leads to an onward propagating signal on the left side. The box in the center indicates the time of the first single event of the excitation depicted in the image. Scale bar: 100 μm

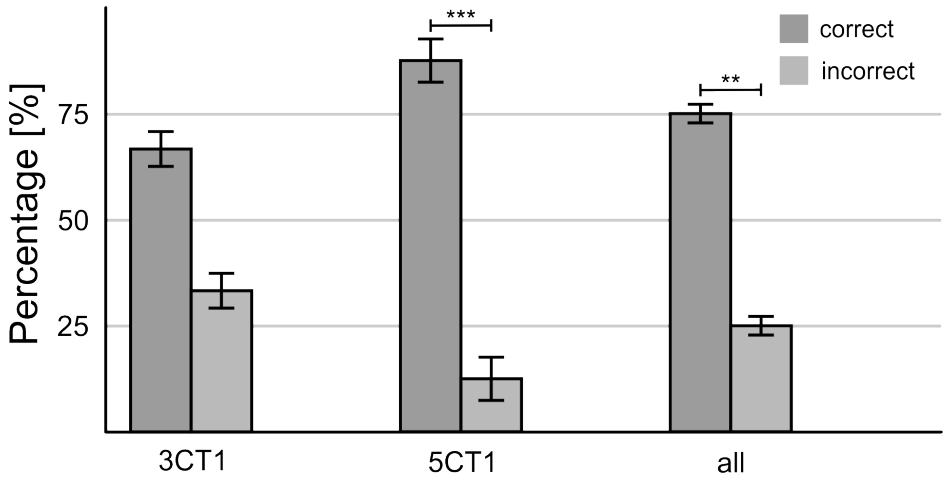

Figure 4.30: Orientation of signal propagation in the daisy chain part of the neuroCAP structure. Results for investigated 3CT1 and 5CT1 pattern are shown individually and the third column shows the averaged results for all recordings. ***: $p < 0.001$, **: $p < 0.05$

occurs, that is caused by the distance the excitation has to be traveled. Theses delay times and an approximation of the distance by a straight line and half circumference with a radius of 500 μm enable the calculation of the propagation speed on the pattern. As expected the resulting propagation velocity of 14 ± 3 mm/s does not differ from the one, that was reported earlier in Chapter 4.3.3. Also the orientation of the signal on the daisy-chain pattern shows comparable results to those on pure CT1 daisy-chains. But in contrast to the pure daisy-chains no signals propagating in both orientations could be observed during one sequence. As a consequence the events are categorized in correct and incorrect and the results are shown in Figure 4.30. For the 3CT1 design two third of the signals propagate in the correct orientation. Here, the difference between the two orientations is not as significant as for the 5CT1 design, where $87.5 \pm 5\%$ of the signals spread in the intended orientation, $p < 0.001$. Summing up the results of the activity on 3CT1 and 5CT1 pattern results in a significant difference for both directions, $p < 0.05$, with a preferential orientation along the pattern.

4.5.5 Signal propagation on neuroCAP structures

Beside the similar characteristics in signal propagation regarding orientation and speed the neuroCAP structures exhibits a clear difference in the frequency of occurring signals. For the pure daisy-chain structures discussed in Chapter 4.3 and 4.4 an excitation that spans the entire frame can be observed every 6.4 ± 1.1 seconds. In contrast to that the neuroCAP structures show a frame spanning activity in average every 3.6 ± 1.2 seconds. That means that the

network on neuroCAP pattern is excited almost twice as much as the pure daisy-chained CT1 structures. This effect can be attributed to the form of the network itself. For populations growing on pure daisy-chained CT1 pattern a signal mainly spreads along the funnel and thus along the line of structures. An excitation occurring on a line requires a new spontaneous activity and runs to a dead end at the end of the daisy-chain. The neuroCAP structures in contrast do not have a dead end. A spontaneous activity, that leads to an excitation of the surrounding population, spreads along the pattern and reaches its origin at some point in time. Here the hypothesis is, that it reactivates the cells on the pattern again and a self triggering activity arises.
Within a network of neurons pacemaker cells develop, that have different characteristics [9, 140, 141]. One of these is, that it fires burst of action potentials separated by an interval of silence. This process is a repetitive function, whereupon the inter-burst interval is not of a fixed length and depends on the input to the pacemaker cell itself. Here the outstanding question is if the firing frequency differs for the individual neuroCAP designs. Therefore the traveled distances for the neuroCAP designs are approximated. Within the daisy-chain the path is assumed as a straight line and for the arc a circumference with a radius of 500 μm is considered. This results in different path length ΔX for 3CT1 and 5CT1:

$$\begin{aligned} \Delta X_{3\mathrm{CT1}} &= 10,183\mu\mathrm{m} \\ \Delta X_{5\mathrm{CT1}} &= 12,783\mu\mathrm{m} \end{aligned}$$

Considering the calculated propagation velocity results in propagation time for one circulation Δt of:

$$\begin{aligned} \Delta t_{3\mathrm{CT1}} &= 727\mathrm{ms} \\ \Delta t_{5\mathrm{CT1}} &= 913\mathrm{ms} \end{aligned}$$

Now the question remains, if the frequency for these two structures is the same independent of the different path length. Assuming that every activity, that travels around the system generates a new activity would result in an inter-burst interval τ of less than one second, what is far below the observed value. In any case, it could be assumed, that τ is smaller for the 3CT1 design than for 5CT1. But the results from calcium imaging analysis reveal the opposite: $\tau_{3\mathrm{CT1}}$= 3.8 $\pm$ 1.3 s and $\tau_{5\mathrm{CT1}}$= 3.0 $\pm$ 1.4 s. Even though, the difference is small and the values are within the standard deviation, their difference is the reciprocal factor of the calculated propagation time $\Delta \approx 1.25$. However, the increase of network activity with network size corresponds with the findings of Yamamoto and colleagues [120, 121]. They showed, that the synchrony of

network activity increases with larger dimensions of the population and even the inter-burst interval reduces in that case. This is a reasonable explanation for the slight decrease of the inter-burst interval for the 5CT1 structures in comparison to the one found for 3CT1. To proof this hypothesis a variation of neuroCAP structures should be designed with different number of CT1 structures separating the arcs. Here a minimal number of one CT1 and a maximal number of six CT1 structures is suggested, as structures with a higher number of CT1 pattern exceed the dimension of the recordable frame size at the calcium-imaging setup.
Still, at this point it can only be speculated if there is any coincidence between the factor Δ, that appears to combine the two values and further investigations are required. For these experiments the whole structure and not a small fraction, as it was done for this thesis, should be investigated at the same time. With these settings a single excitation could be tracked along the entire pathway and signal loss within the pattern could be detected. As a consequence sources of signal loss could be identified that and measures could be taken to eliminate these sources. To this end, the large variation of the expected and measured propagation time and the correlation of inter-burst interval and structure size remains unexplained.

4.6 Calcium imaging in microfluidic systems

Calcium imaging is a powerful tool for the investigation of neuronal activity and propagating signals. The major application of calcium imaging, that is not covered by the described script so far is the use for microfluidic systems. As substrate bound proteins are not the only patterning technique used for neuronal populations applied in the Peter-Grünberg-Institute / Institute of Complex Systems, Bioelectronics (PGI-8/ICS-8) an adaptation of the analysis script to the investigated system design and different coating had to be performed. Here, these changes are explained and described in detail. These systems, which are used in the PGI-8/ICS-8 to investigate the directed connectivity between networks of neurons, are generally designed of two separated chambers, that are connected by microchannels. It is reported that the direction of axonal connectivity between the chambers can be tuned by choosing appropriate dimensioins of the microchannels [19]. To prove the selectivity of the channels, calcium imaging sequences are analysed with respect to signal propagation and Granger causality, comparable to that in Chapter 4.3.1. As a consequence of the microfluidic layout, the recorded frame is divided into three different parts for the analysis: two areas of the chambers (L and R in Figure 4.31 A) and one center area for the microchannels. Here, the person performing the experiment has to ensure that the microchannels are oriented parallel to one side of the frame. It is wise to select the long side of the frame to ensure a recording of a large active area within the chamber on either sides of the microchannels. The orientation of the microfluidic system has to be chosen in a selection box to adjust the analysis. In a next step the data are imported into the workspace and the separation in the different areas is applied. As it is nearly impossible to perfectly center the microchannels in the frame, both chambers are approximated with a larger area by reducing the length of the microchannels. Here, the attention is drawn to the two chambers as the Fluo-4 AM concentrates in the cytoplasm of the soma and while only axons and dendrites are located in the microchannels due to their dimensions. These neurites do not exhibit strong intensity changes and can be neglected in the analysis. Consequently, only the intensity changes in the chambers are included and the main data processing is performed independently for both chambers. For this analysis, the entire chamber is analyzed no selection of active pixels is performed. To reduce the total number of pixels and increase the calculation performance, an additional binning can be applied. For the analysis performed in Figure 4.32 a 10×10 binning is used, resulting in a resolution of 26×26 μm for every pixel. As previously described in Chapter 4.3.1, the extracted intensity traces are smoothed with a Savitzky and Golay filter to detect intensity changes caused by neuronal excitation, see Figure 4.31 B. The applied filter is based on a third order polynomial and has a width of 50 frames.

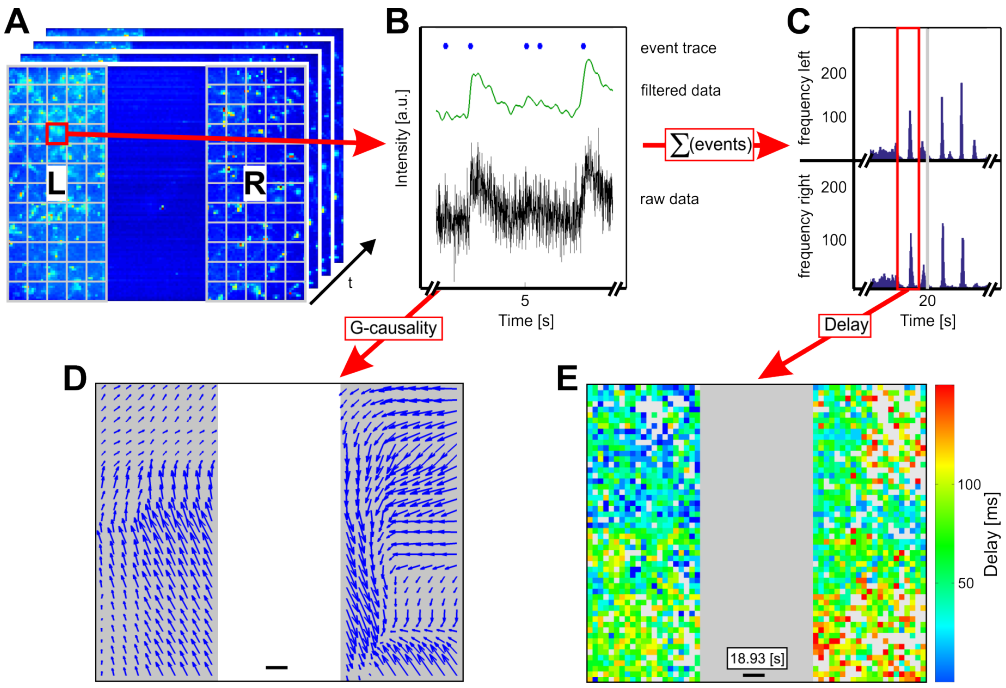

Figure 4.31: Work-flow of the MATLAB script for the analysis in microfluidic systems. **A**) Data from each chamber (L and R) are extracted separately by applying an additional binning. **B**) Events in resulting pixels are identified. **C**) The activity histogram over time for both chambers is generated to identify chamber spanning excitation and synchronism between the activity in the chambers. **D**) Conditional Granger causality analysis for both chambers is performed with an overlap of the chambers to account the connectivity by the microchannels. **E**) Plot of delayed neuronal activity in both chambers at 18.93 s. Scale bar in D) and E): 200 μm.

Event traces are used to identify chamber spanning excitation (CSE) for both chambers, see Figure 4.31 C. Individual CSEs in both chambers are analysed with respect to synchrony and direction of signal propagation. Therefore, the first single event of every individual CSE is identified and subsequently it is determined whether the one or the other chamber fires first and thus causes an excitation in the other. To allow a classification, delay plots for CSEs that occur in both chambers are generated. A categorization in A $\rightarrow$ B or B $\rightarrow$ A of the resulting plots need to be done by visual inspection. Figure 4.32 B shows an example of such a delay plot where it is visible that the activity occurs first in the left chamber and crosses the microchannels towards the right chamber, where an excitation is triggered. The insert in the center indicates the point in time of the first single event. The information about delayed activity is used to generate plots for pathway and averaged delay analysis, as described in Chapter 4.3.1. The only difference here is that both chambers are analyzed individually and the results for both analyses are plotted in a combined plot at the end.

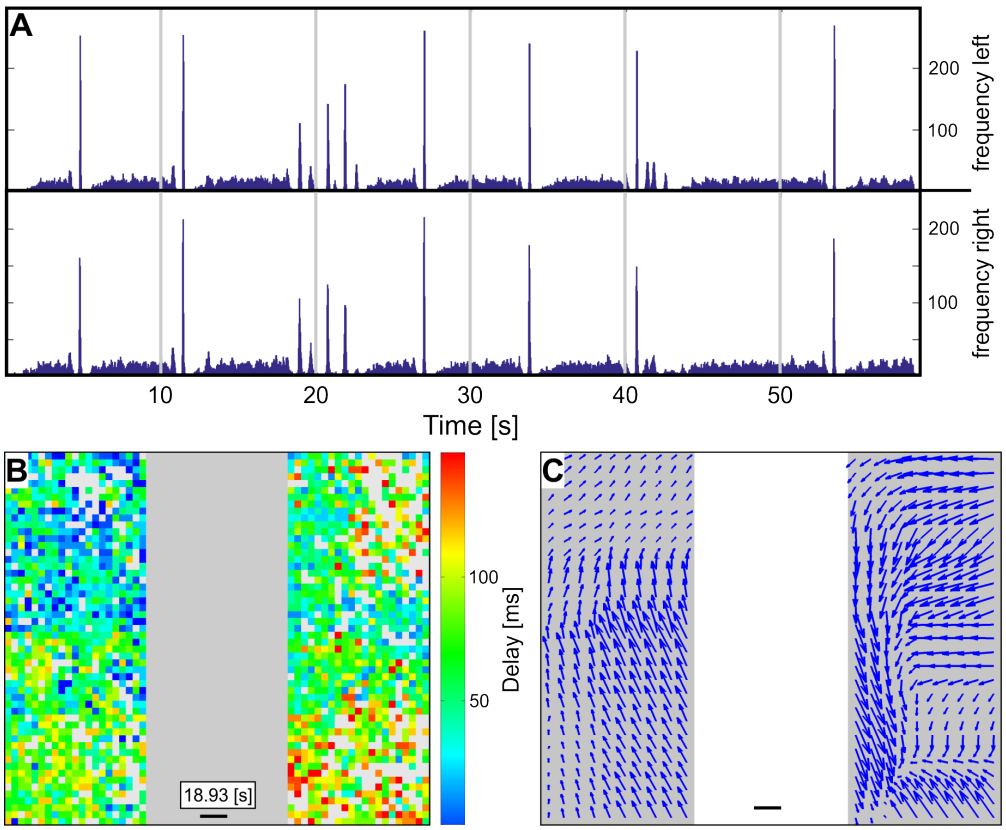

Figure 4.32: Results from calcium imaging analysis in micorfluidic systems. **A**) Histogram of all occurring single events over time. The upper row depicts the results from the left and the lower row from the right chamber. **B**) Example of a delay plot. The activity occurs first in the left chamber and spreads into the right one. The insert in the center indicates the time of the first single event. **C**) Granger causality plot. The arrows indicate the orientation of causal influence for every pixel. Scale bar for B) and C): 200 μm. Plots shown with permission by Dr. Kathrin Zobel.

In addition to the delay activity, conditional Granger causality analysis is performed on the recorded sequences. In contrast to the delay analysis, the chambers are not considered as two separated systems. An overlap of 200 μm on both sides is included in the calculations for each chamber. As a consequence the two chambers are assumed to be attached in the radial causality calculation. A resulting Granger causality plot for a radius of 300 μm is shown in Figure 4.32 C. Any kind of analysis of the resulting delay or causality plots was not part of this thesis and these plots are only meant as an example, to show the different fields of application of the MATLAB script. The plots shown in Figure 4.32 result from experiments performed by Dr. Kathrin Zobel and are shown with her permission.

5 Outlook

The generated system offers a lot of opportunities for further investigations and also improvements. So far the recording of neuronal activity was limited to a single point in time when the cells were labeled with calcium-sensitive dyes. To investigate the developmental changes of the network structure and the resulting alterations in connectivity succeeding experiments from one and the same network are required. But also a localized stimulation of single cells or small regions within the population offer multifaceted possibilities to gain further insides into network structure with a high local and temporal resolution. As a consequence, learning processes can be studied and insights to network plasticity could be at hand. Furthermore, the established system and the results from continuing experiments could be used to implement an *in silico* model system that helps understanding the mechanism of neuronal outgrowth and network formation. As all of these potential continuations and extensions are wide and complex fields itself they will be presented and discussed separately in the next section.

5.1 Genetically encoded calcium indicators

Conventional indicators of changing calcium ion concentration and membrane potentials are limited to a single experiment. Calcium indicators are mostly transferred to to the cytoplasm where they interact with the cell, whereas voltage sensitive dyes are bound to the lipid membrane. In both cases the cell is disturbed in its cultural environment and this causes cell death after a certain period of time. For the used Fluo-4 this is the case after roughly one hour of recordings. As a consequence the experiments reveal only a snap-shot of the connectivity within the population and only a fraction of the network can be studied in detail during this time. To investigate how the network evolves and how the connectivity is established and changed over time during development it is indispensable to record from one and the same population at different points in time. Whereupon, all recordings should be performed under the same conditions and with the same parameters, such as fluorescence intensity and reaction kinetics of the dye. Here, genetically encoded calcium indicators (GECIs) are a perfect choice that fulfill these criteria.

These indicators are fluorescent proteins derived from green fluorescent protein (GFP) fused with calmodulin (CaM), that are able to target specific cell types or intracellular compartments and can be summed up under the term of optogenetic indicators [142]. Beside the above mentioned advantages GECIs offer the opportunity to specifically target different types of cells and are continually replenished in them [143–145]. With this method exclusively neuronal signals can be recorded what is impossible with Fluo-4 as this dye also binds to glia cells, which also exhibit a changing intracellular calcium concentration. Here the challenging aspect is to bring the GECI into the neuron and build its DNA into the DNA of the cell, what starts the expression of the protein by the neuron. To achieve this DNA transfer cultured neurons are transduced with an adeno associated virus (AAV) carrying the transgene. AAVs are single strand DNA virus from the Paroviridae family [146]. The DNA of the GECI is loaded into AAV of the desired serotype, which infects the primary neurons and causes GECI expression within the cell. By choosing an appropriate serotype the selectivity for cell type and different compartments can be tuned. After the transduction the neuron incorporates the GECI DNA into its own DNA and starts the expression of indicators in the desired region. As the expression of proteins takes time recordings can be performed earliest after 7 days *post transduction* (DPT) with a sufficient and constant fluorescence intensity.

Different GECIs are available and the first attempt to use a GFP based calcium sensor was performed by Nakai 2001 [143], which consists of a cirucularly permutated enhanced GFP, a calcium-binding calmodulin (CaM), and a peptide. In this dye the CaM exhibits four calcium binding sites and changes its confirmation upon binding events [147]. By using CaM and fusing it to an EGFP the genetically encoded calcium indicator GCaMP was generated. This dye restores the original protonation status of EGPF upon calcium binding, what leads to the emission of fluorescence [143, 148, 149]. Since than several improvements have been carried out resulting in a pH and temperature insensitive version of the protein GCaMP3 [145, 150] with a maximum absorption at 497 nm and emission at 514 nm. In the Institute of Complex Systems 8 two different types of GCaMP3 are used: the cytoplamsic (GCaMP3-Cyt) and the plasmamembrane-bound (GCaMP3-PM) constructs, which are subcellularely localized as their name indicate.

Even though the changes in fluorescence intensity for GCaMP3 are lower than those for Fluo-4, successful recordings of intensity changes could be performed [151]. Figure 5.1 depicts the intensity change of a single neuron transduced with GCaMP3-Cyt recorded after 21 DIV and 14 DPT. The neuronal activity was triggered by a whole cell patch clamp stimulation. Every occurring rise in fluorescence intensity corresponds to single stimulation pulses that are temporally separated by 900 ms. As a consequence the transduction of neurons with GCaMP3 is

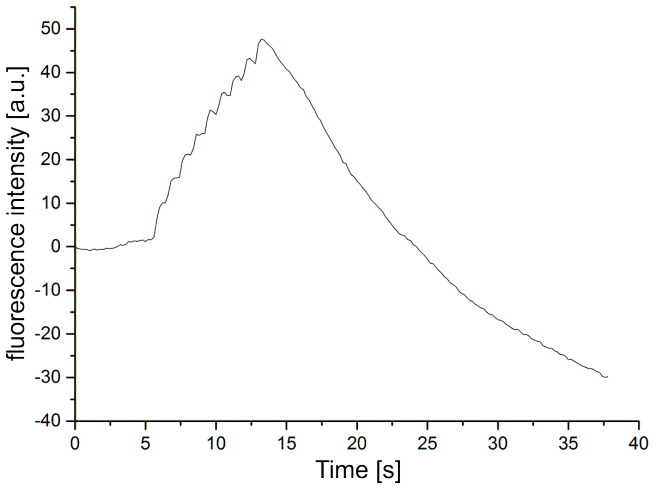

Figure 5.1: Recording of neuronal activity triggered by patch clamp stimulation with GCamP3-Cyt after 21 DIV and 14 days *post transduction*. Figure adapted from [151]

a suitable method to record spontaneous cellular activity at different points in time during the culture and could reveal processes of network plasticity.

5.2 Electrical recording and stimulation with microelectrode array

To overcome the temporal limitation of optical recordings of neuronal activity microelectrode array (MEA) recordings can be performed [152–154]. For these experiments cells are cultured on a chip that has a fixed number of electrodes from which potential as well as current changes can be recorded simultaneously. In the Peter-Grünberg-Institute 8 (PGI-8) and Institute of Complex Systems 8 (ICS-8) a device with 64 electrodes is used and the amplifier system allows recordings with a sampling rate of up to 10 kHz. That way single action potentials (AP) and bursts of AP can be recorded with a high accuracy from all electrodes at the same time. For technical reasons the electrodes are separated by a pitch of 100 μm resulting in a low spacial resolution. Furthermore the design, that commonly arranges the electrodes in a square, has to be changed to fit the daisy-chain design of the structures and even the neuroCAP pattern. Here, a linear arrangement of the electrodes in two lines is suggested with a pitch of 100 μm within the line and separation of the lines by 1000 μm. In this way cell signals on both daisy-chain arrangements of CT1 structures on the neuroCAP design can recorded. Thereby, every CT1 structure covers at least 6 electrodes. The protein pattern transfer to the MEA surface can be performed by microcontact printing that has to be aligned to the orientation of the

electrodes [155, 156], see Figure 5.2. With this technique signals of cardiac cells were guided along the electrodes [156] and the same should apply for neurons.
Crucial for the quality of electrical recordings with MEAs is the coverage of the electrode surface with cells as well as the coupling between the cells and the electrode. As a consequence a high cell density is desired to ensure a good coverage of the electrode. At the same time this is a critical point for patterning with substrate-bound proteins. A too high number of cells on the pattern causes the loss of exclusive cell growth on the pattern. Here a trade of has to be made between a good electrode coverage on the one and patterned growth on the other side. Furthermore, the electrode surface can be modified to improve the cell-chip-coupling and signal to noise ratio, such as implementing 3D structures [157, 158] and nanocavities [159] .
Beside recording of potential changes of the cell membrane also the current flow across the membrane can be recorded. Furthermore, a stimulation on single electrode can be performed. Whereupon the stimulating electrode can be chosen freely among all. At the same time the changes at the other 63 electrodes can be recorded. In this way the network can be excited locally and the impact on of stimulation on different positions within the population can be studied. This at the end, offers a versatile tool to investigate propagating signals and the network response to stimulation with a high temporal resolution.

5.3 Optogenetic stimulation

The stimulation with MEAs is not capable to reveal the impact of patterned cell growth on signal propagation on a single cell level. It rather provides information about the impact of a region within the population on activity on the entire pattern. To disclose finer structure of a population and the connectivity between single cells a more elegant way of stimulation can be applied, optogenetic stimulation. There is a broad variety of fluorescent protein tags that can be used and cover most of the visual [160] and parts of the near infrared spectrum [161]. The basis for optogenetic actuators is formed by Channelrhodopsin that conducts ions directly and was first discovered by Nagel et al. [162]. It exhibits a very fast response time [163] and opens upon exposure to 380 nm light [164]. The entire mechanism of light activation and ion channel opening is described by Gajewski et al. [165] and shall not be explained in this section, here the focus lies on the application of the optogenetic stimulation.
This method can be used to stimulate single cells, like depicted in Figure 5.2. But also the excitation of a cascade of cells can be performed by subsequent stimulation. Therefore, a microscopy setup with a laser unit is required that is coupled into the optical path, that allows focusing of the laser spot to a single cell. Different applications for the optical stimulation

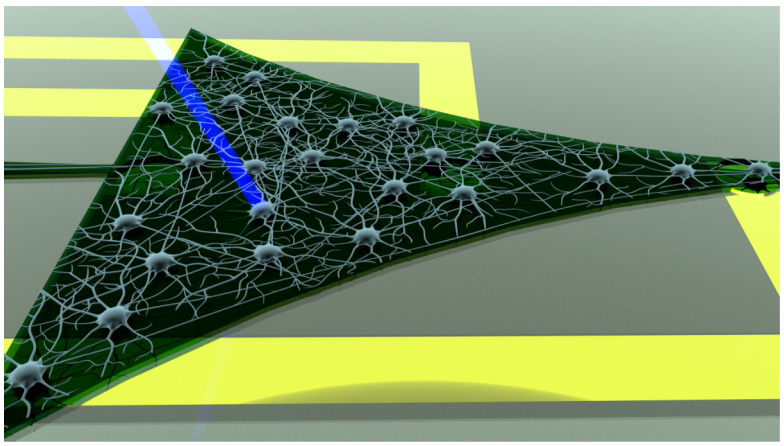

Figure 5.2: Sketch of a neuronal population grown on a CT structure printed on a MEA. The blue beam depicts optogenetic stimulation of a single cell within the population.

can be used. On the one hand it can be combined with MEA recordings resulting in a locally defined stimulation with high temporal resolution recording. While on the other hand a combination with optical recordings is also applicable. In this case the spectra of the excitation of Channelrhodopsin and the ion sensitive dye need to be separated. As a consequence Fluo-4 can not be used for this purpose but there are other dyes with a comparable kinetic that operate in another spectrum such as Fura-2. However, for simultaneous optical stimulation and recording the optical components within the setup have to be chosen carefully. Concluding, a combination of optical recording and stimulation together with MEA recordings is conceivable in any possible permutation and offers a powerful tool to investigate network communication.

5.4 Applications for the established system

The cellular system presented in this thesis offers a vast range of application. In combination with the above described extensions of the toolbox for investigation of the system issues of sophisticated complexity can be addressed. On the one hand the development of signaling pathways can be revealed in detail by recording neuronal activity on different points in time with optogenetic techniques. At the same time these techniques can also be used to stimulate cells within the pathway and determine their impact on the pathway by changes in connectivity. Stimulating cells that do not belong to preferential pathways opens a window to changes in network plasticity and learning processes. In this way the impact of guided outgrowth of axons and dendrites can be investigated regarding the connectivity between populations of neurons. Furthermore the signalling cascades can be identified and sources of signal loss can be determined, what helps understanding signal processing within a neuronal population.

Another application that arises from the characteristics of populations grown on neuroCAP structures are logical device, such as those presented by Feinerman and colleagues [26] as well as Wei et al. [166]. Whereupon only Feinerman was able to realize structures that exceed diode like behaviour, by implementing a threshold and an AND gate *in vitro*. The neuroCAP design could be extended in a way that an excitation, that propagates along the pattern is split at a certain point of the structure. One part of the excitation continues spreading along the neuroCAP, whereas the other part activates a population on an additional pattern which leads the signal to a point, where it is compared with a second signal from another neuroCAP structure. At this point it can only be speculated if the different dimensions of the presented neuroCAP structures have an impact on the phase of a circulating signal. But assuming that this is true logic comparators such as AND, OR, and NOR gates could be generated.
The fact that the neuroCAP structure generates neuronal population, whose properties can be characterized in great detail, offers a model system for various applications. Here, the recovery of the neuronal network after lesion [167] could be investigated. This would improve our knowledge about neuronal regeneration and offers the chance to identify single aspects that improve recapture full functionality of the network. But also other disturbances of the functionality are conceivable, that could open a window to a increasing problem of our society: neurodegenerative diseases such as Alzheimer's disease (AD). About 6% of the population aged over 65 is affected by AD with an increase in incidence with age [168]. Up to now, it remains unclear what the reason for AD is while a number of risk factors is identified. Anyhow, multiple indicators for the disease can be identified several years before a clinical diagnosis of AD is possible [169]. As AD is a chronic progressive neurodegenerative disorder, it is of paramount importance that these evidence can be identified as early as possible to offer the chance to slow down or stop the progression of the disease. One reason for the nerve damage results from the conversion of normal, nontoxic monomers and small oligomers of amyloid β peptide 1-42 (Aβ) to toxic oligomers and protofibrils [170, 171]. The mechanism by which misfolded Aβ leads to synapse loss and neuronal cell death are currently under investigation. So far it is known, that misfolded Aβ accumulates as plaques [172, 173] in cell bodies, axons and synapses [174–176]. These plaques are the primary histological feature of AD [177–179], that can be found in an early stage of the disease.
With the neuroCAP design a model system is at hand, that enables the identification of disturbances of signal propagation at an early stage. By a local drug induced generation of Aβ plaques a spreading of the plaques across the population can be observed and various approaches could be tried to slow down the progression. At the same time measures for the regeneration of nervous tissue can be investigated that reverse the misfolding of the peptide.

List of Figures

2.1 Primary neuron 5
2.2 Neuronal cell membrane 7
2.3 Equivalent circuit for cell membrane 8
2.4 Neuronal action potential 9
2.5 Schematic of the neuronal development. 13
2.6 SPM measurements of the thickness of printed protein layers. 16
2.7 Antibody binding 18

3.1 Molding of POP and PDMS stamps 22
3.2 Structure design 23
3.3 Design of neuroCAP structures 24
3.4 Microcontact printing with PDMS stamps 26

4.1 Protein transfer 34
4.2 Cell growth on pattern printed with PDMS and POP stamps. 35
4.3 Stitched images of four SC1F structures 36
4.4 Analysis of live cell imaging data 39
4.5 Comparison of axonal turn angles on homogeneous and patterned substrates . 40
4.6 Live cell imaging on a CT1 structure 42
4.7 History model of axonal growth. 43
4.8 Trajectories of modeled axonal growth. 44
4.9 Neuronal growth at the edge of a protein pattern. 45
4.10 Neurite growth at a CT1 gateway after 14 DIV. 47
4.11 Dendritic growth at the gateway of different structures. 48
4.12 Orientation of axonal and dendritic growth at the gateway. 49
4.13 Work-flow for Ca-imaging analysis with MATLAB. 53
4.14 Thresholding to identify active traces. 54
4.15 Savitzky-Golay filter comparison. 56
4.16 Granger-causality calculation. 58

4.17 Different influence radius for Granger conditional causality analysis. 59
4.18 Direction of conditional Granger-causality at the gateway. 61
4.19 Signal propagation on CT2 structure 63
4.20 Results from propagation analysis 64
4.21 Averaged sum of activity for pathway analysis. 65
4.22 Averaged delayed activity for pathway analysis. 66
4.23 Cell growth on neuroCAP arc. 71
4.24 Two possible kinds of arrangement for ca-imaging on neuroCAPs. 72
4.25 GCCA of an arc of a neuroCAP structure. 73
4.26 GCCA analysis of the arc in neuroCAP pattern. 74
4.27 Signal propagation on an arc of a neuroCAP structure. 75
4.28 Statistics of propagating signals on arc parts. 76
4.29 Signal propagation on the daisy-chain part of a neuroCAP structure. 77
4.30 Orientation of signal propagation in the daisy chain part of the neuroCAP. . . 78
4.31 Work-flow of the MATLAB script for the analysis in microfluidic systems. . . 82
4.32 Results from calcium imaging analysis in micorfluidic systems. 83

5.1 Recording of neuronal activity with GCamP3. 87
5.2 Sketch of a population grown on a CT structure on a MEA with optical stimulation. 89

A.1 Design of base curvature variations. 113
A.2 Change of axonal polarity during development. 114
A.3 Axonal turn angle on patterned substrates. 115
A.4 Base variation at a CT1. 116
A.5 Thresholding fluorescence intensity for recognition of active pixels. 117
A.6 Neuronal growth on on a 3CT1 neuroCAP structure. 118

List of Tables

2.1 Characteristics of different Ca^{2+}-indicators. 20

4.1 Number of cells on substrates and resulting cell density. 37
4.2 Orientation Granger causality on different structures. 60
4.3 Orientation of neurite growth and signal propagation on different different structures. 68

Bibliography

[1]T. Willis. *Cerebri anatome: cui accessit nervorum descriptio et ususe*. Londini : typis Ja. Flesher, impensis Jo. Martyn & Ja. Allestry apud insigne Campanae in Coemeterio D. Pauli, London, 1664.

[2]L. Galvani. De viribus electricitatis in motu musculari commentarius. *De Bononiensi Scientiarum et Artium Instituto atque Academia Commentarii*, 7:363–418, 1791.

[3]L. Galvani, R.M. Green, and G. Aldini. *De viribus electricitatis in motu musculari commentarius : a translation of luigi Galvani's de viribus electricitatisin motu musculari commentarius*. Licht, 1953.

[4]C Golgi. Intorno alla struttura delle cellule nervose. *Bollettino della Società Medico-Chirurgica di Pavia*, 13:3–16, 1898.

[5]S. Ramón Cajal. Estructura de los centros nerviosos de las aves. *Rev. Trim. Histol. Norm. Pathol.*, 1:1–10, 1888.

[6]A. Hodgkin and A. Huxley. Action Potentials Recorded from Inside a Nerve Fibre. *Nature*, 144:710–711, 1939.

[7]D.E. Goldman. Potential, impedence, and rectification in membranes. *J. Gen. Physiol.*, 27:37–60, 1943.

[8]A.L. Hodgkin and B. Katz. The effect of sodium ions on the electrical activity of the giant axon of the squid. *J. Physiol.*, 108:37–77, 1949.

[9]E. Kandel, J. H. Schwartz, and T. M. Jessell. *Principles of Neural Science*. McGraw-Hill Medical, 4 edition, 2000.

[10]S. Song, P.J. Sjöström, M. Reigl, S. Nelson, and D.B. Chklovskii. Highly Nonrandom Features of Synaptic Connectivity in Local Cortical Circuits. *PLoS Biology*, 3:e68, mar 2005.

[11]V.B. Mountcastle. Modality and topographic properties neurons of cat's somatic sensory. *J. Neurophysiol.*, 20:408–434, 1956.

[12]D.H. Hubel, T.N. Wiesel, and M.P. Stryker. Orientation columns in macaque monkey visual cortex demonstrated by the 2-deoxyglucose autoradiographic technique. *Nature*, 269:328–330, 1977.

[13]E.M. Leise. Modular construction of nervous systems: a basic principle of design for invertebrates and vertebrates. *Brain Res. Brain Res. Rev.*, 15:1–23, jan 1990.

[14]D.P. Buxhoeveden. The minicolumn hypothesis in neuroscience. *Brain*, 125:935–951, may 2002.

[15]F.C. de Anda, G. Pollarolo, J.S. Da Silva, P.G. Camoletto, F. Feiguin, and C.G. Dotti. Centrosome localization determines neuronal polarity. *Nature*, 436:704–708, 2005.

[16]L.J. Richards, S.E. Koester, R. Tuttle, and D.D.M.O. Leary. Directed Growth of Early Cortical Axons Is Influenced by a Chemoattractant Released from an Intermediate Target. *J. Neurosci.*, 17:2445–2458, 1997.

[17]N. Arimura and K. Kaibuchi. Neuronal polarity: from extracellular signals to intracellular mechanisms. *Nat. Rev. Neurosci.*, 8:194–205, 2007.

[18]P. Rakic. The radial edifice of cortical architecture: from neuronal silhouettes to genetic engineering. *Brain research reviews*, 55:204–219, 2007.

[19]J.M. Peyrin, B. Deleglise, L. Saias, M. Vignes, P. Gougis, S. Magnifico, S. Betuing, M. Pietri, J. Caboche, P. Vanhoutte, J.L. Viovy, and B. Brugg. Axon diodes for the reconstruction of oriented neuronal networks in microfluidic chambers. *Lab Chip*, 11:3663–3673, 2011.

[20]L.J. Millet and M.U. Gillette. New perspectives on neuronal development via microfluidic environments. *Trends Neurosci.*, 35:752–761, 2012.

[21]J. Park, S. Kim, S.I. Park, Y. Choe, J. Li, and A. Han. A microchip for quantitative analysis of CNS axon growth under localized biomolecular treatments. *J. Neurosci. Meth.*, 221:166–174, 2014.

[22]M. Verhulsel, M. Vignes, S. Descroix, L. Malaquin, D.M. Vignjevic, and J.-L. Viovy. A review of microfabrication and hydrogel engineering for micro-organs on chips. *Biomaterials*, 35:1816–1832, 2014.

[23]T. Isomura, K. Shimba, Y. Takayama, A. Takeuchi, K. Kotani, and Y. Jimbo. Signal transfer within a cultured asymmetric cortical neuron circuit. *J. Neural Eng.*, 12:066023, 2015.

[24]O. Feinerman, M. Segal, and E. Moses. Signal propagation along unidimensional neuronal networks. *J. Neurophysiol.*, 94:3406–3416, 2005.

[25]S.B.N. Biancardo, H.J. Pranov, and N.B. Larsen. Protein in-mold patterning. *Adv. Mater.*, 20:1825–1829, 2008.

[26]O. Feinerman, A. Rotem, and E. Moses. Reliable neuronal logic devices from patterned hippocampal cultures. *Nat. Phy.*, 4:967–973, 2008.

[27]N. Li and C.-M. Ho. Photolithographic patterning of organosilane monolayer for generating large area two-dimensional B lymphocyte arrays. *Lab Chip*, 8:2105–2112, 2008.

[28]B.C. Wheeler and G.J. Brewer. Desingning neural networks in culture. *Proc. IEEE*, 98:398–406, 2010.

[29]M.A. Scott, Z.D. Wissner-Gross, and M.F. Yanik. Ultra-rapid laser protein micropatterning: screening for directed polarization of single neurons. *Lab Chip*, 12:2265–2276, 2012.

[30]A. Bernard, E. Delamarche, H. Schmid, B. Michel, H.R. Bosshard, and H. Biebuyck. Printing patterns of proteins. *Langmuir*, 14:2225–2229, 1998.

[31]S. Roth, G. Bugnicourt, M. Bisbal, S. Gory-Faure, J. Brocard, C. Villard, and S. Gory-Fauré. Neuronal architectures with axo-dendritic polarity above silicon nanowires. *Small*, 8:671–675, 2012.

[32]D. Schwaab, P. Zentis, S. Winter, S. Meffert, A. Offenhäusser, and D. Mayer. Generation of Protein Nanogradients by Microcontact Printing. *Jpn. J. Appl. Phys.*, 52:05DA19, 2013.

[33]J. Albers, K. Toma, and A. Offenhäusser. Engineering connectivity by multiscale micropatterning of individual populations of neurons. *Biotechnol. J.*, 10:332–338, 2015.

[34]S.G. Turney and P.C. Bridgman. Laminin stimulates and guides axonal outgrowth via growth cone myosin II activity. *Nat. Neurosci.*, 8:717–719, 2005.

[35]M.J. Jang and Y. Nam. Geometric effect of cell adhesive polygonal micropatterns on neuritogenesis and axon guidance. *J. Neural. Eng.*, 9:46019–46029, 2012.

[36]W. Goldmann. Mechanical aspects of cell shape regulation and signaling. *Cell Biol. Int.*, 26:313–317, 2002.

[37]A.J. Ingram, H. Ly, K. Thai, M. Kang, and J.W. Scholey. Activation of mesangial cell signaling cascades in response to mechanical strain. *Kidney Int.*, 55:476–485, 1999.

[38]P.A. Janmey. The cytoskeleton and cell signaling: Component localization and mechanical coupling. *Physiol Rev*, 78:763–781, 1998.

[39]D. Brüggemann, B. Wolfrum, V. Maybeck, Y. Mourzina, M. Jansen, and A. Offenhäusser. Nanostructured gold microelectrodes for extracellular recording from electrogenic cells. *Nanotechnology*, 22:265104, 2011.

[40]D.J Aidley. *The physiology of excitable cells.* Cambridge University Press, 4 edition, 1998.

[41]M.J. Berridge. Neuronal calcium signaling. *Neuron*, 21:13–26, 1998.

[42]S. Poliak and E. Peles. The local differentiation of myelinated axons at nodes of Ranvier. *Nat. Revi. Neurosci.*, 4:968–980, 2003.

[43]M. Simons and J. Trotter. Wrapping it up: the cell biology of myelination. *Curr. Opin. Neurobiol.*, 17:533–540, 2007.

[44]R.S. Lillie. Factors affecting transmission and recovery in the passive iron nerve model. *J. Gen. Physiol.*, 7:473–507, 1925.

[45]I. Tasaki. The electro-saltatory transmission of the nerve impulse and the effect of narcosis upon the nerve fiber. *Am. J. Physiol.*, 127:211–227, 1939.

[46]I. Tasaki and T. Takeuchi. Der am Ranvierschen Knoten entstehende Aktionsstrom und seine Bedeutung für die Erregungsleitung. *Pflugers Arch. Gesamte Physiol. Menschen Tiere*, 244:696–711, 1941.

[47]A. F. Huxley and R. Stämpeli. Evidence for saltatory conduction in peripheral myelinated nerve fibres. *J. Physiol.*, 108:315–339, 1949.

[48]W. Thomson. On the theory of the electric telegraph. *Proc. R. Soc. Lon.*, 7:382–399, 1855.

[49]A.L. Hodgkin and W.A.H. Rushton. The electrical constants of a crustacean nerve fibre. *Proc. R. Soc. B: Biol. Sci.*, 133:444–479, 1946.

[50]T.C. Ruch and H.D. Patton. *Physiology and biophysics*. Saunders (W.B.) Co Ltd, Philadelphia, 20 edition, 1982.

[51]S.D. Graber. *Biology: A self-teaching guide*. John Wiley & Sons, 2nd edition, 2002.

[52]W.W. Lytton. *From computer to brain - Foundations of computational neuroscience.* Springer New York, 1 edition, 2002.

[53]J. Albers. Axonale Dioden - Einfluss von 1- und 2-D Proteinstrukturen auf gerichteten Informationsfluss in neuronalen Systemen. Master's thesis (Diplomarbeit), RWTH Aachen University, 2012.

[54]Y. Fukata, T. Kimura, and K. Kaibuchi. Axon specification in hippocampal neurons. *Neurosci. Res.*, 43:305–315, 2002.

[55]G. Ruthel and P.J. Hollenbeck. Growth cones are not required for initial establishment of polarity or differential axon branch growth in cultured hippocampal neurons. *J. Neurosci.*, 20:2266–2274, 2000.

[56]C. Jacobson, B. Schnapp, and G.A. Banker. A change in the selective translocation of the Kinesin-1 motor domain marks the initial specification of the axon. *Neuron*, 49:797–804, 2006.

[57]C.G. Dotti, C.A. Sullivan, and G.A. Banker. The establishment of polarity by hippocampal neurons in culture. *J. Neurosci.*, 8:1454–1468, 1988.

[58]A.M. Craig and G. Banker. Neuronal polarity. *Annu. Rev. Neurosci.*, 17:267–310, 1994.

[59]S.S.L. Andersen and G.-Q. Bi. Axon formation: a molecular model for the generation of neuronal polarity. *BioEssays*, 22:172–179, 2000.

[60]K. Goslin and G. Banker. Experimental observations on the development of polarity by hippocampal neurons in culture. *J. Cell Biol.*, 108:1507–1516, 1989.

[61]E.M. Hedgecock, J.G. Culotti, and D.H. Hall. The unc-5, unc-6, and unc-40 genes guide circumferential migrations of pioneer axons and mesodermal cells on the epidermis in C. elegans. *Neuron*, 4:61–85, 1990.

[62]T. Serafini, T.E. Kennedy, M.J. Gaiko, C. Mirzayan, T.M. Jessell, and M. Tessier-Lavigne. The netrins define a family of axon outgrowth-promoting proteins homologous to C. elegans UNC-6. *Cell*, 78:409–424, 1994.

[63]W.G. Wadsworth, H. Bhatt, and E.M. Hedgecock. Neuroglia and pioneer neurons express UNC-6 to provide global and local netrin cues for guiding migrations in C. elegans. *Neuron*, 16:35–46, 1996.

[64]K. Hong, L. Hinck, M. Nishiyama, M.-M. Poo, M. Tessier-Lavigne, and E. Stein. A ligand-gated association between cytoplasmic domains of UNC5 and DCC family receptors converts netrin-induced growth cone attraction to repulsion. *Cell*, 97:927–941, 1999.

[65]K.L. Whitford, P. Dijkhuizen, F. Polleux, and A. Ghosh. Molecular control of cortical dendrite development. *Annu. Rev. Neurosci.*, 25:127–149, 2002.

[66]B.C. Prasad and S.G. Clark. Wnt signaling establishes anteroposterior neuronal polarity and requires retromer in C. elegans. *Development*, 133:1757–1766, 2006.

[67]M.A. Hilliard and C.I. Bargmann. Wnt signals and frizzled activity orient anterior-posterior axon outgrowth in C. elegans. *Dev. Cell*, 10:379–390, 2006.

[68]F.R. Zolessi, L. Poggi, C.J. Wilkinson, C.-B. Chien, and W.A. Harris. Polarization and orientation of retinal ganglion cells in vivo. *Neural Dev.*, 1:2, 2006.

[69]F.C. de Anda, A. Gartner, L.H. Tsai, and C.G. Dotti. Pyramidal neuron polarity axis is defined at the bipolar stage. *J. Cell. Sci.*, 121:178–185, 2008.

[70]J.H. Miner and P.D. Yurchenco. Laminin functions in tissue morphogenesis. *Annu. Rev. Cell Dev. Biol.*, 20:255–284, 2004.

[71]I. Selak, J.M. Foidart, and G. Moonen. Laminin promotes cerebellar granule cells migration in vitro and is synthesized by cultured astrocytes. *Dev. Neurosci.*, 7:278–285, 1985.

[72]P. Liesi, G. Hager, H.-U. Dodt, I. Seppälä, and W. Nsberger. Domain-specific antibodies against the B2 chain of laminin inhibit neuronal migration in the neonatal rat cerebellum. *J. Neurosci. Res.*, 40:199–206, 1995.

[73]M.J. Ignatius, T.H. Large, M. Houde, J.W. Tawil, A. Barton, F. Esch, S. Carbonetto, and L.F. Reichardt. Molecular cloning of the rat integrin alpha 1-subunit: a receptor for laminin and collagen. *J. Cell Biol.*, 111:709–720, 1990.

[74]N.J. Tawil, M. Houde, R. Blacher, F. Esch, L.F. Reichardt, D.C. Turner, and S. Carbonetto. Alpha 1 beta 1 integrin heterodimer functions as a dual laminin/collagen receptor in neural cells. *Biochem.*, 29:6540–6544, 1990.

[75]D G Jay. A Src-astic response to mounting tension. *J. Cell Biol.*, 155:327–30, 2001.

[76]S. Woo and T.M. Gomez. Rac1 and RhoA promote neurite outgrowth through formation and stabilization of growth cone point contacts. *J. Neurosci.*, 26:1418–1428, 2006.

[77]R.O. Hynes. Integrins: versatility, modulation, and signaling in cell adhesion. *Cell*, 69:11–25, 1992.

[78]M.E. Hemler. Integrins. In T. Kreis and R. Vale, editors, *Guidebook to the Extracellular Matrix and Adhesion Proteins*. Sambrook and Tooze Publishers, Oxford University Press, 1999.

[79]R.O. Hynes. Cell adhesion: old and new questions. *Trends Cell Biol.*, 9:M33–M37, 1999.

[80]M.D. Henry and K.P. Campbell. Dystroglycan: an extracellular matrix receptor linked to the cytoskeleton. *Curr. Opin. Cell Biol.*, 8:625–31, 1996.

[81]M.A. Schwartz, M.D. Schaller, and M.H. Ginsberg. Integrins: emerging paradigms of signal transduction. *Annu Rev. Cell Dev. Biol.*, 11:549–599, 1995.

[82]E.A. Clark and J.S. Brugge. Integrins and signal transduction pathways: the road taken. *Science*, 268:233–239, 1995.

[83]F.G. Giancotti. Integrin signaling: specificity and control of cell survival and cell cycle progression. *Curr. Opin. Cell Biol.*, 9:691–700, 1997.

[84]G.S. Withers, C.D. James, C.E. Kingman, H.G. Craighead, and G.A. Banker. Effects of substrate geometry on growth cone behavior and axon branching. *J. Neurobiol.*, 66:1183–1194, 2006.

[85]A.K. Vogt, L. Lauer, W. Knoll, and A. Offenhäusser. Micropatterned substrates for the growth of functionla neuronal networks of defined geometry. *Biotechnol. Prog.*, 19:1562–1568, 2003.

[86]A.K. Vogt, F.D. Stefani, A. Best, G. Nelles, A. Yasuda, W. Knoll, and A. Offenhausser. Impact of micropatterned surfaces on neuronal polarity. *J. Neurosci. Meth.*, 134:191–198, 2004.

[87]A.K. Vogt, G.J. Brewer, T. Decker, S. Bocker-Meffert, V. Jacobsen, M. Kreiter, W. Knoll, and A. Offenhausser. Independence of synaptic specificity from neuritic guidance. *Neurosci.*, 134:783–790, 2005.

[88]A.C. von Philipsborn, S. Lang, J. Loeschinger, A. Bernard, C. David, D. Lehnert, F. Bonhoeffer, and M. Bastmeyer. Growth cone navigation in substrate-bound ephrin gradients. *Development*, 133:2487–2495, 2006.

[89]R. Fricke, P.D. Zentis, L.T. Rajappa, B. Hofmann, M. Banzet, A. Offenhausser, and S.H. Meffert. Axon guidance of rat cortical neurons by microcontact printed gradients. *Biomaterials*, 32:2070–2076, 2011.

[90]H. Yamamoto, T. Demura, M. Morita, G.A. Banker, T. Tanii, and S. Nakamura. Differential neurite outgrowth is required for axon specification by cultured hippocampal neurons. *J. Neurosci.*, 123:904–910, 2012.

[91]U. Derra. Studying Signal Propagation in Patterned Cell Networks by Optical Recordings by. Master's thesis, RWTH Aachen University, 2014.

[92]A. Kumar and G.M. Whitesides. Features of gold having micrometer to centimeter dimensions can be formed through a combination of stamping with an elastomeric stamp and an alkanethiol ink followed by chemical etching. *Appl. Phys. Lett.*, 63:2002, 1993.

[93]J.L. Wilbur, A. Kumar, H.A. Biebuyck, E. Kim, and G.M. Whitesides. Microcontact printing of self-assembled monolayers: applications in microfabrication. *Nanotechnology*, 7:452–457, 1996.

[94]A. Offenhäusser, S. Böcker-Meffert, T. Decker, R. Helpenstein, P. Gasteier, J. Groll, M. Möller, A. Reska, S. Schäfer, P. Schulte, and A. Vogt-Eisele. Microcontact printing of proteins for neuronal cell guidance. *Soft Matter*, 3:290–298, 2007.

[95]C. Wendeln and B.J. Ravoo. Surface patterning by microcontact chemistry. *Langmuir*, 28:5527–5538, 2012.

[96]R Singhvi, A Kumar, G P Lopez, G N Stephanopoulos, D I Wang, G M Whitesides, and D E Ingber. Engineering cell shape and function. *Science (New York, N.Y.)*, 264(5159):696–698, apr 1994.

[97]L.M. Tender, R.L. Worley, H. Fan, and G.P. Lopez. ElectrochemicalpPatterning of self-assembled monolayers onto microscopic arrays of gold electrodes fabricated by laser ablation. *Langmuir*, 12:5515–5518, 1996.

[98]K.L. Prime and G.M. Whitesides. Adsorption of proteins onto surfaces containing end-attached oligo (ethylene oxide): a model system using self-assembled monolayers. *J. Am. Chem. Soc.*, 115:10714–10721, 1993.

[99]E. Delamarche, A. Bernard, H. Schmid, B. Michel, and H. Biebuyck. Patterned delivery of immunoglobulins to surfaces using microfluidic networks. *Science*, 276:779–781, 1997.

[100]M. Mrksich and G.M. Whitesides. Using self-assembled monolayers to understand the interactions of man-made surfaces with proteins and cells. *Annu. Revi. Biophys. Biomol. Struct.*, 25:55–78, 1996.

[101]C.D. James, R.C. Davis, L. Kam, H.G. Craighead, M. Isaacson, J.N. Turner, and W. Shain. Patterned protein layers on solid substrates by thin stamp microcontact printing. *Langmuir*, 14:741–744, 1998.

[102]E. Delamarche, H. Schmid, A. Bietsch, N. B. Larsen, H. Rothuizen, B. Michel, and H. Biebuyck. Transport mechanisms of alkanethiols during microcontact printing on gold. *J. Phys. Chem. B*, 102:3324–3334, 1998.

[103]A. Bernard, J.P. Renault, B. Michel, H.R. Bosshard, and E. Delamarche. Microcontact printing of proteins. *Adv. Mater.*, 12:1067–1070, 2000.

[104]A.A. Oliva, C.D. James, C.E. Kingman, H.G. Craighead, and G.A. Banker. Patterning axonal guidance molecules using a novel strategy for microcontact printing. *Neurochem. Res.*, 28:1639–1648, 2003.

[105]G. Csucs, T. Künzler, K. Feldman, F. Robin, and N.D. Spencer. Microcontact printing of macromolecules with submicrometer resolution by means of polyolefin stamps. *Langmuir*, 19:6104–6109, 2003.

[106]W. Knoll. *Handbook of biofunctional surfaces*. Pan Stanford Puplishing, 1 edition, 2013.

[107]J.W. Lichtman and J.-A. Conchello. Fluorescence microscopy. *Nature Methods*, 2:910–919, 2005.

[108]I.D. Odell and D. Cook. Immunofluorescence techniques. *J. Ivest. Dermatol.*, 133:e4, 2013.

[109]M.B. Cannell, J.R. Berlin, and W.J. Lederer. Intracellular calcium in cardiac myocytes: calcium transients measured using fluorescence imaging. *Soc. Gen. Physiol. Ser.*, 42:201–214, 1987.

[110]Molecular Probes. Fluo calcium indicators. Technical report, Invitrogen detection technologies, 2011.

[111]D. Thomas, S.C. Tovey, T.J. Collins, M.D. Bootman, M.J. Berridge, and P. Lipp. A comparison of fluorescent Ca2+indicator properties and their use in measuring elementary and global Ca2+signals. *Cell Calcium*, 28:213–223, 2000.

[112]K.R. Gee, K.A. Brown, W.N. Chen, J. Bishop-Stewart, D. Gray, and I. Johnson. Chemical and physiological characterization of fluo-4 Ca(2+)-indicator dyes. *Cell calcium*, 27:97–106, 2000.

[113]J.C. Chang, G.J. Brewer, and B.C. Wheeler. Modulation of neural network activity by patterning. *Biosens. Bioelectron.*, 16:527–533, 2001.

[114]A. Savitzky and M.J.E. Golay. Smoothing and differentiation of data by simplyfied least sqares procedures. *Analyt. Chem.*, 36:1627–1639, 1964.

[115]C.W.J. Granger. Investigating causal relations by econometric models and cross-spectral methods. *Econometrica*, 37:424–438, 1969.

[116]A. Roebroeck, E. Formisano, and R. Goebel. Mapping directed influence over the brain using Granger causality and fMRI. *NeuroImage*, 25:230–242, 2005.

[117]A.K. Seth. A MATLAB toolbox for Granger causal connectivity analysis. *J. Neurosci. Meth.*, 186:262–273, 2010.

[118]L. Barnett and A.K. Seth. The MVGC multivariate Granger causality toolbox: A new approach to Granger-causal inference. *J. Neurosci. Meth.*, 223:50–68, 2014.

[119]K.J. Blinowska, R. Kus, and M. Kaminski. Granger causality and information flow in multivariate processes. *Physi. Rev. E Stat. Nonlin. Soft Matter Phys.*, 70:050902, 2004.

[120]H. Yamamoto, A. Hirano-Iwata, T. Tanii, S. Kobota, and M Niwano. Spontaneous activity patterns of small neuronal ensembles. In *The 4th RIEC International Symposium on Brain Functions and Brain Computer*, 2016.

[121]H. Yamamoto, S. Kuboty, A. Hirano-Iwata, Y. Chida, M. Morita, T. Tanii, and M Niwano. Scale-dependent regulation of synchronized activity in living neuronal networks. *under review*, 2016.

[122]S. Werner and R. Grose. Regulation of wound healing by growth factors and cytokines. *Physiol. Rev.*, 83:835–870, 2003.

[123]H. Ogbomo, M. Michaelis, D. Klassert, H.W. Doerr, and J. Cinatl. Resistance to cytarabine induces the up-regulation of NKG2D ligands and enhances natural killer cell lysis of leukemic cells. *Neoplasia*, 10:1402–1410, 2008.

[124]M. O'Toole, P. Lamoureux, and K.E. Miller. A physical model of axonal elongation: force, viscosity, and adhesions govern the mode of outgrowth. *Biophysi. J.*, 94:2610–2620, 2008.

[125]D.M. Suter and K.E. Miller. The emerging role of forces in axonal elongation. *Prog. Neurobiol.*, 94:91–101, 2011.

[126]K. Franze. The mechanical control of nervous system development. *Development*, 140:3069–3077, 2013.

[127]M. O'Toole, P. Lamoureux, and K.E. Miller. Measurement of subcellular force generation in neurons. *Biophys. J.*, 108:1027–1037, 2015.

[128]R.A. Koene, B. Tijms, P. van Hees, F. Postma, A. de Ridder, G.J.A. Ramakers, J. van Pelt, and A. van Ooyen. NETMORPH: a framework for the stochastic generation of large scale neuronal networks with realistic neuron morphologies. *Neuroinformatics*, 7:195–210, 2009.

[129]M. Mulas and P. Massobrio. NeuVision: A novel simulation environment to model spontaneous and stimulus-evoked activity of large-scale neuronal networks. *Neurocomputing*, 122:441–457, 2013.

[130]D. Lenthe. Modelierung der morphogenese von neuronalen populationen in 2D - modeling morphogenesis of 2D neuronal populations. Master's thesis, RWTH Aachen University, 2015.

[131]P Baas. Force generation by cytoskeletal motor proteins as a regulator of axonal elongation and retraction. *Trends Cell Biol.*, 11:244–249, 2001.

[132]G. Deshpande, S. LaConte, G.A. James, S. Peltier, and X. Hu. Multivariate Granger causality analysis of fMRI data. *Hum. Brain Mapp.*, 30:1361–1373, 2009.

[133]Z. Zhou, Y. Chen, M. Ding, P. Wright, Z. Lu, and Y. Liu. Analyzing brain networks with PCA and conditional Granger causality. *Hum. Brain Mapp.*, 30:2197–2206, 2009.

[134]L. Pan, S. Alagapan, E. Franca, S.S. Leondopulos, T.B. DeMarse, G.J. Brewer, and B.C. Wheeler. An in vitro method to manipulate the direction and functional strength between neural populations. *Front. Neural Circuit.*, 9:32, 2015.

[135]M. Garwicz and G. Andersson. Spread of synaptic activity along parallel fibres in cat cerebellar anterior lobe. *Exp. Brain Res.*, 88:615–622, 1992.

[136]I. Vranesic, T. Iijima, M. Ichikawa, G. Matsumoto, T. Knopfel, and T Knöpfel. Signal transmission in the parallel fiber-Purkinje cell system visualized by high-resolution imaging. *Proc. Natl. Acad. Sci. USA*, 91:13014–13017, 1994.

[137]S.S. Dellal, R. Luo, and T.S. Otis. GABAA receptors increase excitability and conduction velocity of cerebellar parallel fiber axons. *J. Neurophysiol.*, 107:2958–2970, 2012.

[138]S.A. Arrhenius. Über die Dissociationswärme und den Einflusß der Temperatur auf den Dissociationsgrad der Elektrolyte. *Z. Phys. Chem.*, 4:96–116, 1889.

[139]B.A. Reyes, J.S. Pendergast, and S. Yamazaki. Mammalian peripheral circadian oscillators are temperature compensated. *J. Biol. Rhythms*, 23:95–98, 2008.

[140]J.-M. Ramirez, A.K. Tryba, and F. Pena. Pacemaker neurons and neuronal networks: an integrative view. *Curr. Opin. Neurobiol.*, 14:665–674, 2004.

[141]C.T.i Genis. Pacemaker neuron model with plastic firing rate: Entrainment and learning ranges. *Biol. Cybern.*, 52:79–91, 1985.

[142]M. Baker. Light tools. *Nat. Methods Methods*, 8:19–22, 2010.

[143]J. Nakai, M. Ohkura, and K. Imoto. A high signal-to-noise Ca(2+) probe composed of a single green fluorescent protein. *Nat. Biotechnol.*, 19:137–141, 2001.

[144]M. Mank and O. Griesbeck. Genetically encoded calcium indicators. *Chemi. Rev.*, 108:1550–1564, 2008.

[145]L. Tian, S.A. Hires, and L.L. Looger. Imaging neuronal activity with genetically encoded calcium indicators. *Cold Spring Harb. Protoc.*, 2012:647–656, 2012.

[146]J.W. Hartley and W.P. Rowe. A new mouse virus apparently related to the adenovirus group. *Virology*, 11:645–647, 1960.

[147]W.E. Meador, A.R. Means, and F.A. Quiocho. Target enzyme recognition by calmodulin: 2.4 A structure of a calmodulin-peptide complex. *Science*, 257:1251–1555, 1992.

[148]J. Akerboom, J.D.V. Rivera, M.M.R. Guilbe, E.C.A. Malavé, H.H. Hernandez, L. Tian, S.A. Hires, J.S. Marvin, L.L. Looger, and E.R. Schreiter. Crystal structures of the GCaMP calcium sensor reveal the mechanism of fluorescence signal change and aid rational design. *J. Biol. Chem.*, 284:6455–6464, 2009.

[149]Q. Wang, B. Shui, M.I. Kotlikoff, and H. Sondermann. Structural basis for calcium sensing by GCaMP2. *Structure*, 16:1817–1827, 2008.

[150]Y.N. Tallini, M. Ohkura, B.-R. Choi, G. Ji, K. Imoto, R. Doran, J. Lee, P. Plan, J. Wilson, H.-B. Xin, A. Sanbe, J. Gulick, J. Mathai, J. Robbins, G. Salama, J. Nakai, and Mi.I. Kotlikoff. Imaging cellular signals in the heart in vivo: Cardiac expression of the high-signal Ca2+ indicator GCaMP2. *Proc. Natil. Acad. Sci. USA*, 103:4753–4758, 2006.

[151]L.F. Krieger. Optogenetic as well as intracellular recordings and stimulations of structured excitable cellular networks . Master's thesis, University of Konstanz, 2014.

[152]C.A. Thomas, P.A. Springer, G.E. Loeb, Y. Berwald-Netter, and L.M. Okun. A miniature microelectrode array to monitor the bioelectric activity of cultured cells. *Exp. Cell Res.*, 74:61–66, 1972.

[153]J. Pine. Recording action potentials from cultured neurons with extracellular microcircuit electrodes. *J. Neurosci. Meth.*, 2:19–31, 1980.

[154]Y. Nam and B.C. Wheeler. In vitro microelectrode array technology and neural recordings. *Crit. Revi. Biomed. Eng.*, 39:45–61, 2011.

[155]C.D. James, R. Davis, M. Meyer, A. Turner, S. Turner, G. Withers, L. Kam, G. Banker, H. Craighead, M. Isaacson, J. Turner, and W. Shain. Aligned microcontact printing of micrometer-scale poly-L-lysine structures for controlled growth of cultured neurons on planar microelectrode arrays. *IEEE Trans. Biomed. Eng.*, 47:17–21, 2000.

[156]L. Wang, L. Liu, X. Li, N. Magome, K. Agladze, and Y. Chen. Multi-electrode monitoring of guided excitation in patterned cardiomyocytes. *Microelectron. Eng.*, 111:267–271, 2013.

[157]A. Hai, J. Shappir, and M.E. Spira. In-cell recordings by extracellular microelectrodes. *Nat. Methods*, 7:200–202, 2010.

[158]F. Santoro, S. Dasgupta, J. Schnitker, T. Auth, E. Neumann, G. Panaitov, G. Gompper, and A. Offenhäusser. Interfacing electrogenic cells with 3D. *ACS Nano*, 8:6713–6723, 2014.

[159]A. Czeschik, P. Rinklin, U. Derra, S. Ullmann, P. Holik, S. Steltenkamp, A. Offenhäusser, and B. Wolfrum. Nanostructured cavity devices for extracellular stimulation of HL-1 cells. *Nanoscale*, 7:9275–9281, 2015.

[160]N.C. Shaner, G.H. Patterson, and M.W. Davidson. Advances in fluorescent protein technology. *J. Cell Sci.*, 120:4247–4260, 2007.

[161]H. Luo, J. Yang, H. Jin, C. Huang, J. Fu, F. Yang, H. Gong, S. Zeng, Q. Luo, and Z. Zhang. Tetrameric far-red fluorescent protein as a scaffold to assemble an octavalent peptide nanoprobe for enhanced tumor targeting and intracellular uptake in vivo. *FASEB*, 25:1865–1873, 2011.

[162]G. Nagel, D. Ollig, M. Fuhrmann, S. Kateriya, A.M. Musti, E. Bamberg, and P. Hegemann. Channelrhodopsin-1: a light-gated proton channel in green algae. *Science*, 296:2395–2398, 2002.

[163]J.Y. Lin. A user's guide to channelrhodopsin variants: features, limitations and future developments. *Exp. Physiol.*, 96:19–25, 2011.

[164]M. Volgraf, P. Gorostiza, R. Numano, R.H. Kramer, E.Y. Isacoff, and D. Trauner. Allosteric control of an ionotropic glutamate receptor with an optical switch. *Nat. Chem. Biol.*, 2:47–52, 2006.

[165]W. Gajewski, P. Achatz, O.A. Williams, K. Haenen, E. Bustarret, M. Stutzmann, and J.A. Garrido. Electronic and optical properties of boron-doped nanocrystalline diamond films. *Phy. Rev. B*, 79:045206, 2009.

[166]W. Li, Z. Xu, J. Huang, X. Lin, R. Luo, C.-H. Chen, and P. Shi. NeuroArray: a universal interface for patterning and interrogating neural circuitry with single cell resolution. *Sci. Rep.*, 4:4784, 2014.

[167]P. Rinklin, D. Afanasenkau, S. Wiegand, A. Offenhäusser, and B. Wolfrum. Inducing microscopic thermal lesions for the dissection of functional cell networks on a chip. *Lab Chip*, 15:237–243, 2015.

[168]C.P. Ferri, M. Prince, C. Brayne, H. Brodaty, L. Fratiglioni, M. Ganguli, K. Hall, K. Hasegawa, H. Hendrie, Y. Huang, A. Jorm, C. Mathers, P.R. Menezes, E. Rimmer, and M. Scazufca. Global prevalence of dementia: a Delphi consensus study. *Lancet*, 366:2112–2117, 2005.

[169]F.E. Matthews, I. McKeith, J. Bond, and C. Brayne. Reaching the population with dementia drugs: what are the challenges? *Int. J. Geriatr. Psychiatry*, 22:627–631, 2007.

[170]M.J. Volles, S.J. Lee, J.C. Rochet, M.D. Shtilerman, T.T. Ding, J.C. Kessler, and P.T. Lansbury. Vesicle permeabilization by protofibrillar alpha-synuclein: implications for the pathogenesis and treatment of Parkinson's disease. *Biochemistry*, 40:7812–7819, 2001.

[171]M.J. Volles and P.T. Lansbury. Vesicle permeabilization by protofibrillar alpha-synuclein is sensitive to Parkinson's disease-linked mutations and occurs by a pore-like mechanism. *Biochemistry*, 41:4595–602, 2002.

[172]C. Ramassamy, D. Averill, U. Beffert, S. Bastianetto, L. Theroux, S. Lussier-Cacan, J.S. Cohn, Y. Christen, J. Davignon, R. Quirion, and J. Poirier. Oxidative damage and protection by antioxidants in the frontal cortex of Alzheimer's disease is related to the apolipoprotein E genotype. *Free Radic. Biol. Med.*, 27:544–553, 1999.

[173]P. Ferrigno and P.A. Silver. Polyglutamine expansions: proteolysis, chaperones, and the dangers of promiscuity. *Neuron*, 26:9–12, 2000.

[174]M.G. Spillantini, M.L. Schmidt, V.M. Lee, J.Q. Trojanowski, R. Jakes, and M. Goedert. Alpha-synuclein in Lewy bodies. *Nature*, 388:839–840, 1997.

[175]M.C. Irizarry, W. Growdon, T. Gomez-Isla, K. Newell, J.M. George, D.F. Clayton, and B.T. Hyman. Nigral and cortical Lewy bodies and dystrophic nigral neurites in Parkinson's disease and cortical Lewy body disease contain alpha-synuclein immunoreactivity. *J. Neuropathol. Exp. Neurol.*, 57:334–337, 1998.

[176]A. Takeda, M. Mallory, M. Sundsmo, W. Honer, L. Hansen, and E. Masliah. Abnormal accumulation of NACP/alpha-synuclein in neurodegenerative disorders. *Am. J. Pathol.*, 152:367–372, 1998.

[177]D.J. Selkoe, T. Yamazaki, M. Citron, M.B. Podlisny, E.H. Koo, D.B. Teplow, and C. Haass. The role of APP processing and trafficking pathways in the formation of amyloid beta-protein. *Ann. NY Acad. Sci.*, 777:57–64, 1996.

[178]J.Q. Trojanowski and V.M. Lee. ”Fatal attractions” of proteins. A comprehensive hypothetical mechanism underlying Alzheimer's disease and other neurodegenerative disorders. *Ann. NY Acad. Sci.*, 924:62–67, 2000.

[179]D.M. Walsh, B.P. Tseng, R.E. Rydel, M.B. Podlisny, and D.J. Selkoe. The oligomerization of amyloid beta-protein begins intracellularly in cells derived from human brain. *Biochemistry*, 39:10831–10839, 2000.

Acknowledgment

Prof. Andreas Offenhäusser - Thank you for the opportunity to work in your exciting institute. I enjoyed the open minded lab culture and challenging work atmosphere. You have a great hand to create a interdisciplinary working environment, where physicists naturally work in the biolab without loosing the physics behind the scene.
Prof. Bernhard Wolfrum - Thank you for being a motivative group leader. You always brought a new perspective to my project and made me review my decisions.
Tina & Rita - Danke für eure organisatorische Arbeit in und um die Labore, durch eure Ordnung, Hartnäckigkeit und beharrliches kämpfen gegen Windmühlen ist die produktive Arbeit erst möglich. Außerdem danke ich euch für eure Hilfe im Labor und eure Ratschläge zu meinen Experimenten, ohne sie wäre ich in die eine oder andere Sackgasse gelaufen.
Tina - Danke für dein offenes Ohr und die aufbauenden Worte, wenn sich meine Motivation an einem Tiefpunkten befand.
Kay & Volker - Thank you for your advices on my work and inspiring discussions. You helped me to get another perspective and helped with all the little things. I also enjoyed talking about non-work related thinks to clear my mind for a reset during the day.
Irina - Thank you for taking over my ideas. It is good to know that some is proceeding my work or is at least inspired by the results and their implications.
My family - Danke für eure ständige Unterstützung und euren Rückhalt. Ohne euch wäre ich nicht so weit gekommen, wie ich es jetzt bin.
Christiane - Danke für dein Verständnis und deine Geduld mit mir. Vor allem in der letzten Phase meiner Arbeit hast du mir den Rücken frei gehalten und keine Gegenleistung erwartet.
Vanessa - Thank you for all your advice. I could approach you with any kind of technical or biological question and you always knew the answer. Even though we have an institute Wiki, allot of knowledge would be lost without you. Moreover you were always very patient with me in proofreading my manuscripts.
Ulrike, Lars & Dennis - You were great master students to me and you helped me looking into side projects, that I could not realize within my thesis. In particular you did a great job in the biolab and tackled all the problems I confronted you with. I am very pleased to have

worked with you.
Marko - Danke für die Reinraumarbeit und die Fürsorge für die Glovebox.
Michael - Danke für die Reinraumprozessierung der Master und Stempel.
PGI-8/ICS-8 you made it an inspiring working atmosphere with fruitful discussions. Because of you the every day work was a pleasure and I loved to come to work every day.

Appendix A: Figures

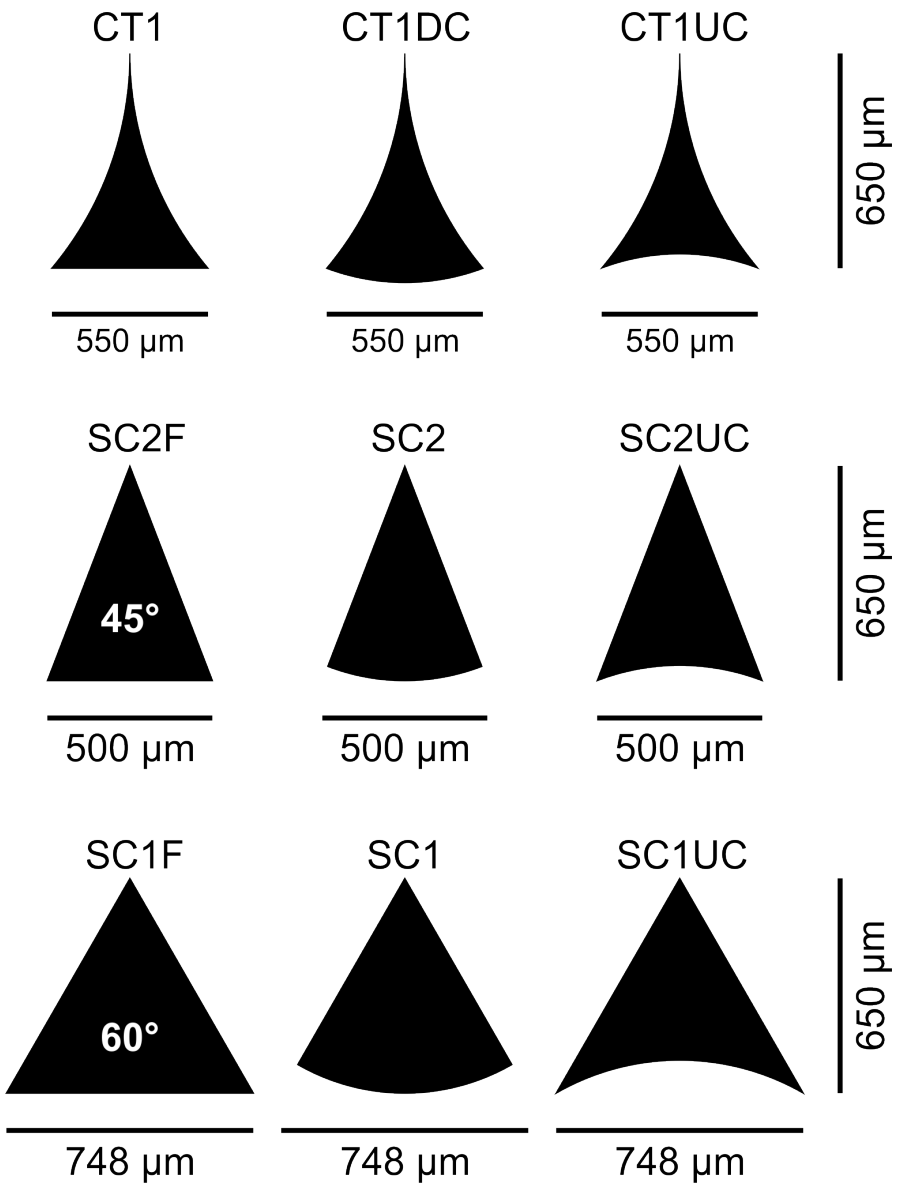

Figure A.1: Sketch of the design of the SC and CT structures with a differently shaped bases. Every structure was designed with a flat or a curved base while the orientation of the curvature is opposite for UC and DC.

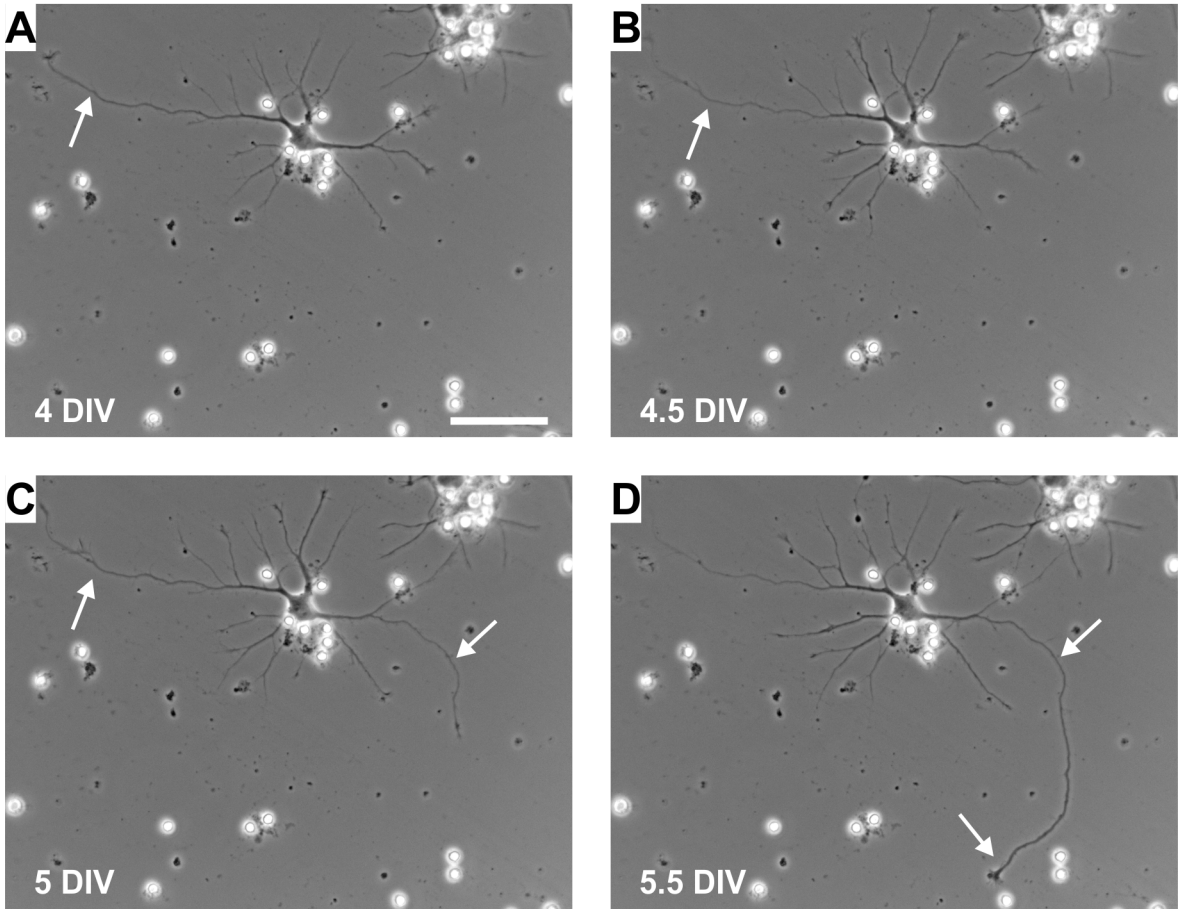

Figure A.2: Change of axonal polarity during development. The axon was determined by length. **A**) The premature axon is indicated by the white arrow. Also dendrites are visible after 4 DIV. **B**) At 4.5 DIV the axon appears thinner than at **A**) but the dendrites continued developing. **C**) After 5 DIV one of the former dendrites (marked with a white arrow) starts sprouting in the opposite direction of the axon. **D**) The newly generated axon stretches even further and exhibits a well developed growth cone. At the same time the former axon retracts and regenerates to the same length as the other dendrites. Scale bar: 50 μm

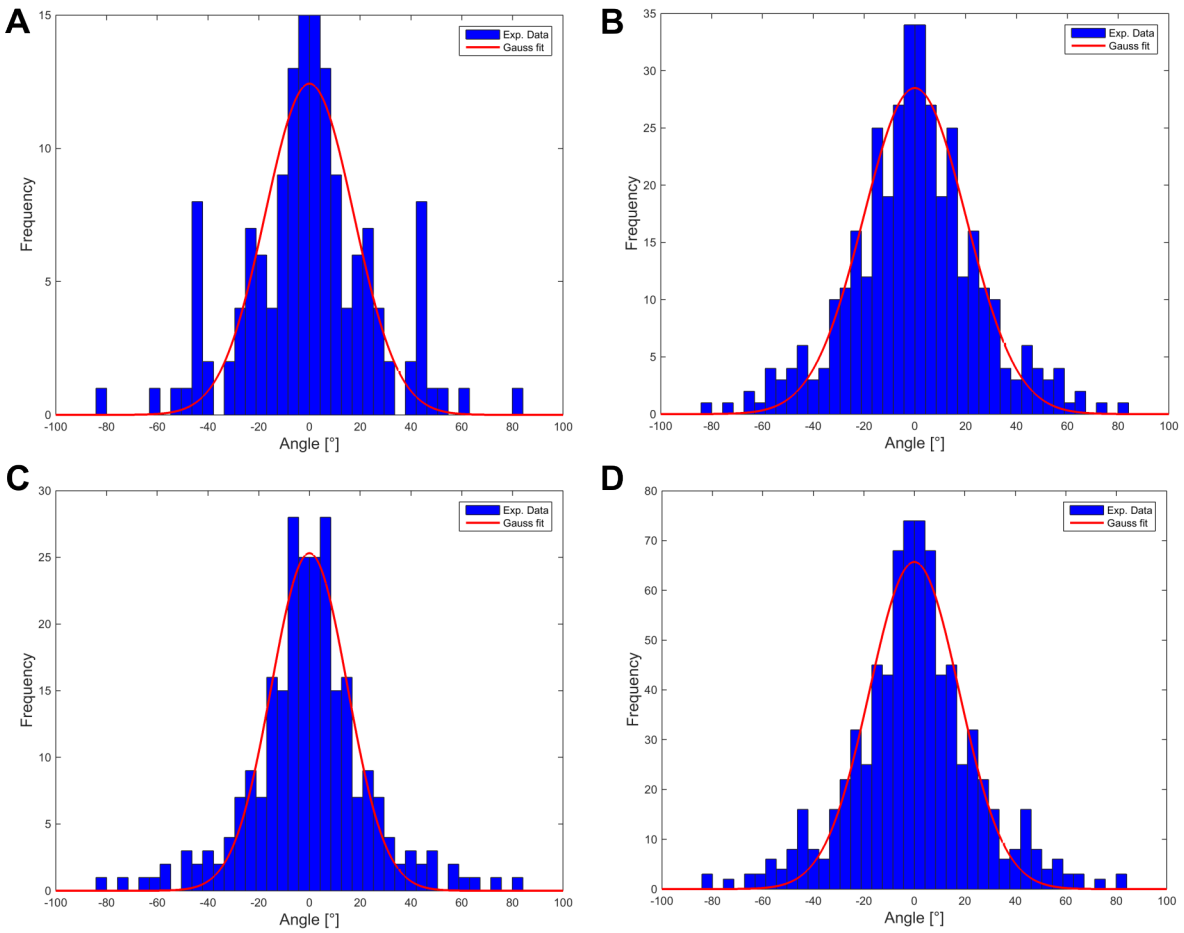

Figure A.3: Histogram plots of turn angle distributions on CT1 patterned substrates with fitted normal distribution at different points in time. **A**) 1.0 DIV: $\sigma = 17°$, $\chi^2 = 0.75$; **B**) 1.5 DIV: $\sigma = 20°$, $\chi^2 = 0.91$; **C**) 2.0 DIV: $\sigma = 15°$, $\chi^2 = 0.93$; **D**) Summation of all evaluated data: $\sigma = 17°$, $\chi^2 = 0.92$. The angle distribution narrows over time and larger angles are more unlikely to appear at later stages of development.

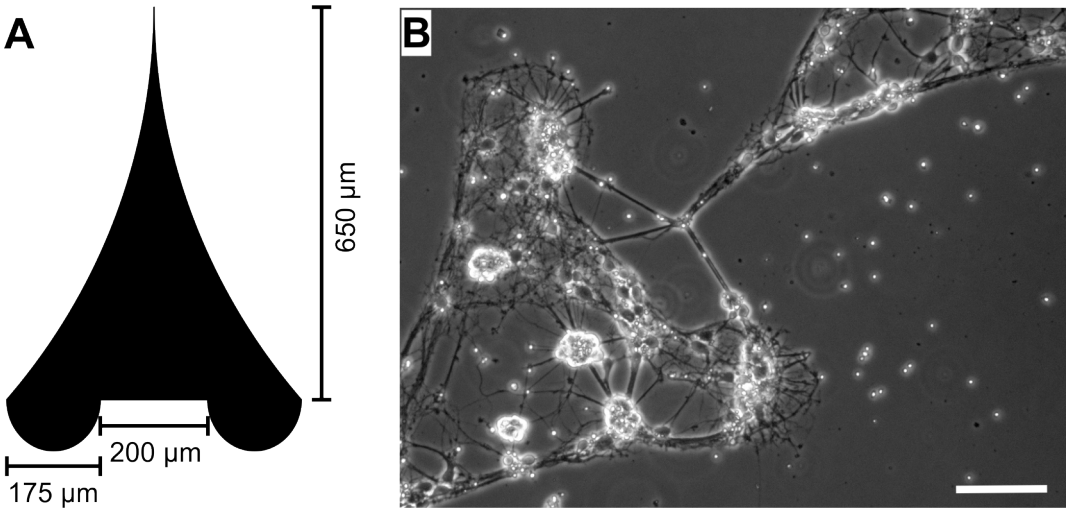

Figure A.4: Base variation of a CT1 structure. **A**) Design of a CT1 structure with semicircles (CT1WC). To the base of the CT1 structure semicircles with a diameter of 175 μm were added at both sides. The other dimensions were kept. **B**) Ramified networks are formed within the structure. In contrast to regular CT1 structures the neurites are not funneled by the tip towards the next structure but vault from and to the added semicircles. Scale bar: 100 μm

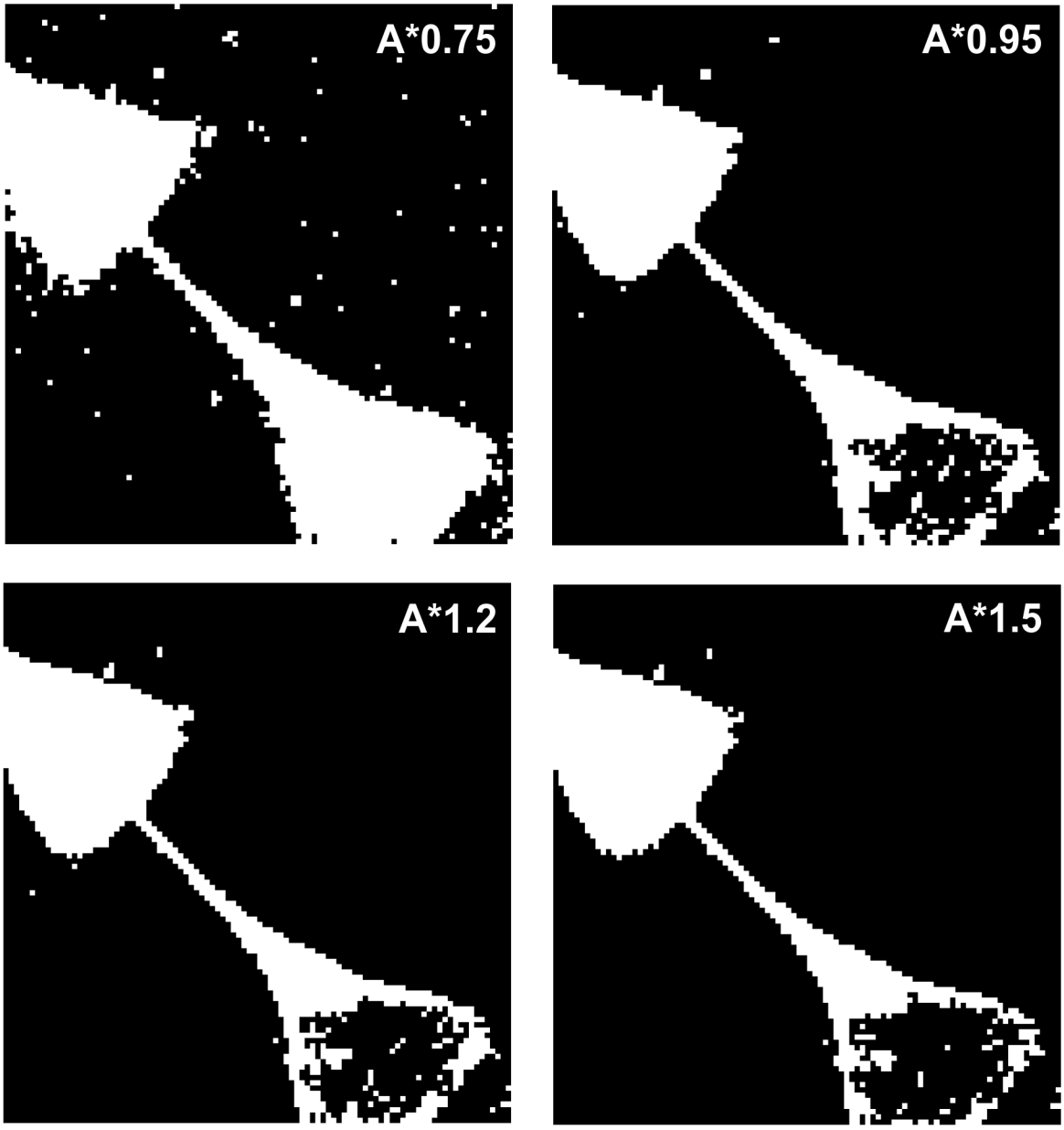

Figure A.5: Thresholding fluorescence intensity for recognition of active pixels. Active pixels are colored white. A value of $A * 0.75$ increases the number of pixels considered as active in contrast to $A * 0.95$ as the threshold value. In contrast an increase up to $A * 1.5$ does not affect the number of active pixels as much as the previously described decrease of the value.

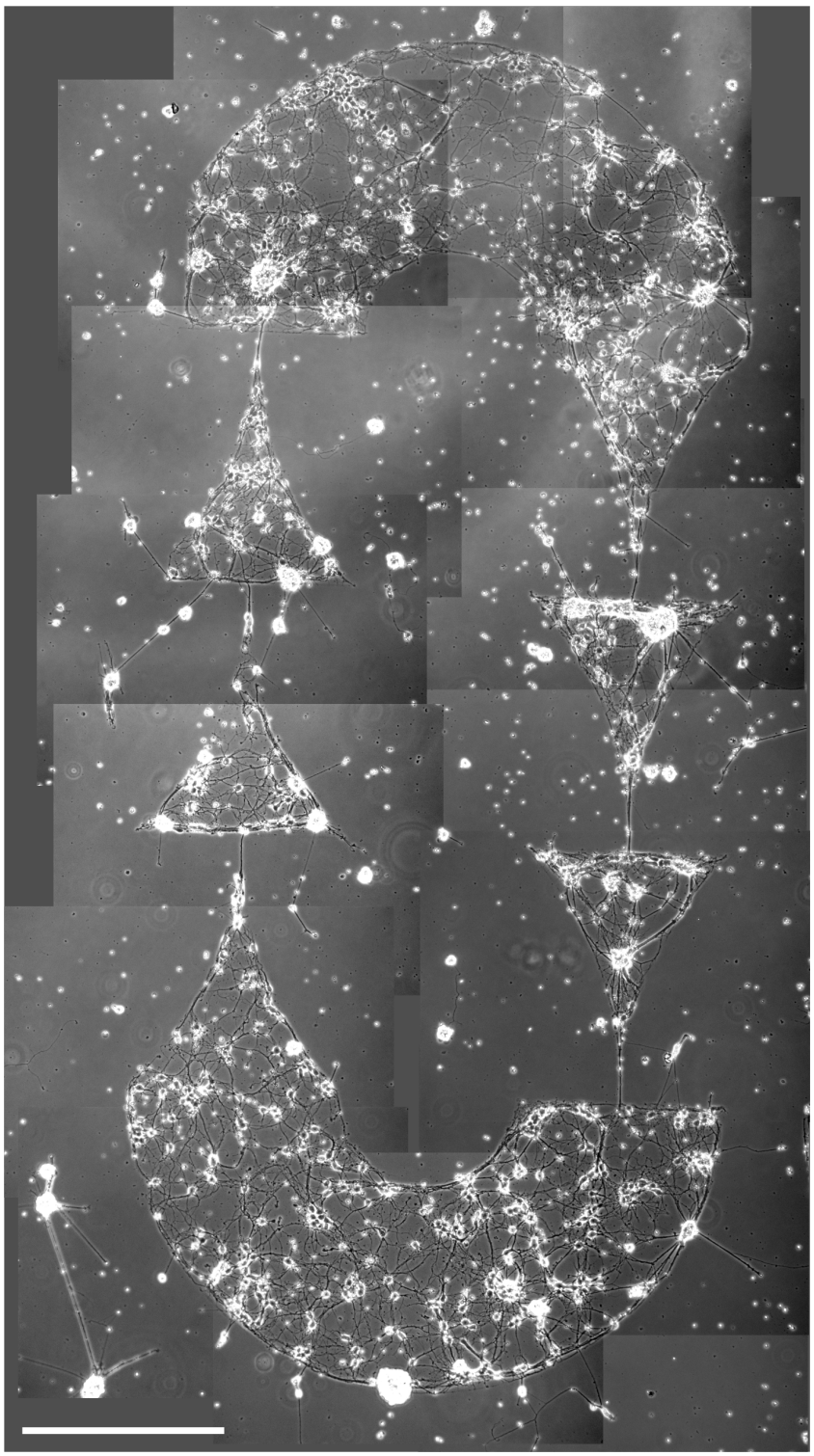

Figure A.6: Neuronal growth on on a 3CT1 neuroCAP structure. The entire area of the pattern is covered with a ramified network. Some clusters of cells formed within the populations but mostly single cell can be found allover the network. The gateways between adjacent pattern are well defined and only one junction exhibits cross growing neurites. Scale bar: 500 μm

Appendix B: Abbreviations

AAV . . . . . adeno associated virus

AD . . . . . Alzheimer's disease

AM . . . . . acetoxymethyl ester

Ara-C . . . . . arabinofuranosyl cytidine

ATP . . . . . adenosintriphosphate

BB . . . . . blocking buffer

CaM . . . . . calmodulin

CCD . . . . . charge-coupled device

CNS . . . . . central nervous system

CSE . . . . . chamber spanning excitation

CT . . . . . curved sided triangle

DAPI . . . . . 4',6-Diamidin-2-phenylindol)

DIV . . . . . days *in vitro*

DNA . . . . . deoxyribonucleic acid

DPT . . . . . days *post transduction*

ECM . . . . . extracellular matrix

EGTA . . . . . ethylene glycol tetraacidic acid

E-patch . . . . . extracellular patch solution

ER . . . . . endoplasmatic reticulum

FBS . . . . . fetal bovine serum

FITC . . . . . FITC

fMRI . . . . . functional magnetic resonance imaging

FOTCS . . . . . (Tridecafluoro-1,1,2,2-tetrahydrooctyl)trichlorosilane

G-causality . . . . . Granger-causality

GBSS . . . . . Gey's Balanced Salt Solution

GECI . . . . . genetically encoded calcium indicator

GFP . . . . . green fluorescent protein

ICS-8 . . . . . Institute of Complex Systems 8

LED . . . . . Light Emitting Diode

MAP2 . . . . . mcirotuble-associated protein 2

μCP . . . . . microcontact Printing

MEA . . . . . microelectrode array

neuroCAP . . . . . neuronal circulating action potential

NFH . . . . . Anti-200 kD Neurofilament Heavy

PBS . . . . . phosphate buffered saline

PDMS . . . . . poly(dimethylsiloxane

PGI-8 . . . . . Peter-Grünberg-Institute 8

PLL . . . . . poly-L-lysine

POP . . . . . polyolefin plastomer

ROI . . . . . region of interest

RT . . . . . room temperature

SC . . . . . sector of a circle

sCMOS . . . . . scientific complementary metal-oxide-semiconductor

SE . . . . . single event

SG . . . . . Savitzky-Golay

SSE . . . . . substrate spanning excitation

SPM . . . . . surface plasmon microscopy

Appendix C: Solutions and Materials

Blocking Buffer

Substance	Amount
PBS	50 ml
Bovine serum albumin	0.5 g
Goat serum	1 ml

Extracellular Patch solution

Substance	Endconcentration [mM]	Initial weight [g]
NaCl	120	7.013
KCl	3	0.224
$MgCl_2$	1	0.203
Hepes	10	2.383
$CaCl_2$	2	0.222

Above listed substances are diluted in 1 liter double distilled water and subsequently the pH value is adjusted with 1N NaOH to a pH value of 7.3. The resulting osmolarity is 248 mosm/kg.

Neuro Basal media

Substance	Amount
Neurobasal media	50 ml
B-27 Supplement (final concentration 1% v/v)	500 μl
L-Glutamine (final concentration 0.25% v/v)	125 μl
gentamycin (final concentration 1% v/v)	50 μl

Phosphate Buffer Saline solution (PBS)

Substance	Endconcentration [mM]	Initial weight [g]
NaCL	137	80.063
KCl	2.7	2.013
Na_2HPO_4	8	11.499
KH_2PO_4	1.8	2.00

Above listed substances are diluted in 1 liter double distilled water and subsequently the pH value is adjusted with 1N NaOH to a pH value of 7.4.

List of used materials

Material	Specification	Supplier
Alexa Fluor Dyes	2 mg/ml	Life Technologies
Bovine serum albumin	Inactivate at 56°C for 30 min	Sigma Aldrich
B-27 Supplement		Life Technologies
DAPI	2.5 mg/ml	Life Technologies
Dimethylsulfoxid		Sigma
Ethanol		Sigma Aldrich
Fetal bovine serum	EU Approved Origin	Life Technologies
Fluo4-AM	diluted to 1 μg/μl in DMSO	Invitrogen
Gentamycin	10 mg/ml	Life Technologies
Goat serum	EU Approved Origin	Life Technologies
KCl		Sigma Aldrich
KH_2PO_4		Sigma Aldrich
Laminin		Sigma Aldrich
L-Glutamine	200 mM	Life Technologies
NaCl		Sigma Aldrich
Na_2HPO_4		Sigma Aldrich
Neurobasal media		Life Technologies
NFH	2 μg/ml	abcam
MAP2	2 μg/ml	Millipore
Poly-L-lysine	1 mg/ml	Sigma Aldrich

Authors list of publications

Journal publications

Albers, Jonas, Toma, Koji, Offenhäusser, Andreas. 2015. Engineering connectivity by multiscale micropatterning of individual populations of neurons. *Biotechnology Journal*. 10 (2): 332-338.

Albers, Jonas, Offenhäusser, Andreas. 2016. Signal propagation between neuronal populations controlled by micropatterning. *Frontiers in Bioengineering and Biotechnology*. *Frontiers in Bioengineering and Biotechnology*, 4, 46.

Ghosh Moulick, Ranjita, Afanasenkau, Dzmitry, Choi, Sung-Eun, **Albers, Jonas**, Lange, Wienke, Mabeck, Vanessa, Utesch, Tillmann, Offenhäusser, Andreas. 2016. Reconstruction of fusion proteins in supported lipid bilayers for the study of cell surface receptor-ligand interactions in cell-cell contact. *Langmuir*. 32 (14): 3462-3469.

Invited talks

Albers, Jonas, Zobel, Kathrin, Offenhäusser, Andreas. 2016. Function follows form: Controlling signal propagation by patterning populations of neurons. *The 4th RIEC International Symposium on Brain Functions and Brain Computer*.